

**COMPARISON OF
GEOSTATISTICS AND ARTIFICIAL NEURAL NETWORKS
IN RESERVOIR PROPERTY ESTIMATION**

**A THESIS SUBMITTED TO
THE GRADUATE SCHOOL OF NATURAL AND APPLIED SCIENCES
OF
THE MIDDLE EAST TECHNICAL UNIVERSITY**

BY

SADUN ARZUMAN

**IN PARTIAL FULFILLMENT OF THE REQUIREMENTS FOR THE DEGREE
OF
DOCTOR OF PHILOSOPHY
IN
GEOLOGICAL ENGINEERING**

SEPTEMBER 2009

Approval of the thesis:

**COMPARISON OF
GEOSTATISTICS AND ARTIFICIAL NEURAL NETWORKS
IN RESERVOIR PROPERTY ESTIMATION**

submitted by **SADUN ARZUMAN** in partial fulfilment of the requirements for the degree of **Doctor of Philosophy in Geological Engineering Department, Middle East Technical University** by,

Prof. Dr. Canan Özgen

Dean, Graduate School of **Natural and Applied Sciences**

Prof. Dr. M. Zeki Çamur

Head of Department, **Geological Engineering**

Prof. Dr. Nurkan Karahanoğlu

Supervisor, **Geological Engineering Dept., METU**

Examining Committee Members:

Prof. Dr. G. M. Vedat Toprak

Geological Engineering Department, METU

Prof. Dr. Nurkan Karahanoğlu

Geological Engineering Department, METU

Prof. Dr. Serhat Akın

Petroleum & Natural Gas Engineering Department, METU

Prof. Dr. Ahmet T. Başokur

Geophysical Engineering Department, Ankara University

Assoc. Prof. Dr. M. Lütfi Süzen

Geological Engineering Department, METU

Date:

11.09.2009

I hereby declare that all information in this document has been obtained and presented in accordance with academic rules and ethical conduct. I also declare that, as required by these rules and conduct, I have fully cited and referenced all material and results that are not original to this work.

Name, Last name : Sadun Arzuman

Signature :

ABSTRACT

COMPARISON OF GEOSTATISTICS AND ARTIFICIAL NEURAL NETWORKS IN RESERVOIR PROPERTY ESTIMATION

Arzuman, Sadun

Ph.D., Geological Engineering Department

Supervisor: Prof. Dr. Nurkan Karahanoğlu

September 2009, 145 Pages

In this dissertation, 3D surface seismic data was integrated with the well logs to be able to define the properties in every location for the reservoir under investigation. To accomplish this task, geostatistical and artificial neural networks (ANN) techniques were employed.

First, missing log sets in the study area were estimated using common empirical relationships and ANN. Empirical estimations showed linear dependent results that cannot be generalized. On the other hand, ANNs predicted missing logs with an very high accuracy. Sonic logs were predicted using resistivity logs with 90% correlation coefficient. Second, acoustic impedance property was predicted in the study area. AI estimation first performed using sonic log with GRNN and 88% CC was obtained. AI estimation was repeated using sonic and resistivity logs and the result were improved to 94% CC.

In the final part of the study, SGS technique was used with collocated cokriging techniques to estimate NPHI property. Results were varying due to nature of the algorithm. Then, GRNN and RNN algorithms were applied to predict NPHI property. Using optimized GRNN network parameters, NPHI was estimated with high accuracy.

Results of the study were showed that ANN provides a powerful solution for reservoir parameter prediction in the study area with its flexibility to find out non-linear relationships from the existing available data.

Keywords: geostatistics, artificial neural networks, reservoir property estimation

ÖZ

REZERVUAR PARAMETRE KESTİRİMİNDE JEOİSTATİSTİK VE YAPAY SİNİR AĞLARI'NIN KARŞILAŞTIRILMASI

Arzuman, Sadun

Doktora, Jeoloji Mühendisliği Bölümü

Tez Yöneticisi: Prof. Dr. Nurkan Karahanoğlu

Eylül 2009, 145 Sayfa

Bu çalışmada, incelenen rezervuarın her noktasındaki parametreleri tanımlayabilmek için, 3B sismik veriler kuyu verileri ile entegre edilmiştir. Bu amacı başarabilmek için, jeostatistik ve yapay sinir ağları (YSA) yöntemleri kullanılmıştır.

İlk olarak, mevcut olmayan kuyu logları empirik ilişkiler ve YSA ile önkestirilmiştir. Empirik kestirimler doğrusal bağımlı genelleştirilemeyen sonuçlar göstermiştir. Diğer taraftan, YSA mevcut olmayan logları yüksek doğrulukta bulabilmiştir. Sonik loglar %90 korelasyon katsayısı ile bulunmuştur. İkinci olarak, akustik empedans parametresi çalışma alanında önkestirilmiştir. Sonik log ve GRNN tekniği kullanılarak yapılan önkestirim işleminde %88 korelasyon katsayısı elde edilmiştir. Akustik empedans kestirimi daha sonra sonik ve rezistivite logları kullanılarak tekrar edilmiş ve sonuçlar iyileştirilmiş ve %94 korelasyon sağlanmıştır.

Çalışmanın son kısmında, SGS jeostatistiksel similasyon algoritması collocated cokriging tekniği ile birlikte kullanılarak sonik porozite parametresi önkestirilmiştir. Algoritmanın çalışma prensibinden dolayı sonuçlar çeşitli olmuştur. Daha sonra, GRNN algoritması sonik porozite parametresini önkestirmek için kullanılmış ve GRNN ile yüksek bir korelasyon sonucu elde edilmiştir.

Bu çalışmanın sonuçları, çalışma alanında YSA'nın rezervuar parametrelerini önkestirebilmek için çok güçlü bir yöntem olduğunu, mevcut verilerden lineer olmayan ilişkiler kurarak göstermiştir.

Anahtar Kelimeler: jeostatistik, yapay sinir ağları, rezervuar parametre önkestirimi

In memory of my mother and father

ACKNOWLEDGEMENTS

First of all, I would like to express my gratitude to my advisor Dr. Nurkan Karahanoğlu for his precious guidance for my academic and personal life and continuous encouragement for completing this dissertation.

I would also like to thank to my committee members Dr. G. M. Vedat Toprak and Dr. Serhat Akin for their support and supervision. Dr. Ahmet T. Başokur and Dr. Lütfi Süzen were also very kind to accept to be in the reviewing committee.

Second, I would like to express my gratitude to my sister and brother for their patience and support.

I also would like to thank to Schlumberger Information Solutions and Intelligent Solutions, Inc. for providing their software packages.

Finally, thanks to Arch Petroleum (and their production company Threshold Production), Enserch, and OXY USA, Inc., for making the data set used in this study available through Bureau of Economic Geology, University of Texas at Austin.

TABLE OF CONTENTS

ABSTRACT	iv
ÖZ	v
DEDICATION	vi
ACNOWLEDGEMENTS	vii
TABLE OF CONTENTS	viii
LIST OF TABLES	x
LIST OF FIGURES	xi
NOMENCLATURE	xvi
CHAPTER	
1. INTRODUCTION	1
1.1 Statement of the Problem	2
1.2 Data Base	3
1.3 Previous Studies	8
2. THEORETRICAL BACKGROUND	12
2.1 Geostatistical Methods	15
2.2 Artificial Neural Networks	31
3. DATA PREPERATION AND METHODOLOGY	38
3.1 Methodology	38
3.2 Seismic and Well Data Quality Checking and Editing	39
3.3 Seismic to Well Tie	45
3.4 Seismic Interpretation	49
3.5 Velocity Model and Depth Conversion	53
3.6 Static Model Building	59
4. ESTIMATION OF MISSING LOG SETS	61
4.1 Empirical Methods	61
4.2 Neural Network Approach	65
4.3 Seismic Inversion	80
4.4 Acoustic Impedance Estimation	83
5. ESTIMATION OF RESERVOIR PARAMETERS BASED ON SEISMIC.	89
5.1 Seismic Attributes	89
5.2 Geostatistical Approach	93
5.3 Neural Network Approach	110

6. DISCUSSION	125
7. CONCLUSIONS	127
REFERENCES	129
APPENDICES	135
A. Well Log Types and Stratigraphic Nomenclature	134
B. Basic Seismic Attributes	138
C. Acoustic Impedance Estimation Results.....	141
D. Variogram Principles.....	142
VITA	145

LIST OF TABLES

TABLES

Table 2.1 Comparison of geostatistical and intelligent systems	14
Table 4.1 Gardner’s velocity-density relationship constants for different lithologies.....	64
Table 4.2 Petrel ANN run DT estimation error results for the well B Yates 18D	72
Table 4.3 PCA results for NPHI estimation using RILD, GR, estimated DT for wells Ashe 6, B Yates 13, B Yates 15, and LOF 2	78
Table 5.1 Seismic attributes correlation table calculated in this study	91
Table 5.2 The most correlated seismic attributes and their correlation coefficients.....	92
Table 5.3 Summary statistics for the SGS simulation results.....	101
Table 5.4 Summary statistics for the SGS collocated cokriging results	107
Table 5.5 Classical and fuzzy logic comparison.....	114
Table A.1 Wells and well log data types available in this study.....	135

LIST OF FIGURES

FIGURES

Figure 1.1 Resolution problem for the reservoir characterization studies	1
Figure 1.2 Fort Worth and other basins around the study area Boonsville over the Middle Pennsylvanian paleogeographic map	3
Figure 1.3 Seismic base map and well locations over the study area.....	4
Figure 1.4 Log types histogram in the study area	5
Figure 1.5 Bend arch - Fort Worth Basin with major structural features and location of oil and gas fields.....	6
Figure 1.6 Generalized Pennsylvanian stratigraphic column for the Fort Worth Basin	7
Figure 2.1 The basic components of an artificial neural network	13
Figure 2.2 Sequential simulation of an unknown porosity value in a layer.....	17
Figure 2.3 The random function model.....	19
Figure 2.4 Omni-directional variogram and correlogram	22
Figure 2.5 Geometric and zonal anisotropy.....	23
Figure 2.6 Cross validation example	25
Figure 2.7 Isotropy and heterotopy.....	26
Figure 2.8 Three different neighborhood cases.....	27
Figure 2.9 Kriging, cokriging and collocated cokriging examples.....	28
Figure 2.10 Basic elements of artificial neural network	31
Figure 2.11 Sum-squared error model	32
Figure 2.12 Error function and its relation to w	33
Figure 2.13 Simple artificial neural network elements.....	33
Figure 2.14 Effect of learning rate on the ANN process	33
Figure 2.15 Multi-layer network with a hidden node and activation function	34
Figure 2.16 Multi-layer network pattern	35
Figure 2.17 Overtraining phenomenon.....	35
Figure 2.18 Schematic learning curves for the training and validation sets	36
Figure 3.1 Methodology developed for this study.....	39
Figure 3.2 Time-migrated 3D seismic data used in this study.....	40
Figure 3.3 Cropped seismic cube and amplitude filter	40
Figure 3.4 Original seismic in-line 152 and result of frequency band filter.....	41

Figure 3.5 Amplitude enhancements for the in-line 152.....	42
Figure 3.6 Basemap showing available wells inside the study area.....	42
Figure 3.7 B Yates 18D type log	43
Figure 3.8 Well correlation section through North-West to South-East representing the formation tops used in this study	44
Figure 3.9 Log-log cross plot for wells B Yates 11, B Yates 18D, and C Yates 9	45
Figure 3.10 Velocity functions for the well B Yates 18D.....	45
Figure 3.11 Sonic correction application for well B Yates 18D.....	46
Figure 3.12 Well B Yates 18D synthetic seismogram	47
Figure 3.13 Wavelet extraction procedure for the B Yates 18D well	48
Figure 3.14 Extracted wavelet using the parameters in Figure 3.13	49
Figure 3.15 Two-way time structure map of the Caddo (MFS90) and David (MFS70) horizons respectively	50
Figure 3.16 Two-way time structure map of the Runaway (MFS53) and Vineyard (MFS20) horizons respectively	51
Figure 3.17 Seismic composite line over the study area	52
Figure 3.18 Variance time slice at 1,093 ms from the seismic survey.....	53
Figure 3.19 Corrected sonic curves for the Wells B Yates 18D, B Yates 11, and C Yates 9.....	54
Figure 3.20 Two way time map (ms) of the Caddo horizon overlain by residual values.....	55
Figure 3.21 Time error plots for the horizons Caddo, David, Runaway, and Vineyard	55
Figure 3.22 3D velocity model built for the whole area	57
Figure 3.23 Interval velocity field was posted on seismic in-line 153	57
Figure 3.24 Seismic in-line 153 showing time and depth converted versions	58
Figure 3.25 Initial structural model for the area	59
Figure 3.26 Structural model for the are which was divided into stratigraphic intervals	60
Figure 3.27 Layering results for the zone 7	60
Figure 4.1 Sonic estimation results using Faust’s relationship for wells Ashe C5 and B Yates 11.....	62
Figure 4.2 Sonic estimation results using Faust’s relationship for wells B Yates 18D and C Yates 9	62
Figure 4.3 Sonic versus sonic estimated (DLT-E) cross plots for well Ashe C5 and B Yates 11 respectively	63

Figure 4.4 Sonic versus sonic estimated (DLT-E) cross plots for well B Yates 18D and C Yates 9 respectively	63
Figure 4.5 Density estimation results using Gardner’s relationship for wells B Yates 11, B Yates 18D, and C Yates 9.....	64
Figure 4.6 Density versus density estimated (RHOB-E) cross plots for well B Yates 11, B Yates 18D, and C Yates 9 respectively.....	64
Figure 4.7 A multilayer neural network structure with a single hidden layer.....	66
Figure 4.8 Log data cross plots for the well B Yates 18D.....	67
Figure 4.9 ANN optimum parameters (MNI, EL and CV) selection error plots	69
Figure 4.10 DT estimation results from ANN versus original DT logs	72
Figure 4.11 Estimated versus original DT log cross plots	73
Figure 4.12 DT estimation results from RILD logs.....	73
Figure 4.13 Cross plots of the estimated DT log versus original DT logs	74
Figure 4.14 DT estimation results for well B Yates 18D using RILD from one and three other wells.	74
Figure 4.15 NPHI versus GR, SP, RILD, RHOB, DT and estimated DT cross plots.....	75
Figure 4.16 NPHI estimation results for 5 wells (Ashe C6, B Yates 13, -15, -18D, and IG Yates 9).....	76
Figure 4.17 NPHI versus estimated NPHI cross plots for wells Ashe C6, B Yates 13, -15, -18D, and IG Yates 9	76
Figure 4.18 Cross-plot of the training results for the NPHI estimation from GR, RILD and estimated DT using wells Ashe 6, B Yates 13, B Yates 15, and LOF 2 (CC=0.884845)	77
Figure 4.19 Cross-plot of the training results for the NPHI estimation using PC1 and PC2.....	78
Figure 4.20 Cross-plot of the training results for the NPHI estimation versus original NPHI logs with and without PCs.....	79
Figure 4.21 Estimated NPHI log for the well Ashe C6.....	79
Figure 4.22 Schematic diagrams of the forward and inverse modeling concepts	81
Figure 4.23 Computed AI logs for the wells having DT and RHOB logs	84
Figure 4.24 Sonic versus Acoustic Impedance cross plots for the wells B Yates 11, C Yates 9, and B Yates 18D	84
Figure 4.25 DT prediction results for the wells B Yates 11, B Yates 18D, and C Yates 9	85
Figure 4.26 Original DT versus estimated DT results from RILD and AI logs	86

Figure 4.27 DT estimation results from RILD and AI logs for the wells B Yates 11, B Yates 18D, and C Yates 9	87
Figure 4.28 DT versus estimated DT cross plots using RILD and AI logs.....	87
Figure 4.29 Distribution of the computed AI logs in the study area	88
Figure 5.1 Classification of post-stack seismic amplitudes	90
Figure 5.2 Upscaled NPHI logs for the Well B Yates 18D.....	94
Figure 5.3 Histogram of the original, upscaled, and to be modeled NPHI logs	94
Figure 5.4 Variogram map for the upscaled NPHI logs	95
Figure 5.5 Sample variograms calculated for upscaled NPHI logs	96
Figure 5.6 Data transformation process for the NPHI logs.....	97
Figure 5.7 Experimental (grey line) and modeled variograms (blue line) for vertical direction for the NPHI logs	99
Figure 5.8 Experimental (grey line) and modeled variograms (blue line) for horizontal major and minor directions for the NPHI logs	99
Figure 5.9 SGS realizations using upscaled NPHI logs	101
Figure 5.10 Histograms of the simulated, upscaled, and original NPHI logs for four runs respectively	102
Figure 5.11 Comparison of original NPHI logs and SGS simulation results for the wells LO Fancher 1, B Yates 7, and Ashe C 1 respectively	103
Figure 5.12 Histogram of the upscaled and original AI logs.....	104
Figure 5.13 Result of the SGS with cokriging using NPHI as a primary and AI as a secondary data	105
Figure 5.14 Cokriging SGS simulation results.....	106
Figure 5.15 Histogram display of the cokriging results using LVM (on the left) and bivariate distribution (on the right)	106
Figure 5.16 SGS collocated cokriging realizations.....	107
Figure 5.17 Comparison of original NPHI logs and collocated cokriging simulation results for the wells LO Fancher 1, B Yates 7, and Ashe C 1 respectively.....	108
Figure 5.18 A typical neuron architecture for MFNN	110
Figure 5.19 Enlarged display of the seismic attributes extracted along the B Yates 18D well	112
Figure 5.20 Linear regression plot and 3D cross plot for the well B Yates 18D	113
Figure 5.21 Degree of influences of each attribute against each other	115
Figure 5.22 Data contribution cross plot (NPHI versus A-3) for quick inspection...	116

Figure 5.23 Sensitivity analysis for the seismic attributes versus property to be estimated (NPHI)	116
Figure 5.24 Well locations in the study area.....	117
Figure 5.25 Error Back Propagation network built to estimate NPHI property from seismic attributes.....	118
Figure 5.26 BPN algorithm training results for the NPHI estimation.....	119
Figure 5.27 BPN algorithm calibration results for the NPHI estimation	119
Figure 5.28 BPN algorithm verification results for the NPHI estimation	120
Figure 5.29 BPN validation results on wells LO Fancher 1, Ashe C1, and B Yates 7	120
Figure 5.30 GRNN algorithm training results for the NPHI estimation	122
Figure 5.31 GRNN algorithm calibration results for the NPHI estimation.....	122
Figure 5.32 GRNN algorithm verification results for the NPHI estimation.....	123
Figure 5.33 GRNN validation results on wells LO Fancher 1, Ashe C1, and B Yates 7	123
Figure A.1 Stratigraphic nomenclature used to define Bend Conglomerate genetic sequences by Bureau of Economic Geology for Boonsville field...	137
Figure C.1 NPHI versus estimated AI cross plots	141
Figure C.2 NPHI versus estimated NPHI cross plots	141
Figure D.1 Sample variogram and variogram model.....	142
Figure D.2 Sample variogram calculation features.....	143

NOMENCLATURE

Abbreviations

1D:	One Dimensional
2D:	Two Dimensional
3D:	Three Dimensional
AGC:	Automatic Gain Control
AI:	Acoustic Impedance
ANN:	Artificial Neural Networks
BSIS:	Bayesian Sequential Indicator Simulation
CA:	Correlation Analysis
CALI:	Caliper
CC:	Correlation Coefficient
CCDF:	Conditional Cumulative Distribution Function
CDF:	Cumulative Distribution Function
CS:	Check Shot
CSSI:	Constrained Sparse Spike
DT:	Delta-t Sonic
FPR:	Fuzzy Pattern Recognition
GR:	Gamma Ray
GRNN:	Generalized Regression Neural Network
GA :	Genetic Algorithm
LL3:	Laterolog 3 Resistivity
LL8:	Laterolog 8 Resistivity
LAT:	Laterolog Resistivity
LCPD:	Local Conditional Probability Distribution
LN:	Long Normal Resistivity
LVM:	Local Varying Mean
MFNN:	Multi-Layer Feedforwarded Neural Network
MICRO:	Micro Log
MLP:	Multi-Layer Perception
MSFL:	Micro Spherically Focused Log
NPHI:	Compensated Neutron
OWT:	One Way Time
PC:	Principal Component
PCA:	Principal Component Analysis
PEF:	Photo Electric Effect
PFS:	Probability Field Simulation
PNN:	Probabilistic Neural Network
RILD:	Deep Induction Resistivity
RILM:	Medium Induction Resistivity
RBF:	Radial Basis Function
RC:	Reflection Coefficient
RHOB:	Bulk Density
SA:	Simulated Annealing
SFL:	Spherically Focused Resistivity
SGR:	Secondary Gas Recovery
SGS:	Sequential Gaussian Simulation
SIS:	Sequential Indicator Simulation
SN:	Short Normal (16") Resistivity

SOM: Kohonen's Self-Organizing Maps
SOR: Secondary Oil Recovery
SP: Spontaneous Potential
T-D: Time-Depth
TWT: Two Way Time
UVQ: Unsupervised Vector Quantizer
VSP: Vertical Seismic Profile

CHAPTER 1

INTRODUCTION

One of the most challenging tasks in today's reservoir characterization studies is the non-existence of abundant hard data, for instance, well logs and cores which usually carry high confidence information. Successful and most accurate characterization works usually integrate all the available data for the reservoir under investigation. Among them, surface seismic (2D & 3D) is not sparse as it is easy to obtain with the high details with current acquisition technologies. On the other hand, well log and core data usually does not exist or scarce in the beginning of the life of the reservoir and expensive to acquire compared to surface seismic. As reservoir characterization studies mostly aim to estimate the reservoir properties in a high level of detail, the well and core data provide the most important input with high resolution information for the limited areal extend around the wells, on the contrary surface seismic data bring low degree of resolution over the whole reservoir with reasonable amount of budget. Therefore, integrating seismic data into reservoir characterization studies is one of the most important targets in practice. In this point of view, integrating surface seismic data with the other types of available data requires the challenge of combined data having different resolution scales (Figure 1.1).

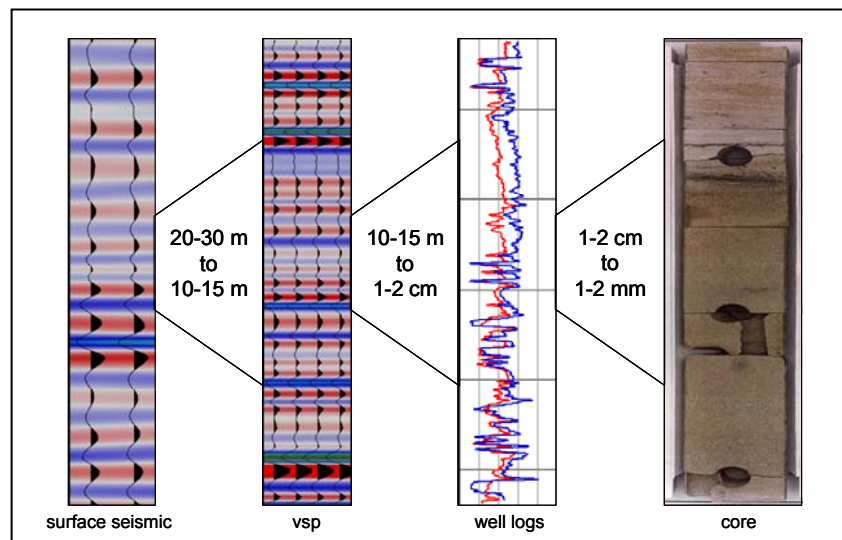


Figure 1.1 Resolution problem for the reservoir characterization studies. The data come usually from various sources with different scales.

1.1 STATEMENT OF THE PROBLEM

Reservoir description is considerably a difficult task because of the limited hard data availability over the existing hydrocarbon fields. Well logs, cores, and similar data can be considered as hard data and conventionally these types of data are used to characterize the reservoirs. The usage of only one type of data usually cannot sufficient for detailed description of the reservoirs. On the other hand, surface seismic data, which is considered as soft data, is abundant over the exploration and production areas and generally cover whole reservoir area and traditionally they are mainly being used for reservoir mapping.

Integrating well and seismic data bring distinctive advantage for the delineation of the reservoirs but it carries two main difficulties; information and resolution contained in different data types. In general, seismic data is dependent on the acoustic properties of the subsurface but the well log data can provide rock and fluid properties and core data allow direct measurement of the rock properties in the vicinity of the borehole. Seismic data scale is expressed in meters, however well log and core data contain information from cm to mm scale.

The main objective of this study is to study the relationship between seismic and reservoir properties. Particularly, a relationship will be extracted between seismic attributes and reservoir properties at the well locations and this relationship will be used to estimate the reservoir parameters over the whole reservoir area.

To accomplish this task, first a methodology will be established to prepare, interpret and create a model from the available data set. Second, missing log sets will be predicted using empirical and artificial neural network techniques. Third, seismic inversion techniques will be reviewed and acoustic impedance property will be calculated. Fourth, several seismic attributes will be extracted from the well locations and a non-linear relationship will be established between the seismic attributes and well log properties. Geostatistical and artificial neural network techniques will be used to create this connection, then, outcome of each technique will be compared and finally the best relationship will be used to predict the reservoir properties over the whole study area.

1.2 DATA BASE

In this section, available data and the geology of the study area will be described. The data set used in the study is publicly available as a part of the technology transfer activities of the Secondary Gas Recovery (SGR) program funded by the U.S. Department of Energy and the Gas Research Institute (Hardage et al., 1996). The study area (Boonsville) is located in Fort Worth Basin in North-Central Texas (Figure 1.2).

The data set includes:

- 3-D seismic data, time migrated, 5.5 mi²
- 38 wells, digitized
- Various logs inside the 3-D survey area
- Interpreted genetic sequences from well logs
- Petrophysical and reservoir engineering data
- VSP (Vertical Seismic Profile) and CS (Check Shot) data for one well

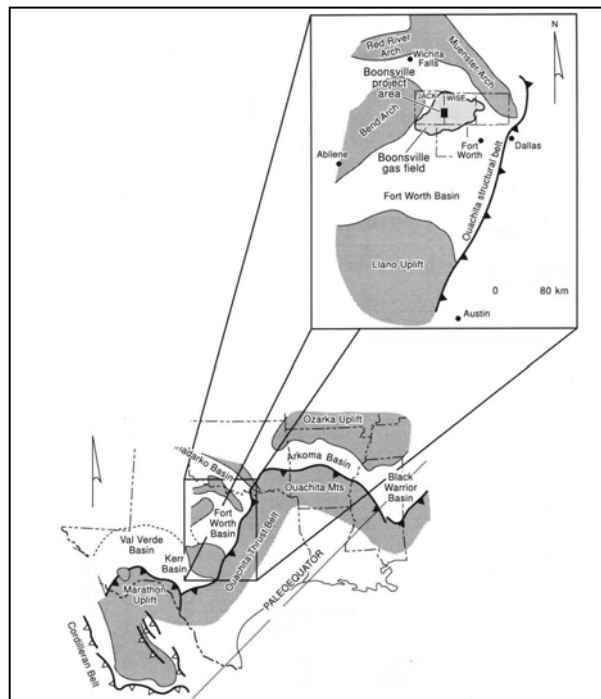


Figure 1.2 Fort Worth and other basins around the study area Boonsville over the Middle Pennsylvanian paleogeographic map. Rectangle (filled in black) in the enlarged map presents the 3-D seismic area (Hardage et al., 1996).

3-D time migrated seismic data set was collected with a dynamite source and having 110x110 ft stacking bins with a datum of 900 ft. It has a high signal to noise ratio and wide frequency range varying from 10 Hz to 115 Hz. Seismic data have 0 to 2,000 ms vertical time range and 1 msec sampling interval (Figure 1.3).

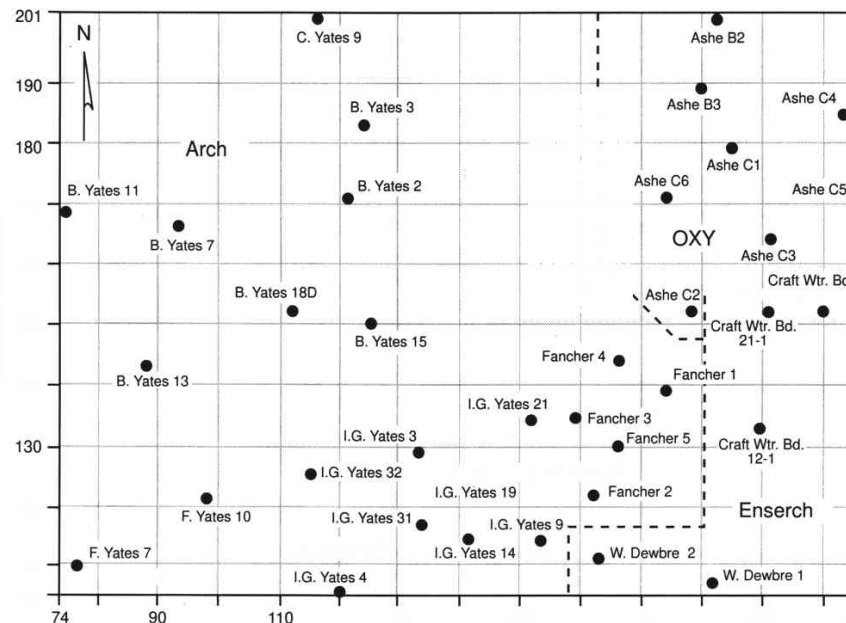


Figure 1.3 Seismic base map and well locations over the study area (Hardage et al., 1996).

There are 38 wells available inside the study area and all the wells were digitized from processed field records with 0.5 ft depth increment. Intensity of the wells over the seismic grid is 0.37 sq km/well. As it can be seen in Figure 1.4, 34 wells have deep-induction resistivity (RILD) logs and some wells have various other resistivity type logs including Medium-Induction (RILM), Short-Normal (SN), Spherically focused (SFL) logs. All the wells have Self-Potential (SP) logs and 18 wells have Gamma-Ray (GR), 12 wells having Compensated Neutron (NPHI) and 14 wells have Bulk Density (RHOB) logs. There are 4 wells with Sonic (DT) log in the study area and only one of them has VSP and CS surveys which is located in the central-west of the region. VSP data was recorded with a vibroseis source for only one well and consist of an offset and zero-offset profiles. Well B-Yates 18D has also a checkshot survey recorded with an explosive source.

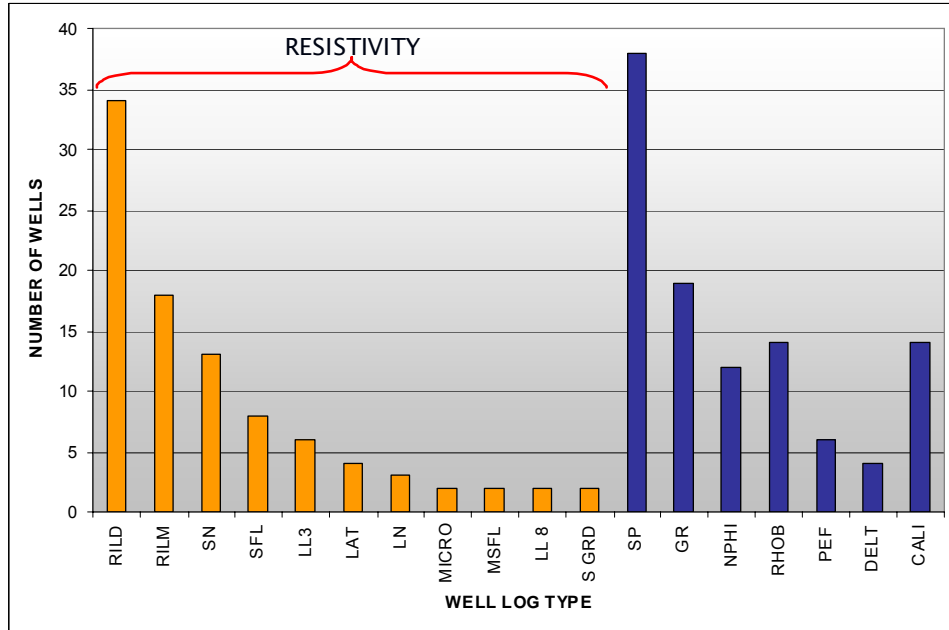


Figure 1.4 Log types histogram in the study area. Resistivity logs are abundant among the wells and SP exists for all wells.

General structural settings and the geology of the area can be summarized as following: The Fort Worth Basin defined as an asymmetric, wedge-shaped basin containing approximately 12,000 ft (3657 m) of sedimentary rocks along the west side of the Muenster arch. During a late Mississippian–early Pennsylvanian episode of plate convergence, this foreland basin formed in front of the advancing Ouachita structural belt as it was thrust onto the margin of the North America craton. The Bend arch is a large, north-plunging, subsurface anticline that extends northward from the Llano uplift. Pennsylvanian and younger sediments were deposited on the Eastern shelf of the Permian Basin and shaped by the arch which represents the westernmost limit of a migrating hinge zone. The Ouachita structural front bounds the basin to the east and southeast, the Llano uplift to the south, and the Muenster and Red River arches to the north and northeast, and the Bend arch to the west (Hill et al., 2007) (Figure 1.5).

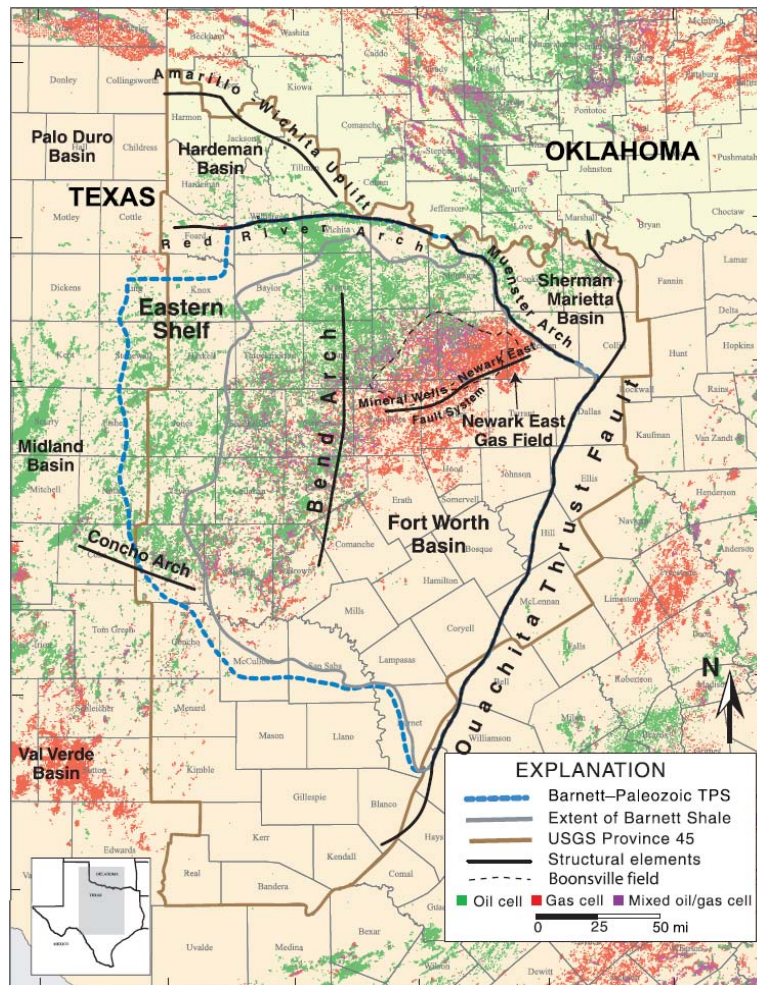


Figure 1.5 Bend arch - Fort Worth Basin with major structural features and location of oil and gas fields (Hill et al., 2007).

Structural style of the basin is mostly represented by minor high-angle normal faults and graben-type features. These structures are believed to be changing their orientations depending on several major tectonic elements. For instance, at Boonsville and Newark East fields, well data showed that many normal faults trend NE to SW (Hill et al., 2007). A study conducted by Hardage et al. (1996) also showed that small-scale faulting and local subsidence in Mississippian to middle Pennsylvanian strata is related to karst development and solution collapse in the underlying Ordovician Ellenburger Group. A generalized Pennsylvanian stratigraphic column for the Fort Worth Basin and the interpreted sequence boundaries is shown in Figure 1.6. Defined interval of the Bend Conglomerate is from the base of the Caddo Limestone to top of the Marble Falls Limestone and its thickness ranges from 1,000 to 1,200 ft (305 to 365 m) (Hardage et al., 1996).

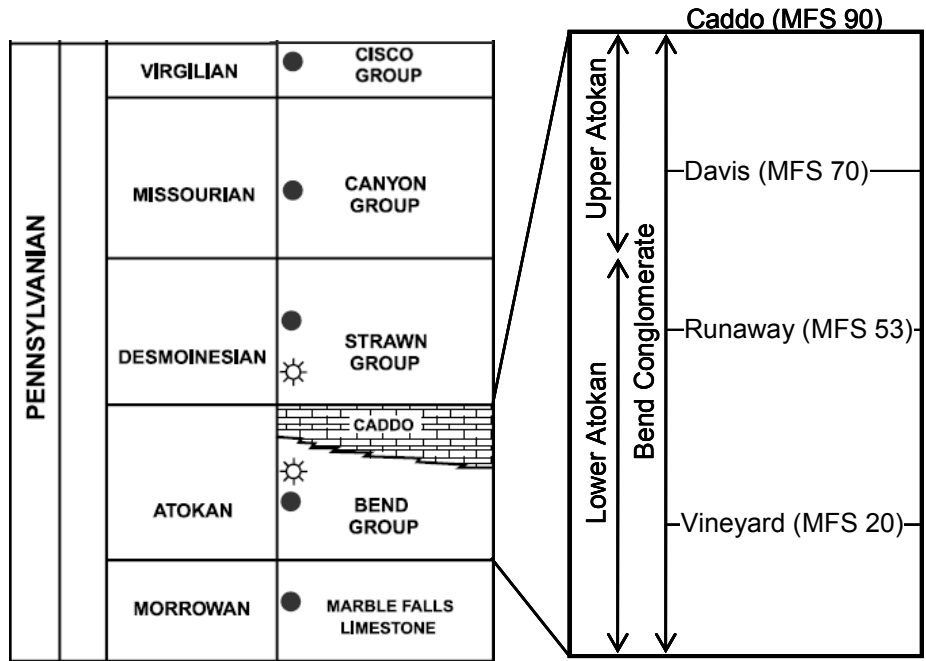


Figure 1.6 Generalized Pennsylvanian stratigraphic column for the Fort Worth Basin. The data provided for this study is limited to Atokan interval (modified from Zhao et al., 2007 and Hardage et al., 1996). Four Maximum Flooding Surface (MFS), from Caddo to Vineyard, represent the interval used in this study.

In particular, the Boonsville gas field is located deep on a moderately-sloping eastern shelf of the relatively narrow, northern part of the Fort Worth basin. The lower Pennsylvanian (Atokan) beds and older rocks dip northeasterly into the basin trough, The Atokan appears to enter into a more shaley and finer clastic facies to the east and southeast, deeper into the Fort Worth basin. In the area conglomerates are thicker, more porous, and more frequent than in the other parts.

The Atokan is divided into two parts. The "lower" Atokan top is clearly marked in the subsurface by the base of a fine grained, silty, glauconitic sandstone wedge, which pinches out to the northwest of the field and thickens rapidly and considerably to the southeast. The "upper" Atokan consists of silty sandstone wedge and a predominantly shale interval to the base of the Caddo (Gardner, 1960).

1.3 PREVIOUS STUDIES

In this section, previously published studies on the same data set and related to this research will be summarized. Because the data used in this study are available publicly through Bureau of Economic Geology, University of Texas at Austin, many researches conducted several studies.

The published report completed by Hardage et al. (1996) presented the details of the data set including data characteristics, structural, geologic, and stratigraphic information. Hardage et al. (1996) conducted a research on identifying carbonate karst collapse features and reservoir compartmentalization using 3-D seismic and well log data. Lancaster et al. (1996) summarized the application of 3-D seismic imaging, detailed sequence stratigraphy, petrophysical analysis, and reservoir engineering in an integrated study of reserve growth potential in Midcontinent (Pennsylvanian) sandstone natural gas reservoirs in the Boonsville (Bend Conglomerate Gas) field. The objectives of their work were to identify undrained or incompletely drained reservoir compartments controlled by depositional heterogeneity in a low-accommodation, cratonic Midcontinent depositional setting, and then, to developing and transfer strategies for infield gas reserve growth in these complex, difficult-to-characterize, fluvial and deltaic sandstone reservoirs. Lancaster et al. (1996) conducted a research on how to calculate facies from wireline logs using deterministic methods. Their study focused on developing a deterministic method for identifying facies from logs for use in the Boonsville Bend conglomerate, and out of several different approaches they used only one system. Their final system consisted of five different computational models, all using the same numerical technique but different wireline curve suites. Hamilton et al. (1997), focused on the reservoir compartmentalization. In their study, they integrated all available data, including geological, engineering and geophysical and identified three styles of compartmentalization: structural, stratigraphic and combination of two. McCormick et al. (1999), published a paper to describe a software tool and interpretation method for that allows one to combine well-based interpretation and quantitative analog information from fields or outcrops to make testable predictions about the location of geological bodies that are prospective infill drilling locations. This tool combines (1) 3D visualization in a common viewing environment of diverse data that are viewed at true scale (e.g., 3D

surface seismic; vertical seismic profiles, reservoir simulation results, conventional wireline and borehole imaging logs, core photographs); (2) a well-based interpretation environment; and (3) an archive of digital 3D geological analog shapes and textures that one can use to relate textures seen in image logs or core images to those observed in analog data, i.e., other fields or outcrops. The key advantages of their approach are that preserving information about the interpretation process and multiple hypotheses; viewing all data at the appropriate scale; and examining the implications of the deterministic geological interpretations within the same data volume. Hentz et al. (2006), presented depositional facies, reservoir distribution and infield potential of the Lower Atoka Group in the study area. Their study revealed that the units are bounded by mostly fourth-order flooding surfaces within prodeltaic shales and delta-plain coals. Lower Atoka Group depositional facies interpreted as more heterogeneous. Depositional trends shift from SE-NW to NE-SW midway in the succession, recording, respectively, a change in primary source area from the distant Ouachita Fold belt to the closer Muenster Arch. McDonnell et al. (2007) defined the seismically resolvable sag structures, and conducted a detailed quantitative analysis of the geometries of these circular features. They compared the results with reviews of subsurface collapse mechanisms and strike-slip processes that are known to produce subsurface circular to subcircular sag geometries in plan view. Finally, they described several constraints for differentiating collapse-related sag structures from strike-slip-related sag structures.

Xie (2001) completed a PhD dissertation using the same data set focusing on "Thin Bed Reservoir Characterization". In this study, two problems were addressed: estimating thin-bed reservoirs and distinguishing thin-bed sandstone reservoirs from thin-bed non-reservoir carbonates using seismic attributes. To build seismically driven depositional model and reservoir distribution, point-based and trace-based seismic attributes were employed. For the point-based application, he deployed 6 different seismic attributes and the results were not very satisfying. For the trace-based application, he applied Kohonen's self-organization (SOM) neural network recognition algorithm and obtained better results (correlation factor > 70%). He, then proposed a new algorithm for seismic facies analysis, which is a modified cross-correlation model. "Cross-correlation (R) (1.1) for the two series of signals $X(i)$ and $Y(i)$ ($i=1,2,3,\dots,N$):

$$R = \frac{\sum_i^N [(X(i) - X_m)(Y(i-d) - Y_m)]}{\sqrt{\sum_i^N (X(i) - X_m)^2} \sqrt{\sum_i^N (Y(i-d) - Y_m)^2}} \quad (1.1)$$

where X_m and Y_m are the means of the corresponding series and d is the delay. This correlation is representative of similarity of patterns between two time series rather than absolute similarity.” Therefore this expression was modified to (1.2):

$$R = \left(\frac{\sum_i^N [(X(i) - X_m)(Y(i-d) - Y_m)]}{\sqrt{\sum_i^N (X(i) - X_m)^2} \sqrt{\sum_i^N (Y(i-d) - Y_m)^2}} \right) \left(\frac{\sum_i^N |X(i)| - \sum_i^N |Y(i)|}{\sum_i^N |X(i)|} \right) \quad (1.2)$$

This equation allows for correcting possible horizon mistracking by searching an amount of time (d samples specified by the user) in order to find the highest value for R . The output values will be continuous from -1 to 1 and provide a value for every single trace for R .

To apply this equation to multiple user-specified traces, the following expression (1.3) can be used:

$$R = i * \max(R_1, R_2, R_3, \dots, R_i, \dots, R_n) \quad (1.3)$$

where, i is the order of the seismic trace, n is the number of traces selected, R_i is the correlation coefficient based on the selected trace.” As a result, it was concluded that “the coherence algorithm was not able to reveal subtle depositional facies in the thin Caddo sequence. The trace classification approach based on neural network clustering provided very good results.

In the second part of this study, thin-bed tuning models have been examined using seismic inversion techniques.

“After evaluating the conventional thin-bed tuning models, ‘A Novel Generalized Regression Neural Network Inversion’ (GRNN) was applied using four different seismic attributes as an input with 6 wells. As a result, sandstone reservoir sections were able to predicted using acoustic impedance cube.”

In the final part, a comparison study between different inversion methods was conducted. Two different inversion techniques were used: ‘Probabilistic Neural Network’ (PNN) and ‘Constrained Sparse Spike’ (CSSI). “As a result, all three inversion models were able to identify the thicker reservoir sandstones and non-reservoir limestones but the resulting details for thin-beds were varying.”

Tanakov (1997) studied the same data set in his MS thesis subjecting an integrated reservoir description of the field. In this study, first a linear velocity function was used to converted log data from depth to time and created synthetic

seismograms using three wells having sonic and density logs. Following time structure interpretation of the Caddo level, depth conversion was produced. Variogram analysis was performed on the extracted velocities at the well locations and results were krigged, and then multiplied with the time structure map to obtain the final depth map. In the second part of this work, 29 attributes were extracted at the well locations over the Caddo level within the several time windows. Then, results were cross plotted versus porosity values at the well locations to obtain the correlation coefficients (CC). Highest CC found for the seismic amplitude attribute having -0.615 value. Another 15 complex attributes run similarly and the highest CC observed for the quadrature attribute which is 0.690. After applying the spectral decomposition on the seismic volume, highest CC (0.726) found for the 80 Hz frequency value.

In the second part, porosity values at the well locations for the Caddo level mapped using variogram analysis. Then, a linear relationship was build with porosity to map permeability values. Porosities were mapped with kriging with an external drift using the extracted attributes having the highest CC. Same application was performed using cokriging algorithm also. Cokriging application repeated using a polynomial functions applying the regression analysis to the input variables. The results of this analysis were not satisfying then the cokriging results. Permeability was also mapped using the similar techniques.

In the final part, flow simulation, history matching and production forecast for secondary oil recovery (SOR) were performed.

CHAPTER 2

THEORETRICAL BACKGROUND

Geostatistics is a widely used tool to combine highly accurate but less sampled well data with the less precise but more sampled 3D seismic data. The usage of geostatistical tools can give reservoir property estimation, uncertainty and risk assessment to models. On the other hand, it can easily be derived incorrect models if the principal assumptions are neglected. It should be clearly and carefully analyzed that if these methods are valid under the studied data set.

Hirsche et al. (1998) stated very clearly in their paper how one can avoid drawbacks of the geostatistical methods during reservoir characterization studies. Gathering all available data is the first step in all reservoir characterization studies. It should be noted that poor quality seismic and/or well log data can only result in a poor reservoir characterization and the data should always be treated depending on its reliability.

Well logs are considered to be "hard" or precise data because the measurements are made in the borehole around the sides of the formation with a diversity of tools that are directly related to the reservoir properties (ie. density, porosity and permeability). Generally the well logs are acquired for a long period of time and different logging and processing parameters can bring an artificial bias in the petrophysical parameters. This effect can dangerously degrade the calibration between well and seismic data. In most cases the properties are averaged to assign a representative value of porosity (or other parameters) for the reservoir zone. Therefore, well to seismic calibration can seriously be affected by this averaging (Hirsche et al., 1998).

The surface seismic data is less consistent than well log data because it is made remotely and only indirectly related to the reservoir properties (ie. amplitude is proportional to reflectivity which is proportional to the changes in acoustic impedance which is proportional to density, etc.). Even high quality seismic data can have problems because of processing artefacts. In general the seismic attributes used in reservoir characterization are extracted from the 3D seismic volume. The quality of the interpretation is directly related to the quality of the attribute extracted. As a result, if the data quality is not good, it should not be expected that geostatistical methods will provide a satisfactory solution (Hirsche et al., 1998).

Subsurface are usually contaminated by associated uncertainty, linked uncertainty, different scaling problems. Therefore, unconventional approaches bring an alternative solution such as soft computing tools (Nikraves, 2001 and Aminzadeh, 2005). Among them Artificial Neural Networks (ANN) were first introduced by McCulloch (1943) and became very popular in recent years. ANN can be considered as a non-linear processing application that uses biological neuron as a model. Therefore, classification, pattern matching, and clustering can be performed via learning and training. Traditional mathematical approaches, on the other hand, works well for exact computations (Aminzadeh and de Groot, 2006).

In general, ANN is an attempt to simulate the human neural system and adapt artificial systems through software. These algorithms have parallel processing capabilities not only by programming but also by training and adaptation.

A 'node' or 'unit' is defined as a basic computational element (model neuron) (Figure 2.1) and it receives input from other units. 'Weights' (w) are associated to each input can be modified so that the model starts to learn. The, function 'f' of the weighted sum of inputs is computed. 'Net input' to unit i (or net_i) is defined as (2.1) (Krose and Smagt, 1996):

$$y_k = f\left(\sum_j w_{jk} y_j\right) + \theta_k \quad (2.1)$$

where; w_{jk} : weight from unit j to unit i and F : unit's activation function

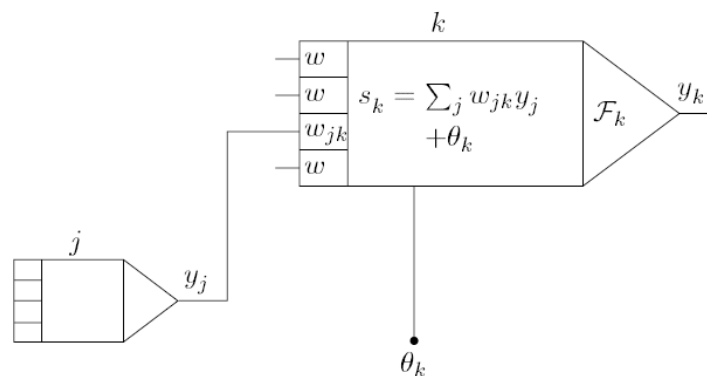


Figure 2.1 The basic components of an artificial neural network. Standard weighted summation propagation rule is used in this figure (modified from Krose and Smagt, 1996).

Estimating the reservoir properties was usually established by constructing the system using known properties with the help of attributes extracted from seismic,

well log, core etc. data. This study is followed typically by predicting the properties in desired locations using the extracted non-linear relationship. In previous figure, the inputs can be considered as seismic, well core etc. data and the output can be the desired reservoir property.

The comparison of the geostatistical and intelligent systems can be summarized as following (Table 2.1):

Table 2.1 Comparison of geostatistical and intelligent systems (modified from Nikravesh and Aminzadeh, 2001).

GEOSTATISTICAL	INTELLIGENT
Data assumption: A certain probability distribution	Data assumption: Data automatic clustering and expert-guided segmentation. Classification of relationship between data and targets
Model: Weight functions come from variogram trend, stratigraphic facies, and probability constraints	Model: Weight functions come from supervised training based on geological and stratigraphic information
Simulation: Stochastic, not optimized	Simulation: Optimized by Genetic Algorithms (GA), Simulated Annealing (SA), ANN, and Belief Networks

The reasons of choice of ANN for prediction studies were summarized briefly by Aminzadeh and de Groot (2006) as:

- Incoherent or contaminated data can be handled
- Unpredictable situations can be handled by using information from other disciplines
- Relevant information can be extracted quickly from large amounts of input
- Parallel working logic brings performance advantages
- It is fault tolerant and even if some of the connection does not work the whole system continues to work
- Alters itself to new situations and learns from example

2.1 GEOSTATISTICAL METHODS

In geostatistics, statistical distribution of the reservoir properties are estimated based on some assumptions and it is important to be sure that the data satisfy these assumptions. Constructing a geologic model is also an important step of the whole process as it guides the choice of tools used in geostatistical analysis.

The first step during the data analysis is to review the quality and consistency of the data. One of the methods is to generate histograms of the reservoir and seismic parameters. To obtain a reliable distribution for well based parameters is difficult due to fact that intensity and sample sizes are small and sampling is biased. If the distribution exhibits skewness or multiple peaks, this can imply the non-normal distribution or non-stationarity case. Establishing a relationship between seismic attributes and petrophysical properties can easily affected by outliers in the data set. They should be removed to obtain a better spatial correlation. On the other hand, they can exhibit value from another population. If this is the case, they must be treated separately without simply removing.

One of the drawbacks of the geostatistical techniques is that the assumption of the mean and variance of the reservoir properties derived from the well locations is representative of the entire field. This assumption is usually not the case for exploration studies as the drilled wells always targeted to specific objective and this practice create a bias on the statistical sampling of the reservoir.

Statistical stationarity is the assumption that the statistics (i.e. mean and variance) of the population (reservoir) are consistent throughout the study area. Existence of trends in the study area can cause non-stationarity case. This can be checked by cross-plotting against mean value of the reservoir property in different parts of the reservoir. Trends should be removed before the mapping and modeling practices. Another reason for non-stationarity case is the changes in lithology, facies, or fluid saturation. For example, if wells from the channel sands and the shales are treated as a single population the variance would be overly large and the average value of porosity could be completely unrepresentative. This can be overcome subdividing the data into separate populations and mapping within each group independently.

Finding a correlation between seismic attributes and reservoir properties is simply an empirical relationship. Usual approach to establish such a relationship

starts with extracting certain number of attributes over a horizon or through the well path and crossplot against the reservoir properties. Using bivariate statistics linear relationship between two variables is established.

Synthetic seismograms also provide a good approach for selecting the seismic trace locations where attribute extraction should be done as they provide the best match between synthetic and real seismic traces. Seismic attributes often need some amount of smoothing prior to extraction. This relationship can be established using the correlation coefficient (CC). It is the measure of the linear dependency of the two variables and it carries associated uncertainty. This uncertainty can be removed by detecting the outliers in the data set.

Seismic attributes are generally considered to be the best information that may be related to reservoir properties. For example, the product of seismic inversion, acoustic impedance, is related to porosity, lithology and saturation. Correlating the attributes and the properties are directly related to number of measurement which is the number of wells in the reservoir characterization studies. Generating synthetic seismic traces over the pseudo-wells can improve the reservoir property estimation procedure. Building a spatial relationship between these variables is another step for correlation. Creating a variogram model and deriving maps using kriging associated with error help estimating reservoir properties between the wells using weighted average of the property values. This practice generally is followed by cokriging to include other variables. Uncertainties can be assessed using the cross validation techniques.

Journal (1994) provides a good summary of the stochastic algorithms:

A stochastic simulation (imaging) algorithm is a mechanism that allows drawing alternative, equiprobable, spatial distributions of objects or pixel values. Each alternative distribution constitutes a stochastic image. There can be several stochastic images of the same phenomenon and each stochastic image/realization/outcome honors (1) specific statistics, such as a histogram, covariance, variogram, or correlation coefficient; for example, the simulated facies can be made to honor volume proportions, size distributions, aspect ratios, etc., and (2) hard and soft data at specific locations. Hard data, such as well data, are reproduced exactly by all realizations, whereas soft data are reproduced with some degree of tolerance.

From the constraining statistics and data honored, one cannot say that one realization is better than another. Yet, the various stochastic images differ one from another at locations away from the hard data locations. That difference provides a visual and quantitative measure of uncertainty about the properties being imaged (Journal, 1994).

“The family of “sequential” procedures all makes use of the same basic algorithm shown in Figure 2.2:

1. Choose at random a grid node at which we have not yet simulated a value.
2. Estimate the local conditional probability distribution (LCPD) at that location.
3. Draw at random a single value from the LCPD.
4. Include the newly simulated value in the set of conditioning data.
5. Repeat steps 1 through 4 until all grid nodes have a simulated value.”

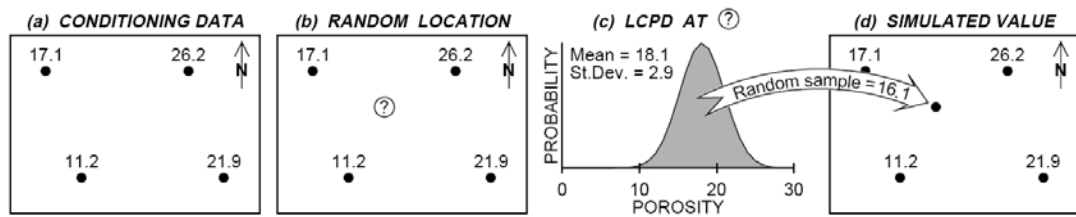


Figure 2.2. Sequential simulation of an unknown porosity value in a layer (modified from Srivastava, 1994).

The characteristic geostatistical study for reservoir characterization has following steps (Chambers et. al., 2000):

1. Data gathering and preparation (including initial quality control)
2. Data loading
3. Exploratory Data Analysis
 - a. univariate and multivariate statistical analysis
 - b. identification and probable removal of outliers
 - c. identification of sub-populations
 - d. data posting
 - e. sampling of seismic attributes at well locations
4. Spatial Continuity Analysis
 - a. calculation of experimental covariance model
 - b. interpretation and modeling
5. Search Neighbourhood Design
6. Model Cross-Validation
7. Spatial Interpolation of Reservoir Properties
8. Conditional Simulation of Reservoir Properties
9. Model Uncertainty Assessment

The continuity of sample properties with distance and direction are defined by regionalized variables. For instance, property values of two wells expected to be similar if they are close together but as they become apart values tend to be different. In this point univariate or bivariate statistics cannot distinguish this spatial information.

Univariate (Single-Attribute) Geostatistics

Statistical analyze of a single variable usually performed with calculating the mean, variance and the standard deviation. The results displayed in histogram or over the map and spatial information were tried to extract.

Randomly selected values z from a set of random variable Z can be called as a realization. The first moment (mean) of the random variable (expected value) of Z is given by the integral over the realizations z of Z (Wackernagel, 2003):

$$E[Z] = \int z \cdot p(z) dz = m \quad (2.2)$$

where; E : expected value, $p(z)$: weights and m : mean. The second moment can be defined as an expectation of its squared value:

$$E[Z^2] = \int z^2 \cdot p(z) dz = m \quad (2.3)$$

Variance can be defines as the average squared difference of the observed values from the mean. The variance σ^2 of the random variable Z can be given as:

$$\sigma^2 = \text{var}(Z) = E[Z^2] - (E[Z])^2 \quad (2.4)$$

Above equation gives the result of the difference between the second moment and the squared first moment. Because the variance involves squared differences, this statistic is very sensitive to high/low values.

Bivariate Geostatistics

These methods carry information about relationship between two variables and spatial content of a random function for each observation. The relationship is generally analyzed by looking at how one variable changes to another observing the values; direct increase or decrease of values in variables. Scatter plot is one of the methods of defining the linear relationship as a positive or negative and showing the outlier points. H-scatterplot analyzes the spatial continuity of the data by displaying all sample pairs which are separated by specific distance in a certain direction. Sample point cloud also shows if the relationship getting stronger or not (Geovariances, 2008).

“The theoretical covariance σ_{ij} between two random variables Z_i and Z_j can be defined as” (Wackernagel, 2003):

$$\sigma_{ij} = \text{cov}(Z_i, Z_j) = E[(Z_i - E[Z_i]) \cdot (Z_j - E[Z_j])] = E[(Z_i - m_i) \cdot (Z_j - m_j)] \quad (2.5)$$

where m_i and m_j are the means of the two random variables.

Correlation Coefficient (CC) defines the relationship between two variables in a range of +1 and -1. Theoretical correlation coefficient can be obtained by dividing the covariance by the square root of the variance:

$$\rho_{ij} = \frac{\sigma_{ij}}{\sqrt{\sigma_i^2 \sigma_j^2}} \quad (2.6)$$

Regionalized Variable and Random Function

Regionalized value is defined as each value measured at the location in the given domain. *Random variable* assumes that regionalized value is outcome of some random system. At each point x_α , this system produces sample value of $z(x_\alpha)$ from a random variable $Z(x_\alpha)$.

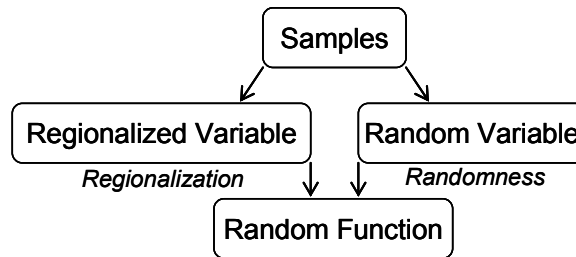


Figure 2.3 The random function model (modified from Wackernagel, 2003)

Figure 2.3 shows that how the data is treated in the random function model. First, data values dependent on the location in the domain which means that they are regionalized. Second, simple generalized function cannot be used to model complex behaviour of the regionalized sample values. Therefore, the data values considered as outcomes of the *random* system (Wackernagel, 2003).

Properties in the hydrocarbon reservoirs can be thought as random functions which has *regionalized* and *random* variables. Two components of a random function area:

- Structured Component, consisting of the regionalized variable, which exhibits some degree of spatial auto-correlation

- Local Random Component, consisting of the random variable (also referred to as the nugget effect), showing little or no correlation

Stationary Assumption

Stationary assumes that the random function keep the same properties when moving from one location to another in a given region. The mean of the data values is not depending on the distance (h) separating the data points (x_α). Expected value of the difference between two random variables is zero (2.7). This is also called *translation invariance*. Note that stationary is a part of the random function model not the regionalized variable (Wackernagel, 2003).

$$E[Z(x_\alpha+h)-Z(x_\alpha)] = 0 \text{ for all } x_\alpha, h \quad (2.7)$$

where; $Z(x_\alpha)$, $Z(x_\alpha +h)$: random variables, E : expected value, x_α : sampled location h : distance between sampled locations.

Strict stationary assumption is also requires the simplification of the distribution of the points. For instance, Gaussian distribution characterize only first two moments (*second order stationary*). *Intrinsic stationary* characterizes the first two moments of the pair of values which employs the variogram concept (Wackernagel, 2003).

“Stationarity is defined through the first-order (mean) and second-order (variability) moments of the observed random function, and degrees of stationarity correspond to the particular moments that remain invariant across the study area” (Hohn, 1998). For a random variable, $Z(x_\alpha)$, observed at location x_α , the distribution function of $Z(x_\alpha)$ has the expectation $E Z(x_\alpha) = m(x_\alpha)$ which can depend upon x . This is the first-order moment. Three second-order moments are useful in geostatistics:

1. The variance of the random variable $Z(x_\alpha)$:

$$\text{VAR } Z(x_\alpha) = E [Z(x_\alpha) - m(x_\alpha)]^2 \quad (2.8)$$

2. The covariance:

$$C(x_{\alpha1} - x_{\alpha2}) = E [Z(x_{\alpha1}) - m(x_{\alpha1})] [Z(x_{\alpha2}) - m(x_{\alpha2})], \quad (2.9)$$

where $Z(x_{\alpha1})$ and $Z(x_{\alpha2})$ are two random variables observed at locations $x_{\alpha1}$ and $x_{\alpha2}$,

3. The semivariogram function:

$$\gamma(x_{\alpha1}, x_{\alpha2}) = \text{VAR} [Z(x_{\alpha1}) - Z(x_{\alpha2})] / 2 \quad (2.10)$$

Under conditions of second-order stationarity, the semivariogram and covariance are alternative measures of spatial autocorrelation (Hohn, 1988).

Non-Stationary Data

The sampling scale and the trend scale are the dependency of the data considered to be non-stationary. Even though sample distribution is not usually under control, enough sampling can make the data stationary. Non-stationary data can be thought of composing of two parts, the residual and the trend:

$$Z(x_\alpha) = Y(x_\alpha) + m(x_\alpha) \quad (2.11)$$

where; $Y(x_\alpha)$ has an underlying variogram (residual), $m(x_\alpha)$ can be approximated by a polynomial (trend). If the data is abundant, the trend can be ignored, but if it is sparse, the trend should be removed performing the following the steps (Isaaks and Srivastava, 1988):

1. "Stationarize" the data,
 - a. determine the trend on the sample data (trend surface analysis)
 - b. subtract the trend from the data (usually from the well data)
2. Compute the variogram (or correlogram) on the residuals,
3. Obtain kriging or conditional simulation of the residuals on the grid,
4. Krig the trend to the grid,
5. Calculate the final gridded results by adding residuals to the trend.

Spatial Continuity Analysis

Linear relationships usually cannot describe the phenomenon of the subsurface properties. Spatial auto-correlation assumes that variables close to each other exhibit a relationship depending on the distance. As a result, values can be predicted using other samples. Measuring the spatial continuity can be done using variogram and correlogram (auto covariance).

In case of two variables, z_1 and z_2 , a *residual* can be measured by multiplying the difference between a value of a variable and its mean and *experimental covariance* becomes the products of average of the residuals (Wackernagel, 2003):

$$s_{12} = \frac{1}{n} \sum_{\alpha=1}^n (z_1^\alpha - m_1^*)(z_2^\alpha - m_2^*) \quad (2.12)$$

The covariance shows the power of the relationship with its absolute value and similarity or dissimilarity of two variables with its sign. If the units of the variables are different and not comparable, each variable were need to be standardized. The standardized variable is given as:

$$\tilde{z} = \frac{z - m^*}{s} \quad \text{where; } s: \text{ standard deviation and } m: \text{ mean} \quad (2.13)$$

The measure of the dissimilarity (γ^*) between data values z_α and z_β which are located at points x_α and x_β is defined as:

$$\gamma_{\alpha\beta}^* = \frac{(z_\alpha - z_\beta)^2}{2} \quad (2.14)$$

If these two points are linked by a vector h ($x_\alpha - x_\beta$), dissimilarity can be rewritten depending on the spacing and orientation (Wackernagel, 2003):

$$\gamma^*(h) = \frac{1}{2}(z(x_\alpha + h) - z(x_\alpha))^2 \quad (2.15)$$

Plotting dissimilarities against the separation vector produces the *variogram cloud*. The average dissimilarity versus separation vector defines the *experimental variogram* (Figure 2.4):

$$\gamma^*(h) = \frac{1}{2n} \sum_{\alpha=1}^n (z(x_\alpha + h) - z(x_\alpha))^2 \quad (2.16)$$

The auto covariance function (Wackernagel, 2003), measures similarity or correlation, versus separation distance instead of dissimilarity (Figure 2.4).

$$C(h) = \frac{1}{n} \sum_{\alpha=1}^n [z(x_\alpha) - m] \cdot [z(x_{\alpha+h}) - m] \quad (2.17)$$

where; m is the sample mean over all paired points, $n(h)$, separated by distance h .

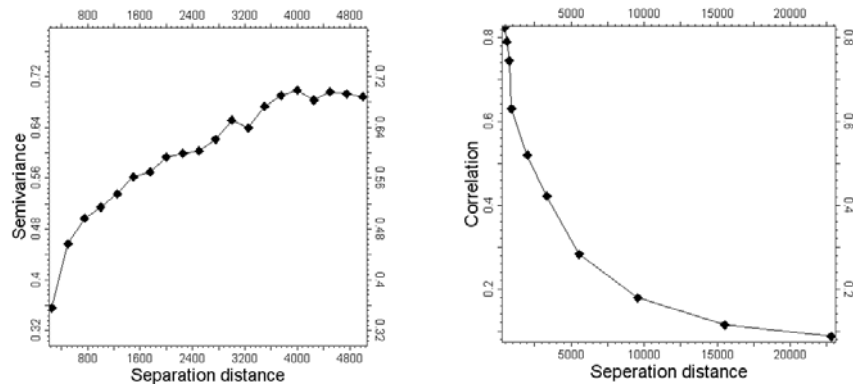


Figure 2.4 Omni-directional variogram and correlogram. The left panel shows omnidirectional variogram (increasing dissimilarity with distance) and the right panel represents the correlogram (decreasing correlation with distance). Origin of the two plots shows zero variance (Geostatistics, 2008).

Creating variograms on the same data set with different directions can represent the influence of the anisotropy (Figure 2.5).

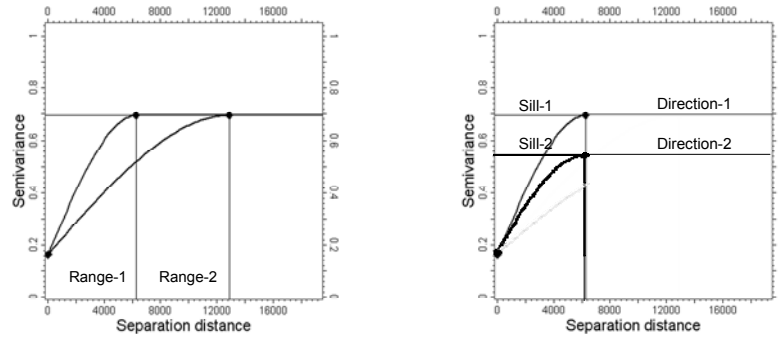


Figure 2.5 Geometric and zonal anisotropy. The left frame shows same sill in same direction with different ranges which characterize the geometric anisotropy, the right frame has different sills but same range for changed directions representing the zonal anisotropy (modified from Chambers et. al., 2000).

In general, variograms and correlograms can measure linear spatial dependence, quantify spatial scales, identify and quantify anisotropy and test multiple geological scenarios. On the other hand, for non-linear processes they may not be the best solution because they represent the linear spatial relationship. If the data is not abundant, variogram analysis cannot be performed.

Spatial relationships of two or more variables can be performed using cross-correlation study. Cokriging or conditional simulations can benefit from cross correlogram or variogram as they compare the known values of one variable to known values of different variable (e.g., matching well data with seismic data). The cross variogram between two variables can be calculated as (Wackernagel, 2003):

$$\gamma_{ij}(h) = \frac{1}{2n} \sum_{\alpha=1}^n [(z_i(x_{\alpha} + h) - z_i(x_{\alpha})) \cdot (z_j(x_{\alpha} + h) - z_j(x_{\alpha}))] \quad (2.18)$$

where; z_i : primary attribute, z_j : secondary attribute and n : number of data points.

Kriging

One of the most well-known geostatistical techniques is the kriging which use the variogram models to exhibit the autocorrelation function between the data points. In *simple kriging*, estimation of a random variable $Z(x_{\alpha})$ from the known variable(s) z measured at locations x_{α} with the following assumptions; a) the random variables are subset of a random function $Z(x)$ at any location x , b) the random function is second order stationary (the expectation and the covariance are both translation invariant over the given domain) which means that the mean of the expected value $E[Z(x)]$ is same at any point x and the covariance depends only on

the separation vector h not on the location and c) the mean is known (Davis, 2002 and Wackernagel, 2003):

$$E[Z(x+h)] = E[Z(x)] \quad (2.19)$$

$$\text{cov}[Z(x+h), Z(x)] = C(h) \quad (2.20)$$

Simple kriging estimation using a calculated average constant mean (stationary assumption) over the whole domain with the knowledge of the covariances between the random variables is (Wackernagel, 2003):

$$Z^*(x_0) = m + \sum_{\alpha=1}^n w_{\alpha} (Z(x_{\alpha}) - m) \quad (2.21)$$

where; w_{α} : weights attached to the residuals $Z(x_{\alpha})-m$. The estimation error is then:

$$Z^*(x_0) - Z(x_0) \quad (2.22)$$

In *ordinary kriging*, an unknown value of a point in a given region with a known variogram can be estimated using the data in the neighborhood.

$$Z^*_{OK}(x_0) = \sum_{\alpha=1}^n w_{\alpha} Z(x_{\alpha}) \quad (2.23)$$

where x_0 : unknown value, w_{α} : weights

The entire weights sum up to one and all the data values and the value to be estimated should be equal to constant in ordinary kriging. In simple kriging, there is no constraint on the weights. Ordinary kriging is an exact interpolator as (Wackernagel, 2003):

$$Z^*(x_0) = Z(x_{\alpha}), \text{ if } x_0 = x_{\alpha} \quad (2.24)$$

Cross Validation

This technique controls the relationship between the estimated and real data values. First, a value of $Z^*(x_{[\alpha]})$, where sampled value Z_{α} is excluded, is estimated using the $n-1$ other samples, then makes the comparison.

$$Z(x_{\alpha}) - Z^*(x_{[\alpha]}) \quad (2.25)$$

Equation 2.25 shows how the estimated value at this location closes to the surrounding data values. In more general terms, validation can be expressed as (Wackernagel, 2003):

$$\frac{1}{n} \sum_{\alpha=1}^n ((z(x_{\alpha}) - Z^*(x_{[\alpha]})) \quad (2.26)$$

Comparing the estimated values to the true values provides a re-estimation error; $RE = Z_{est} - Z_{true}$, calculates the standardized error; $SE = RE / \sigma_{krig}$, then averages the errors for a large number of target points. Any data point whose absolute Standardized Error ≥ 2.5 is considered an outlier, based on the fact that the data point falls outside the 95% confidence limit of a normal distribution (Figure 2.6).

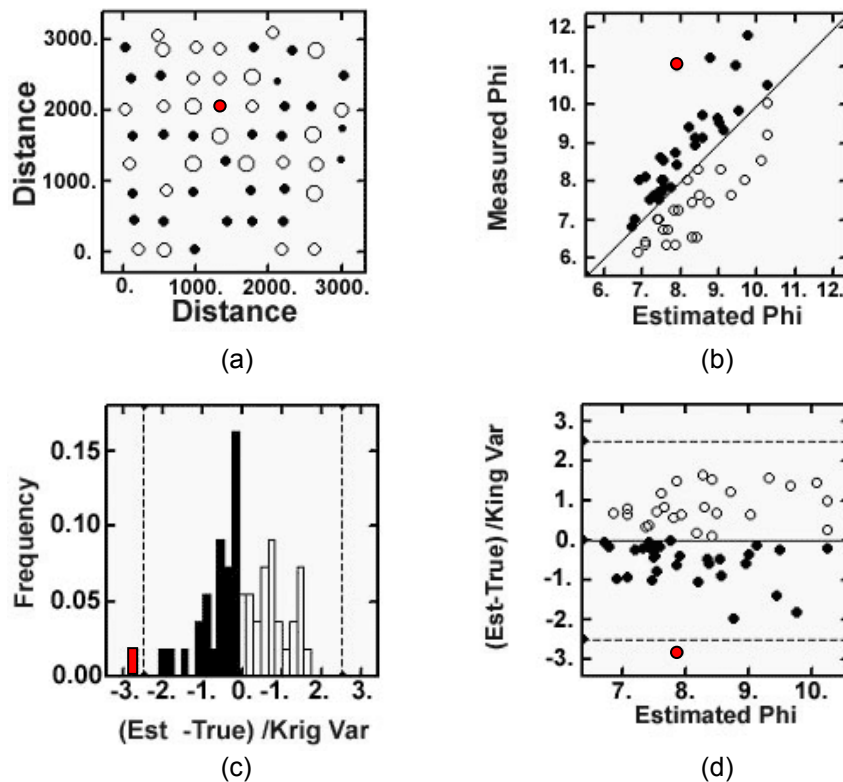


Figure 2.6 Cross validation example. (a) Re-estimation error where open circles are over estimations; solid circles are under-estimations. The solid red circles falls outside the 2.5 standard deviation from a mean, (b) measured attribute versus re-estimated attribute with cross validation test, (c) histogram of standardized error and (d) estimated versus standardized error (existence of correlation present a possible bias) (courtesy of IHRDC, 2009).

Multivariate Geostatistics & Cokriging

Estimating a sparse variable using abundant one or more variables brings a need for multivariate regression methods. Among them, cokriging is the most widely used technique. Data characteristics for the multivariate case can be summarized as follows (Figure 2.7):

- a) Entirely heterotopic data: the variables have no common sample locations
- b) Partially heterotopic data: some variables have some common sample locations
- c) Isotropic data: all variables share same sample locations

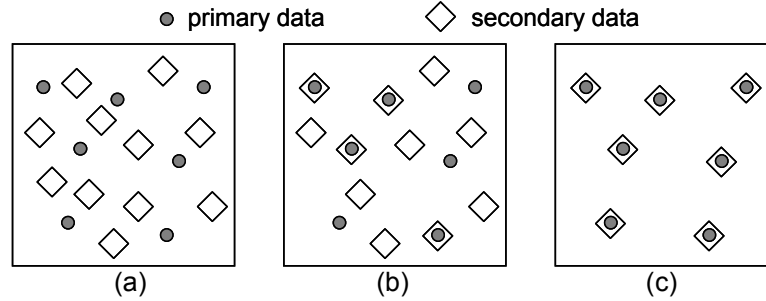


Figure 2.7 Isotropy and heterotopy. (a) Entirely heterotopic data, (b) partially heterotopic data and (c) isotropic data (modified from Wackernagel, 2003).

From data analysis we might find a good correlation between a property measured at well locations and a certain seismic attribute. In such a case, we might want to use the seismic information to provide better inter-well estimates than could be obtained from the well data alone. Even when the number of primary (well) data (e.g., porosity) are sparse, it is possible to use a densely sampled secondary attribute (e.g., seismic acoustic impedance), in the interpolation process. Well data have excellent vertical resolution of reservoir properties, but poor lateral resolution. Seismic data, on the other hand, have poorer vertical resolution than well data, but provide densely sampled lateral information. Geostatistical data integration methods allow us to profit from on the strengths of both data types, to yield higher quality reservoir models.

Simple cokriging variable estimation can be performed using the means of the variables and the residuals without existence of any data value around the estimation point x_0 (such as well locations). The mean is specified explicitly and assumed to be a global constant. The method uses all primary and secondary data according to search criterion (Wackernagel, 2003).

$$Z_{i_0}^*(x_0) = m_{i_0} + \sum_{i=1}^N \sum_{\alpha=1}^{n_i} w_{\alpha}^i (Z_i(x_{\alpha}) - m_i) \quad (2.27)$$

Ordinary cokriging is similar to simple cokriging in that the mean is still assumed to be constant but defines the estimation of point x_0 in partially heterotopic case. Linear combination of weights w_{α}^i of other variable(s) placed around the point x_0 .

$$Z_{i_0}^*(x_0) = \sum_{i=1}^N \sum_{\alpha=1}^{n_i} w_{\alpha}^i Z_i(x_{\alpha}) \quad (2.28)$$

where; i_0 : particular variable from set of N variables.

Collocated cokriging is performed if the interested variable is exist at few locations and secondary variable is located all locations. In this system, a neighborhood defines the subset of a given data around the estimation location. Figure 2.8 shows three different neighborhoods for a single estimation location.

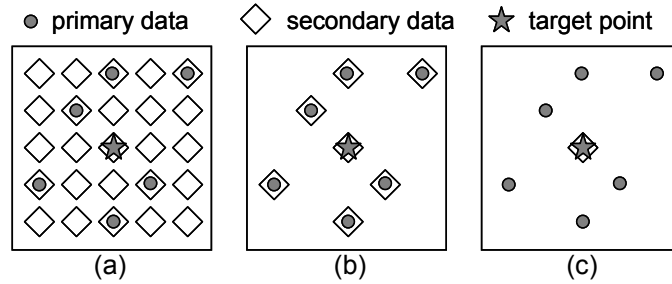


Figure 2.8 Three different neighborhood cases. a) Full neighborhood, b) multicollocated neighborhood and c) collocated neighborhood data (modified from Wackernagel, 2003).

Collocated simple cokriging can be used for collocated neighborhood data (Figure 2.7, c). Collocated simple cokriging uses CC instead of cross-covariance function as the secondary variable is exist only on the estimation point. If the value $S(x_0)$ is collocated with the target point $Z(x)$, the estimator becomes (Wackernagel, 2003):

$$Z^*(x_0) = m_z + w_0(S(x_0) - m_s) + \sum_{\alpha=1}^n w_{\alpha} (Z(x_{\alpha}) - m_z) \quad (2.29)$$

In collocated ordinary cokriging, the weights of the secondary variable should sum up to zero and therefore, secondary variable was not used by the system. This system uses $S(x_{\alpha})$ along with the $S(x_0)$. For the multicollocated neighborhood data (Figure 2.7, b), the ordinary cokriging estimator is:

$$Z^*(x_0) = w_0 S(x_0) + \sum_{\alpha=1}^n (w_z^{\alpha} Z(x_{\alpha}) + w_s^{\alpha} S(x_{\alpha})) \quad (2.30)$$

Cokriging and collocated cokriging techniques can be summarized as:

- Correlated secondary data can be used into the estimation process.
- Secondary data can be incorporated via a cross-covariance model (cokriging) or through the correlation coefficient (collocated cokriging).

- The cokriging technique honors the primary data (wells) and collocated cokriging uses correlation coefficient for data locations away from the wells (Dubrule, 1998).

The Figure 2.9 presents the illustrative examples of cokriging and collocated cokriging.

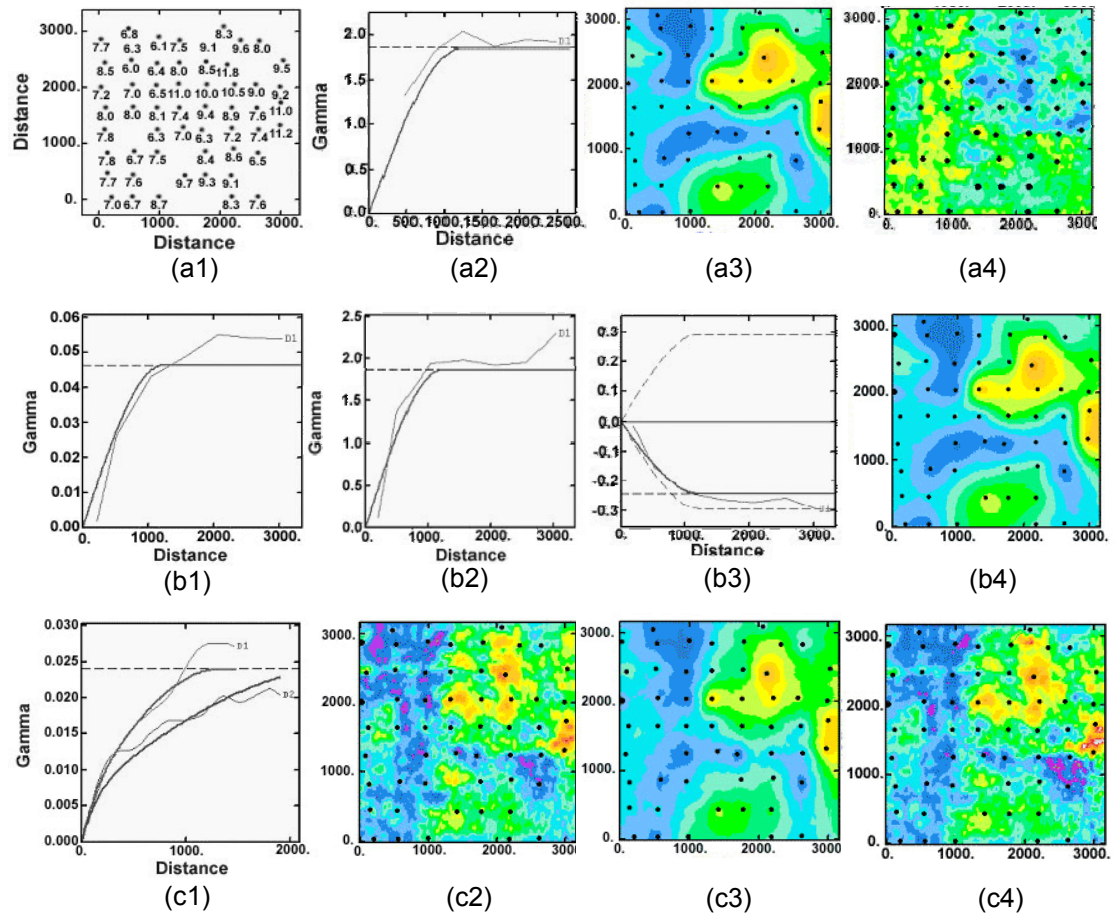


Figure 2.9 Kriging, cokriging and collocated cokriging examples. (a) Kriging using only well data. (a1) Data points from wells, (a2) variogram model for the well data, (a3) kriged porosity data and (a4) seismic acoustic impedance (AI) data. (b) Cokriging example using well and AI data. (b1 and b2) Modeled variograms for porosity and AI data, (b3) cross variogram and (b4) results of kriging using cross variogram. (c) Collocated cokriging and kriging with external drift examples. (c1) Modeled variograms, (c2) result of collocated cokriging, (c3) self kriging and (c4) result of kriging with external drift (courtesy of IHRDC, 2009).

Conditional Simulation and Uncertainty Estimation

Traditionally, lithological units or reservoir properties were analyzed well to well and the results produced usually were showed either connected units or pinch

outs between wells. As a result, mapped units or properties were created smooth contours disregarding the higher frequency content in the subsurface (Srivastava, 1994). Stochastic modeling addresses the conventional modeling approaches as it produces many realizations of the subsurface including associated risk and uncertainty.

Reservoir models always carry an associated uncertainty; on the other hand performance of the result usually performed using the “best” outcome. As the stochastic models offers many outcomes, the up- and down-sides of the results should be carefully handled with the related risk. Considering the heterogeneity in the subsurface is another important step during reservoir simulation studies (Chambers et. al., 2000).

Basically, conditional simulation is used to:

- honor primary and secondary data and spatial covariance model
- make appropriate data transformations
- assess uncertainty in the reservoir model

Srivastava (1994) summarizes the simulation methods as:

- Turning Bands
- Sequential Simulation
 - Gaussian, Indicator, and Bayesian
- Simulated Annealing
- Boolean, Marked-Point Process and Object Based
- Probability Field
- Matrix Decomposition Methods

Turning Bands, first produces a smooth models using kriging and then adds some level of noise to be able to include the heterogeneity of the subsurface. Sequential type of simulations uses the following methodology (Chambers et. al., 2000):

- a. A random grid node x_i which is not simulated yet,
- b. Estimate the mean (m_i) and variance (σ_i^2) at location x_i using kriging from the local conditional probability distribution (LCPD) having zero mean and unit variance,
- c. Select a random value (r_i) using a seed number from the probability distribution whose maximum deviation is $\pm 2\sigma$ around m_i ,

- d. Create a new simulated value $X_{si}^* = m_i + r_i$,
- e. Place newly simulated value X_{si} into data set,
- f. Repeat the steps above until all grid nodes have values.

Sequential Gaussian Simulation (SGS) is used to model continuous properties, such as porosity, permeability etc. In Sequential Indicator Simulation (SIS), discrete variables, e.g. lithologies, facies are simulated. Bayesian Sequential Indicator Simulation (BSIS) provides the usage of seismic attributes combining with the well data (Doyen et. al., 1994). Simulated Annealing (SA) creates the reservoir model using iterative trial and error procedure and does not include the explicit random function model. The resulting model is formulated with an optimization process (Deutsch and Cockerham 1994). Boolean, Marked-Point Process and Object Based methods require priori knowledge of the object (lithofacies) geometries, specific proportions and distribution parameters of the geometries. Probability Field Simulation (PFS) technique computes the LCPD using only the well data in contrast to SGS method where each value picked from the LCPD is considered as a hard data (Srivastava, 1994). Matrix Decomposition methods create different outcomes by multiplying vectors of random numbers by a precalculated matrix obtained from variogram or correlogram (Srivastava, 1994).

Conditional simulations create more realistic reservoir models than those of kriging type models as they have an ability to reproduce the data histogram and structure of the spatial correlation. Hydrocarbon volumes can be simulated in a reasonable manner because simulations can reproduce extreme values. Simulations can create equi-probable reservoir models with associated uncertainty. On the other hand, Models with large data can require more powerful computer specifications. Simulation results are very sensitive to variogram parameters (sill, nugget, CC etc.). Variability between realizations of the same data can be large if the input data is not dense. Even though all the realizations can equally be probable, some of them cannot reflect the real subsurface conditions (Dubrule, 1998 and Chambers et. al., 2000).

2.2 ARTIFICIAL NEURAL NETWORKS

Intelligent computational systems become more popular in the past few years especially for the oil industry. These systems can be classified into two categories: The first group is the tasks related to improvement for the processing and manipulation of the data used in exploration studies and the second group is the studies associated to pattern recognition, identification and prediction of different rock properties. The latter task is done by training the known rock properties from well logs, cores, tests, surface seismic, etc. Then, the extracted relationship is used to predict the properties in the locations where there is no measurement available (Nikravesh, M., 2001).

In general, neural networks are built by processing elements (nodes) organized in a certain structure. Nodes are similar to biological neurons that they can learn, remember, and apply relationships through training.

A Simple Artificial Neuron

A 'node' or 'unit' is defined as a basic computational element (model neuron) and it receives input from other units (Figure 2.10). 'Weights' (w) are associated to each input can be modified so the model starts to learn. Then, function ' f ' of the weighted sum of inputs is computed. 'Net input' to unit i (or net_i) is defined as:

$$y_i = f\left(\sum_j w_{ij}y_j\right) \quad (2.31)$$

where; w_{ij} : weight from unit j to unit i and f : unit's activation function

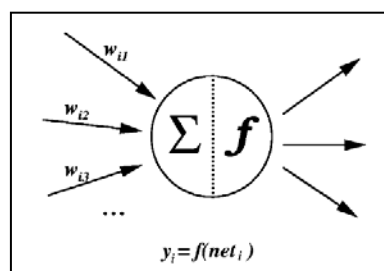


Figure 2.10 Basic elements of artificial neural network (modified from Schraudolph and Cummins, 2009).

A linear model can be defined as: $y = w_1x + w_0$ and a sum-squared error (E) (Figure 2.11) can be written as:

$$E = \frac{1}{2} \sum_p (t_p - y_p)^2 \quad (2.32)$$

where; t_p : target value (actual) and y_p : model's prediction

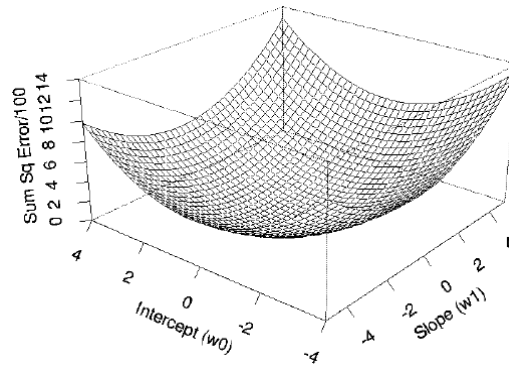


Figure 2.11 Sum-squared error model. Error for a range of values of w_0 and w_1 as a contour map (modified from Schraudolph and Cummins, 2009).

Minimizing the Error

'E' gives the predictive error for specific model parameters chosen. Therefore, the best (linear) model can be found by minimizing the error. For linear models, linear regression can be used but this approach cannot be used for non-linear models. Even for linear models, the minimal error can be calculated using iterative methods. One of them, gradient descent, follows the below sequence:

- Choose random initial values for the model parameters
- Calculate the gradient 'G' of the error function with respect to each model parameter
 - Change the model parameter to be able to move in the direction of '-G' (decrease of the error)
 - Repeat steps until 'G' gets close to zero

The gradient of 'E' shows the direction in which the loss function at the current setting of the 'w' has the steepest slope. To decrease 'E', move to the opposite direction, '-G' (Figure 2.12) (Schraudolph and Cummins, 2009)

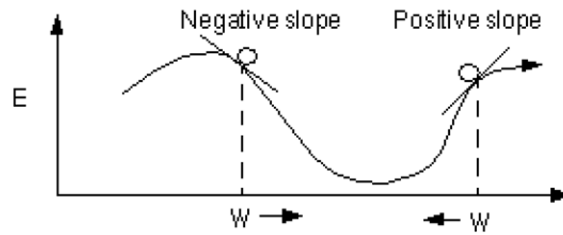


Figure 2.12 Error function and its relation to w (modified from Schraudolph and Cummins, 2009).

Linear Model to Neural Network

Equation $y = w_1x + w_0$ can be expressed as a simple ANN as (Figure 2.13):

$$y_2 = w_{21}y_1 + 1.0w_{20} \quad (2.33)$$

where; y_2 : output unit, $w_{21}=w_1$: slope of the straight line, $w_{20}=w_0$: interception with the y-axis, and 1.0 : bias

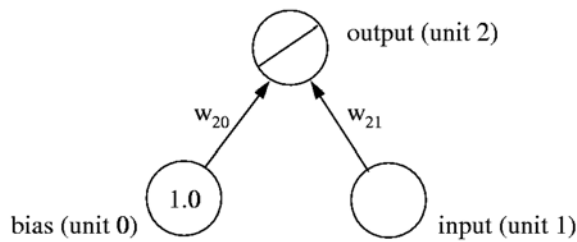


Figure 2.13 Simple artificial neural network elements (modified from Schraudolph and Cummins, 2009)

Learning Rate

Learning rate, μ , determines how much the weights, w , should change at each step. If μ is too small, it will take a long time the algorithm to converge. If μ is too large, the algorithm diverges (Figure 2.14).

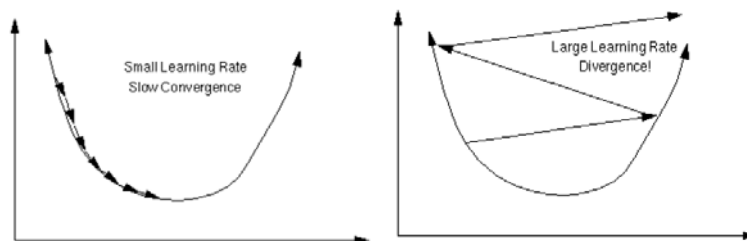


Figure 2.14 Effect of learning rate on the ANN process (modified from Schraudolph and Cummins, 2009).

Multi-Layer Networks

Additional nodes can be employed to create a best non-linear fit to data using non-linear activation functions. Figure 2.15 shows an extra node with an activation function and a hidden node. Note that hidden unit also has weight from the bias unit.

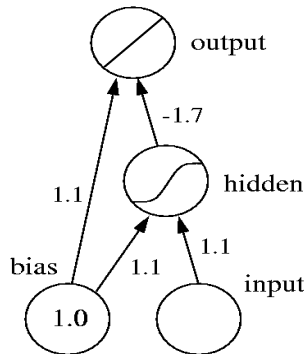


Figure 2.15 Multi-layer network with a hidden node and activation function (modified from Schraudolph and Cummins, 2009).

Hidden Layers

Adding more hidden units into network can fit more complex models. On the other hand, too many hidden layer can degrade the network's performance. Therefore it always a good practice to start the network with a small number of hidden units. Theoretical results indicate that given enough hidden units can approximate any reasonable function to any required degree of accuracy. In other words, any function can be expressed as a linear combination of hyperbolic tangent (*tanh*) functions which is a universal basis function, for instance, sigmoidal and radial basis functions.

Error Backpropagation

For the multi-layer networks, there are no target values for the hidden units. Re-ordering the units from a group closer to input to a group closer to output creates non-cycle pattern it is called feedforward networks (Figure 2.16). To train the network based on some training data, first; the gradient needs to be calculated, second; the activity of the input unit is determined by the network's external input, for the other units, the activity is propagated in forward direction, and third; the output error is calculated and for hidden nodes, the error must be back propagated from the output nodes (Schraudolph and Cummins, 2009).

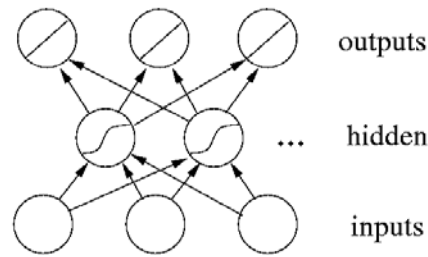


Figure 2.16 Multi-layer network pattern. The network does not have to be organized in layers, any pattern of connectivity that permits a partial ordering of nodes from input to output is allowed (modified from Schraudolph, N., and Cummins, F., 2009).

Overtraining (Overfitting)

Producing a reasonable approximation usually requires knowledge of number of hidden units or weights. Figure 2.17 shows two fitted functions.

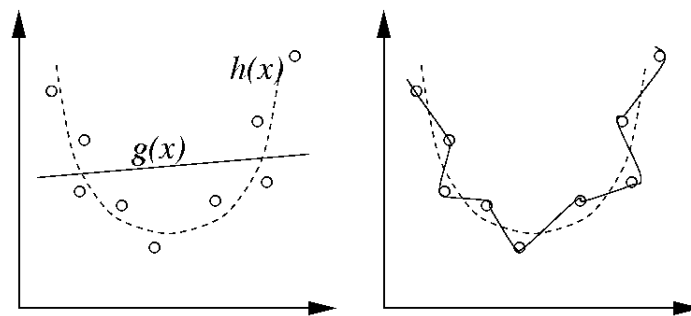


Figure 2.17 Overtraining phenomenon. Functions $g(x)$ and $h(x)$ show different characteristics to fit the data points in circles (modified from Schraudolph and Cummins, 2009).

Function $g(x)$, naturally, does not fit well the data points, as it has only two intersections; this is called a high biased model. Second plot in Figure 2.17 fits the data points very well but it is not able to predict the new values of $h(x)$; this is called high variance model.

To avoid overtraining, the input data is divided into two sets. Training set is used to train the network, and the performance of the network is done by validation set. No weight updates is performed during validation as this data set is independent of the training data. Avoiding overfitting, the network can be stopped at time t where the performance of the validation set is optimal (Figure 2.28) (Schraudolph and Cummins, 2009).

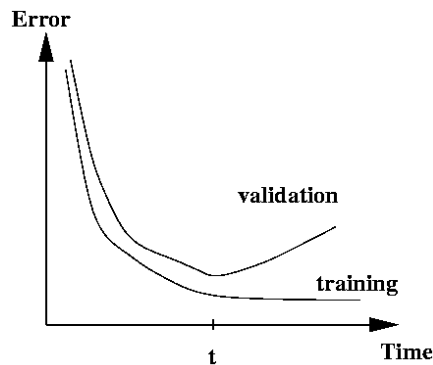


Figure 2.18 Schematic learning curves for the training and validation sets. Overtraining can be avoided by stopping the learning at time t (modified from Schraudolph and Cummins, 2009).

Types of Learning and Training

There are two types of learning; parameter learning which updates the weights and structure learning which changes the node structures. For parameter learning, there are three different types of learning approaches: supervised reinforced, and unsupervised learning. In unsupervised learning, the structure of the data is tried to find. It learns itself; similar inputs activate similar neurons and different inputs activate other neurons. In supervised learning, correct target values are assumed to be known. The network tries to find the non-linear relationship between input and output variables by minimizing the error between predicted and actual values. Self Organizing Maps (SOM) uses this method. In reinforced learning, the feedback information is either right or wrong. Multi-layer perceptrons (MLP) and Radial Basis Functions (RBF) are examples of this network (Aminzadeh and de Groot, 2006).

Types of ANN

MLPs are the most commonly used models which are organized in layers. In general, it forms with three layers: an input, a hidden, and an output layer. There is no connections are allowed between nodes belonging to same layer. MLPs have the ability to extract the relevant features from the input pattern and discard the irrelevant ones and once trained it can recognize the input patterns which are not part of the training.

RBF neural networks have similar architectures as MLP networks but it differs with handling the weights and activation function. There are only weights between output layer and hidden layer and each node in the hidden layer has a

unique activation function, called the basis function.

Modular Neural Networks are built by cluster of individual neural networks that are connected to each other. Each network are controlled by a global expert acts as a decision maker. Global expert take the decisions and determine the importance of each network and combines them.

Self Organizing Networks trains and tests the data set with the known input and output values. Kohonen Self Organizing Map (KSOM) and the Unsupervised Vector Quantizer (UVQ) are examples of this type of network. GRNN and PNNs are the variants of the RBF network (Aminzadeh and de Groot, 2006).

ANNs usually do not require preprocessing of input data. On the other hand, Principal Component Analysis (PCA) and data equalization (balancing) can improve the results.

CHAPTER 3

DATA PREPERATION AND METHODOLOGY

As stated in previous chapters, the data used in this study consist of time-migrated 3D seismic data, 38 wells with various well logs, formation tops of sequence boundaries, and VSP and CS from one well in the area. For the initial state, all data were loaded into an interpretation system to be able to define the area of interest and quality checking.

3.1 METHODOLOGY

In this dissertation, a methodology was developed to achieve final objective (Figure 3.1). 3D seismic data was checked for low signal to noise problems and some filter were applied to data for amplitude enhancements. This was followed by building the time-depth relationship. Synthetic seismograms were prepared for the wells having sonic and density logs (B Yates 11, B Yates 18D, and C Yates 9). This work allowed correcting sonic velocities by adjusting synthetic curve to surface seismic inside the borehole. Creating T-D link was also allowed tying the formation tops to seismic data.

Selected four well tops (MFS 90, MFS 70, MFS 53, and MFS 20) will be interpreted though the whole area. Seismic time structure maps will be mapped and results will be converted to depth using the velocity model prepared with the velocity logs extracted from all wells inside the study area. Defining the area of interest will allow reducing the dimension of the data set. Then, fault modeling and re-gridding of the horizons will be preformed and new grid dimension was established in X-Y direction. Resolution definition in the Z direction will be built by defining the zones, thickness between the stratigraphic intervals, and layering scheme. At the end of this work, structural model of the area will be ready.

Because not all the well log sets available in the study area, missing logs will be estimated using empirical relationships and neural network techniques. The results will be compared and most promising outcomes will be used for further analysis.

In the geostatistical simulation part, empty structural model will be populated with the reservoir properties. To accomplish this, first well logs will be upscaled to model vertical resolution which is the layer thicknesses. Then, property values will

be distributed the area using Sequential Gaussian, Gaussian Random Simulations, and Kriging techniques.

Seismic inversion will be performed to obtain better resolution in the area and obtained acoustic impedances will be extracted from the well locations and will be used as an input for the neural network study.

Finally, neural networks will be employed to estimate properties in the study area. To accomplish this objective, training, validation, and estimation steps will be followed and the results will be compared to ones obtained from geostatistical analysis.

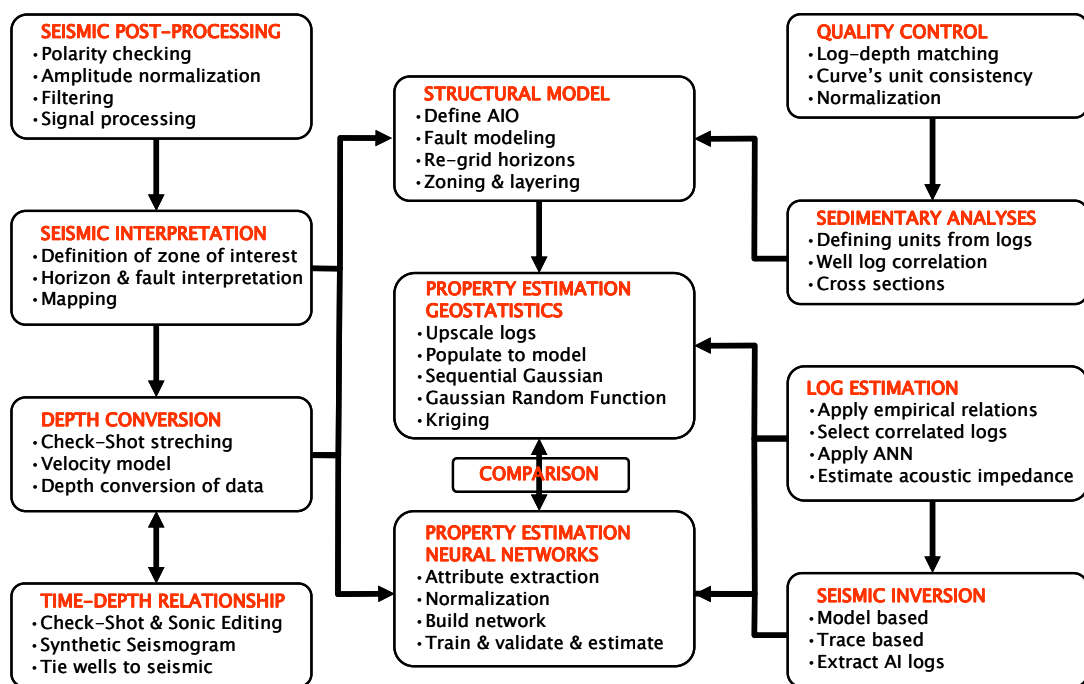


Figure 3.1 Methodology developed for this study. Workflow from data import to model construction to property estimation.

3.2 SEISMIC AND WELL DATA QUALITY CHECKING AND EDITING

First of all time-migrated 3D seismic data was loaded into an interpretation system and quality checked. Figure 3.2 shows the 3D seismic cube loaded.

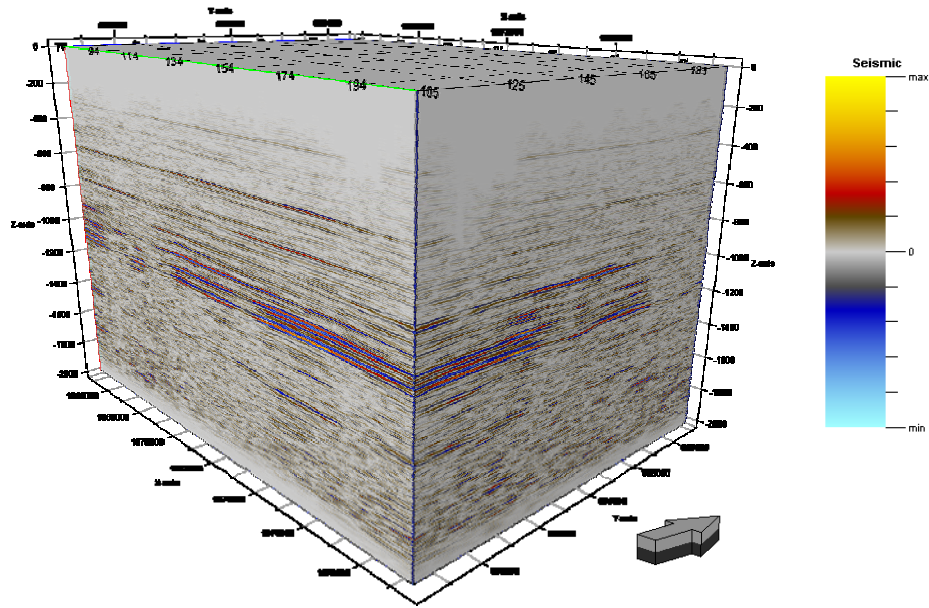


Figure 3.2 Time-migrated 3D seismic data used in this study.

The 3D seismic data is composed of 110x110 ft bins with a seismic reference datum of 900 ft. The total area constitutes a 10,670x14,630 ft (3,25x4,46 km) rectangle. It has a high signal to noise ratio and wide frequency range varying from 10 Hz to 115 Hz. Seismic data have 0 to 2,000 ms vertical time range and 1 msec sampling interval. The amplitude interval of the data is between -121405 to 149035. As it can be seen from above figure, the data quality is generally good around 600 to 1,200 ms.

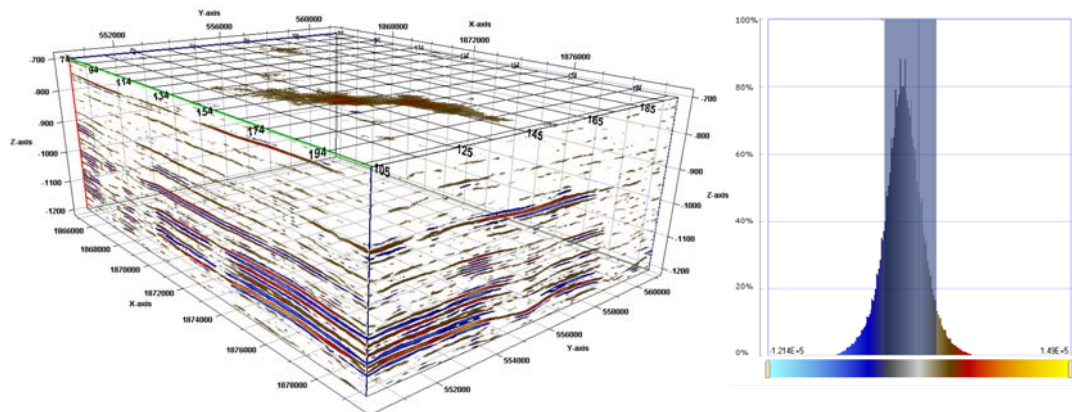


Figure 3.3 Cropped seismic cube and amplitude filter. Figure on the right shows the amplitude values on the x-axis and corresponding color as a histogram. Shadowing the colors (dark blue area) removes the corresponding amplitudes from the seismic cube.

Because the area of interest does not cover the whole cube, it was cropped between 700 and 1,200 ms where the data quality is high. To be able analyze the data quality on the cropped volume, an opacity volume was created and low amplitude values were diminished (Figure 3.3).

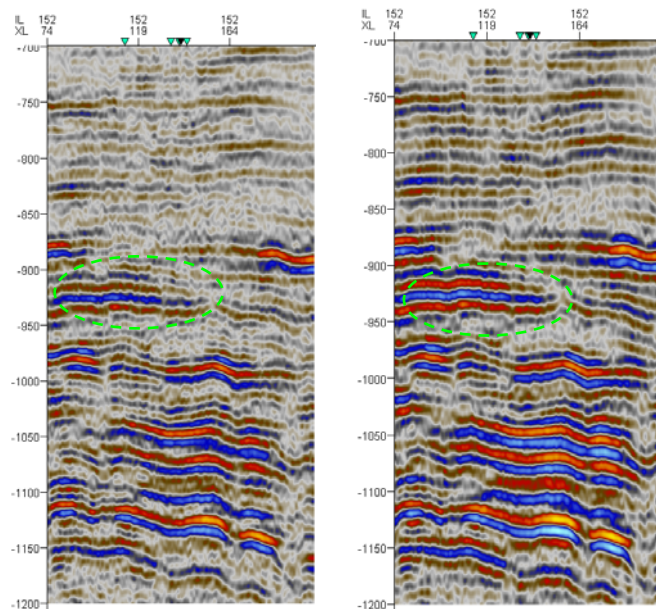


Figure 3.4 Original seismic in-line 152 and the result of frequency band filter. Boosting of the amplitudes can clearly be seen. Vertical axis is TWT in milliseconds.

Even though seismic quality is above average, some filters were applied to enhance the data resolution. Figure 3.4 shows the user-defined frequency band filter applied to input seismic trace.

Automatic Gain Control (AGC) and Quadrature amplitude are the other attributes for increasing the amplitude response in the seismic data. Figure 3.5 represents the differences between original seismic and the AGC applied section. In general post stack processing steps should be taken cautiously as they can artificial effect to original amplitudes. Among them, AGC can be considered as one of the most unsafe post processing steps. The main purpose of applying these filters to seismic data is solely for improving the continuity of the reflectors to help interpretation procedure. In the next chapters, amplitude extraction will be performed from the seismic data. This extraction will be done from the original seismic data directly; no post stack processed version will be used.

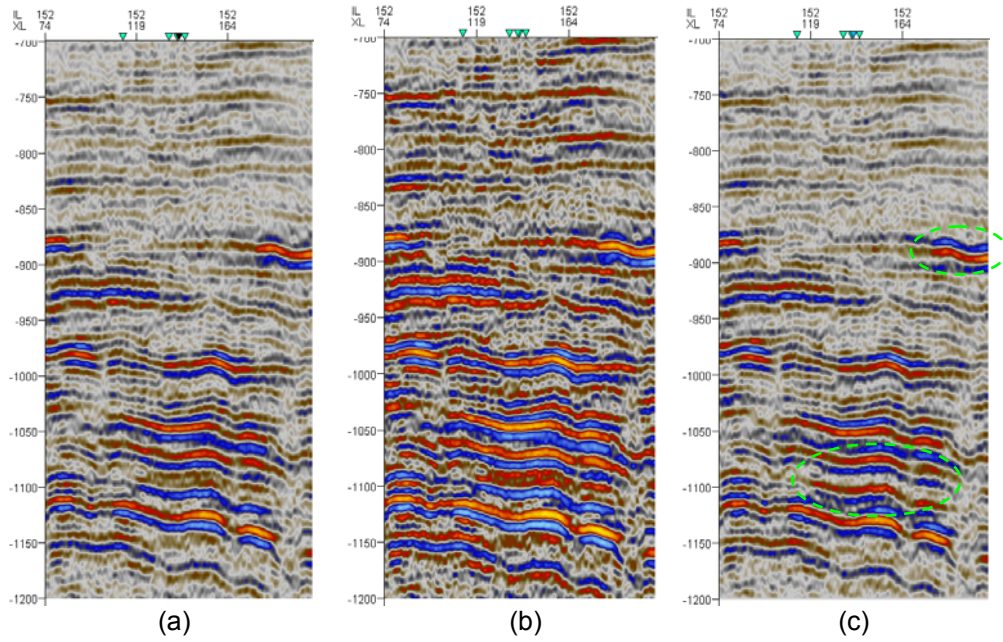


Figure 3.5 Amplitude enhancements for the in-line 152. a) Original seismic, b) AGC applied same section (RMS window is 9 for the AGC), and c) quadrature amplitude applied version. Vertical axis is TWT in milliseconds.

Figure 3.6 shows the existing wells on the basemap. The distribution of the wells in the area was good as they were not gathered in a specific partition.

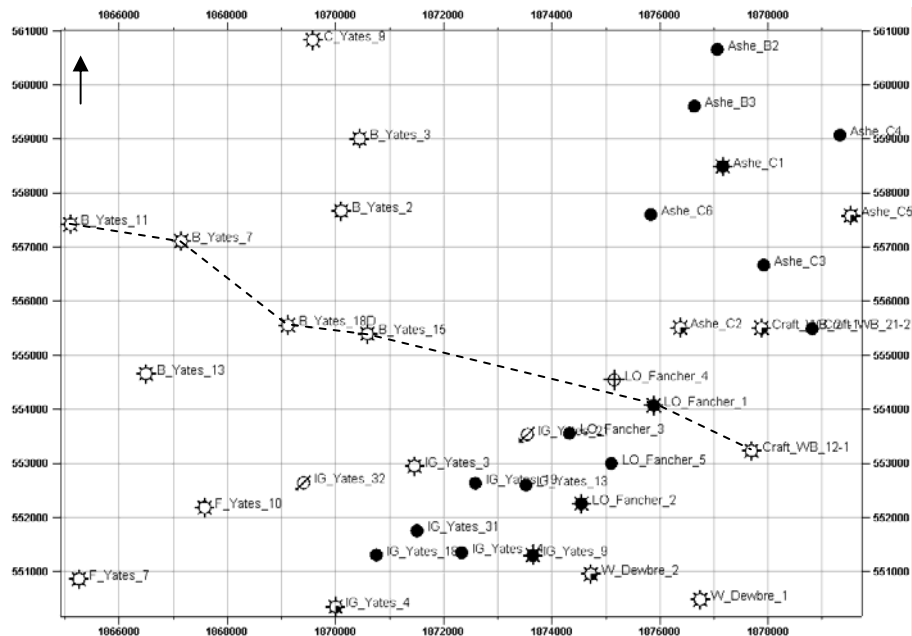


Figure 3.6 Basemap showing available wells inside the study area. Symbols show; ☀: gas, ●: oil, ☆: gas with minor oil, ✱: oil and gas, ⊘: injection, ⊕: abandoned wells respectively.

This situation will be very helpful when some relationship will established between the properties and seismic attributes. As it was mentioned above, there are 38 wells available inside the study area. Wells have various types of logs and all of them were loaded into the interpretation system. Please refer to Figure 1.5 for the list of the log types.

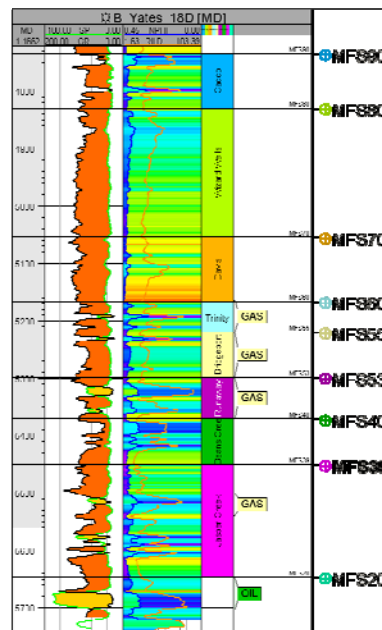


Figure 3.7 B Yates 18D type log. Figure shows SP and GR in this first track and NPHI and RILD in the second track.

It will also be useful for the neural network study as the training and validation set will be able to separate from each other while representing the whole area. Please refer to Appendix A for detailed explanation of the available well logs in the study area.

Several genetic sequence boundaries were available in the study area. Figure 3.7 shows loaded formation top for the aim of this study. Among these tops, MFS90 (Caddo), MFS70 (Davis), MFS53 (Runaway), and MFS20 (Vineyard) were used to interpret four horizons from the 3D seismic data. Full set of interpreted genetic sequences can be seen in Appendix A.

Figure 3.8 shows the NW-SE cross section with main formation tops in the study area. In general, logs are in good quality and continuous for most of the types. Please refer to Figure 3.6 for the location of the cross section. Please refer to Chapter 1 for more information about geological settings of the study area.

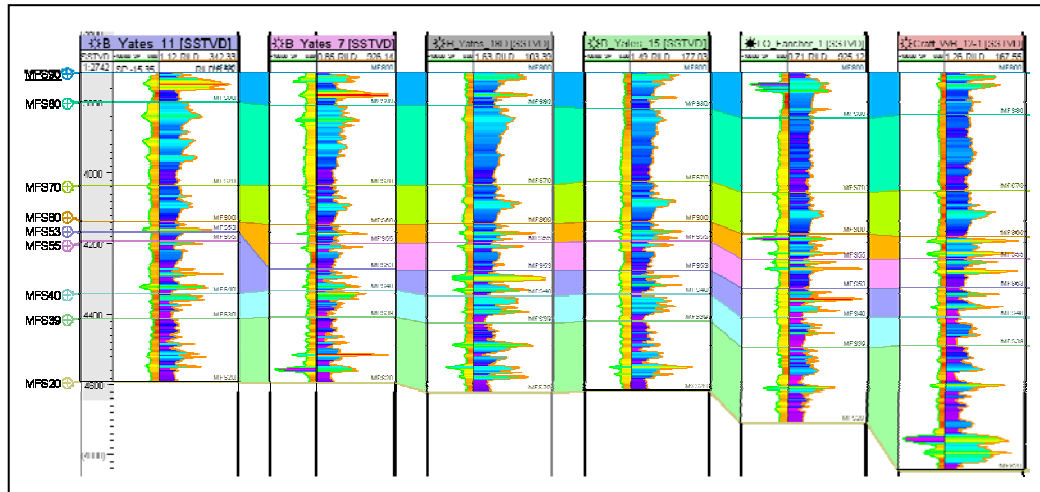


Figure 3.8 Well correlation section through North-West to South-East representing the formation tops used in this study. Refer to Figure 3.5 for the location of the cross section.

Well data generally contains some outliers due to acquisition and/or processing related activities. Regardless of the source of these extreme values, they need to be corrected, either removed or normalized, before using them especially for the study of correlation with the other type of information. The visualization of the log data can help for identifying the outliers. But better way to achieve this is plotting the log data is better way to search the outliers. Cross-plots not only represents the correlation between two or more variables but also give an information about how specific log values are correlated laterally from one well to another.

Figure 3.9 shows an example. Another usage of the cross plots is identifying the outliers. Because most of the simulation (estimation) algorithms are very sensitive to extreme values, they need to be removed from the data points before evaluation. In the first cross plot, there are some outliers indicated by dotted lines. They can be simply due to some measurement or processing errors or they can indicate some geological phenomenon. Therefore, extreme values should be treated carefully. In general, both DT-RHOB and DT-GR cross plots show coherent behavior through the area meaning that these property values do not change much laterally. These outliers should be removed with care as they can represent a specific geological phenomenon. Several cross plots were prepared, extreme values were removed from the log data and these logs were used for the further evaluation through in this study.

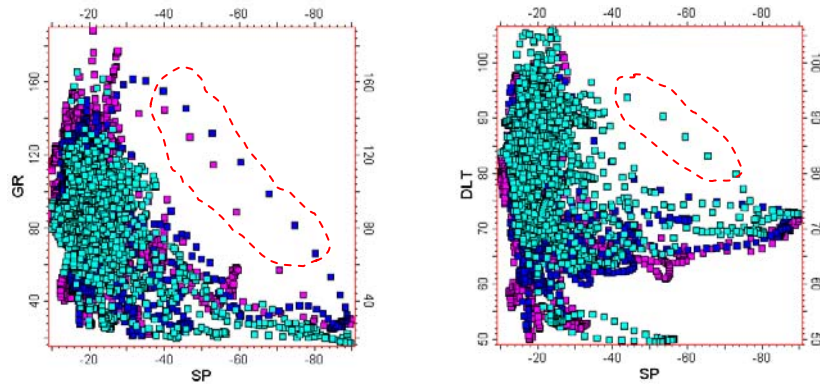


Figure 3.9 Log to log cross plot for wells B Yates 11, B Yates 18D, and C Yates 9. The first plot on the left is SP versus GR and the right plot presents SP versus DT. Each color in plots represents different wells.

3.3 SEISMIC TO WELL TIE

After loading all wells with corresponding well tops, time-depth (T-D) data were loaded into the system. In the study are, only available T-D data is check-shot (CS) data acquired from B Yates 18D well with a vibroseis and dynamite sources. Initially, this information was used to build a relationship between depth indexed well logs and seismic data. Figure 3.10 a shows the T-D graph for the Well B Yates 18D. The fit line shows good relationship with $y=1256.39+5.80*x$ linear correlation.

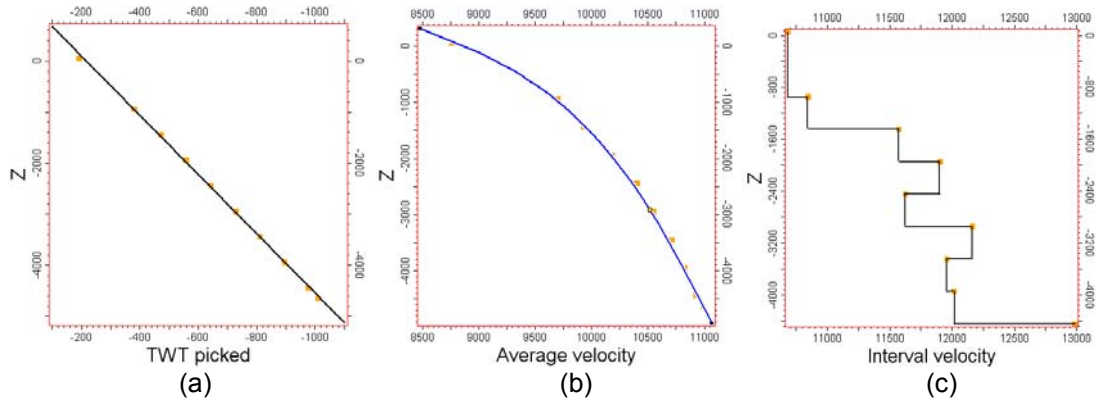


Figure 3.10 Velocity functions for the well B Yates 18D. (a) Time-depth graph, points in yellow represent the values from the check-shot survey, (b) average velocity versus depth values, and (c) interval velocity-depth graph.

Another useful information provided was the Vertical Seismic Profile (VSP) data on the same well location (B Yates 18D). VSP has several advantages over the surface seismic. It is usually free of multiples and does not contain formation

invasion and effects of very small-scale lithological changes. Therefore, good source to compare well synthetics and surface seismic since it contains very high signal to noise ratio (Bacon, 2003).

VSP for well B Yates 18D was loaded and used for correlating the surface seismic. Defining T-D relationship precisely is very important to able to convert time related information, mainly seismic, to depth and also placing the depth-indexed well log over the seismic and extract information. Different T-D relationship was established for the study area and used for velocity model building process.

Correction of sonic velocities (Figure 3.11) provides more reliable velocities as they carry high resolution information.

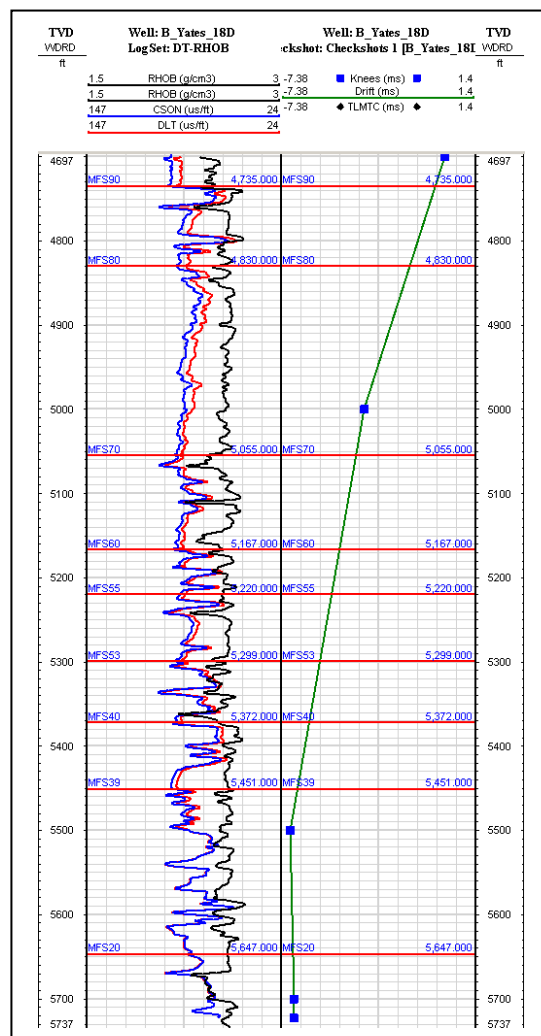


Figure 3.11 Sonic correction application for well B Yates 18D. Corrected sonic is in blue color in the left track.

Figure 3.11 shows original density (RHOB, black curve) and sonic (DLT, red curve) in the left track and CS points in the right track for the well B Yates 18D. By adjusting drift cure (green in color), DLT is corrected against CS values. Corrected DLT is blue curve in the left track. Sonic log contains some artifacts due to changes in borehole diameter, invasion of the borehole fluids, very high or low velocity layers etc.

First, only one well was used to populate velocity information to the area. To be able to achieve this, synthetic seismogram for this well was created (Figure 3.12). Synthetic seismograms are helpful mainly for tying the well information, mainly formation tops, to surface seismic and correcting the sonic logs using CS information.

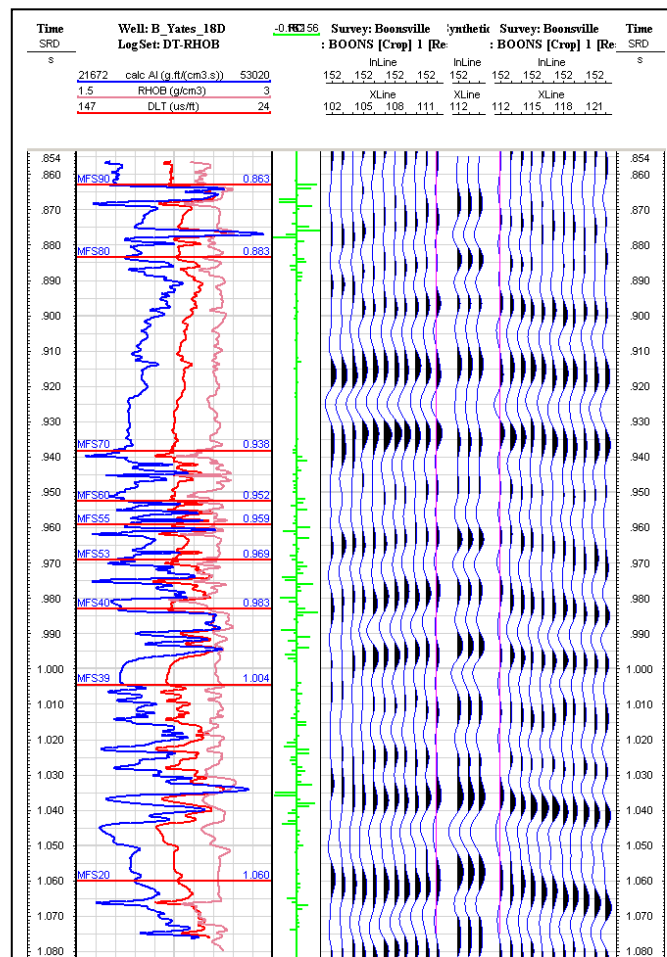


Figure 3.12 Well B Yates 18D synthetic seismogram. Acoustic Impedance curve (in blue) obtained from corrected sonic and density curves. Reflection coefficient series are shown in green. In the right track, corrected synthetic seismogram is shown in the middle (three traces) with surface seismic extracted around the well B Yates 18D.

Correcting sonic log was followed by the calculation of the synthetic seismogram for the same well. In Figure 3.12, Acoustic Impedance (AI) curve was obtained using corrected sonic curve and density curve. AI is simply obtained from velocity and density (blue curve). Using AI log, Reflection Coefficient (RC) series can be extracted (green curve).

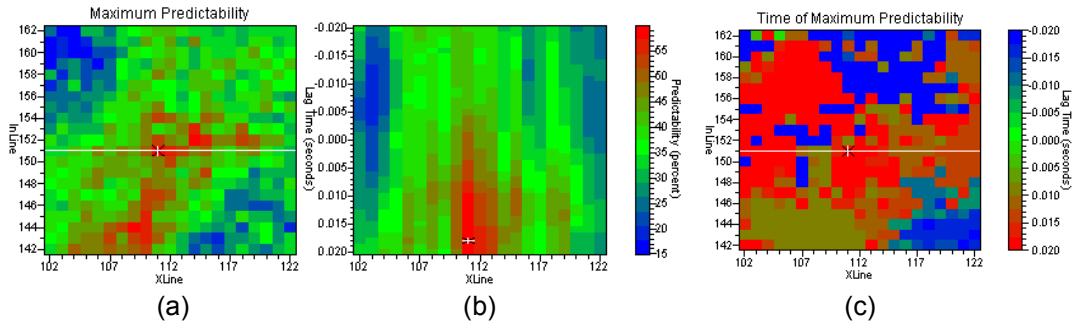


Figure 3.13 Wavelet extraction procedure for the B Yates 18D well. (a) Maximum predictability from 20x20 traces around the well B Yates 18D, (b) predictability in percentage with lag time and (c) time of maximum predictability with lag time in seconds. Cross sign over the white line shows the best location to extract wavelet.

Correcting sonic log was followed by the creation of the synthetic seismogram for the same well. In Figure 3.12, Acoustic Impedance (AI) curve was obtained using corrected sonic curve and density curve. AI is simply obtained from velocity and density (blue curve). Using AI log, Reflection Coefficient (RC) series can be extracted (green curve).

The final procedure of creating the synthetic seismogram is extracting the wavelet. To extract the best representative wavelet, 20x20 traces centered around the well were used to calculate maximum predictability with correlating seismic data with log derived reflectivity (Figure 3.13).

Figure 3.14 presents the final extracted wavelet used in synthetic seismogram creation in Figure 3.12. This procedure of obtaining the synthetic seismogram is simply represents the *forward solution*.

As it can be seen in Figure 3.12, a good match was obtained between the synthetic traces and the surface seismic which led to correcting the sonic velocities. This match was obtained mainly shifting and squeezing the synthetic seismogram reflections against the surface seismic reflections. Obtained corrected velocities at the end of this process can be used for the velocity model which will be constructed

but the reliability of the results can be questionable. Therefore, the practice performed above is repeated for two other wells, B Yates 11 and C Yates 9,

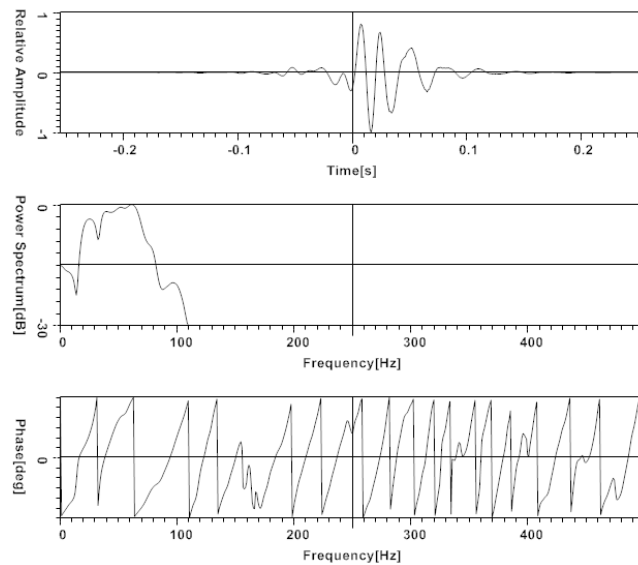


Figure 3.14 Extracted wavelet using the parameters in Figure 3.13. The first panel shows the relative amplitude of the zero-phase wavelet, the second panel is the power spectrum, and the third panel presents the phase. This wavelet was used to construct the synthetic seismogram for the well B Yates 18D.

having sonic and density logs to be able to calculate the synthetic seismogram and correct the sonic velocities. But because these two wells are located at the edges of the study area, they were not able to present the best velocity distribution in the area. As a result, another methodology was followed to build the velocity model which will be presented in the following sections.

3.4 SEISMIC INTERPRETATION

In the study area, nine main sequence boundaries were used and four of them interpreted along the 3D seismic data. To preserve the original amplitude values and not to cause the loss of information, seismic interpretation was made on 32-bit data.

Figure 3.15 and 3.16 presents the interpreted time structure maps of the Caddo (MFS90), David (MFS70), Runaway (MFS53), and Vineyard (MFS20) levels. For the scope of this study, the interval between Caddo and Vineyard has been chosen. Please note that the units are two-way travel time in the maps and the results are smoothed with certain length of filters.

As it can be seen clearly in Figure 3.15, both Caddo and David horizons deepens through the north direction. Analyzing the deeper partitions of the Vineyard

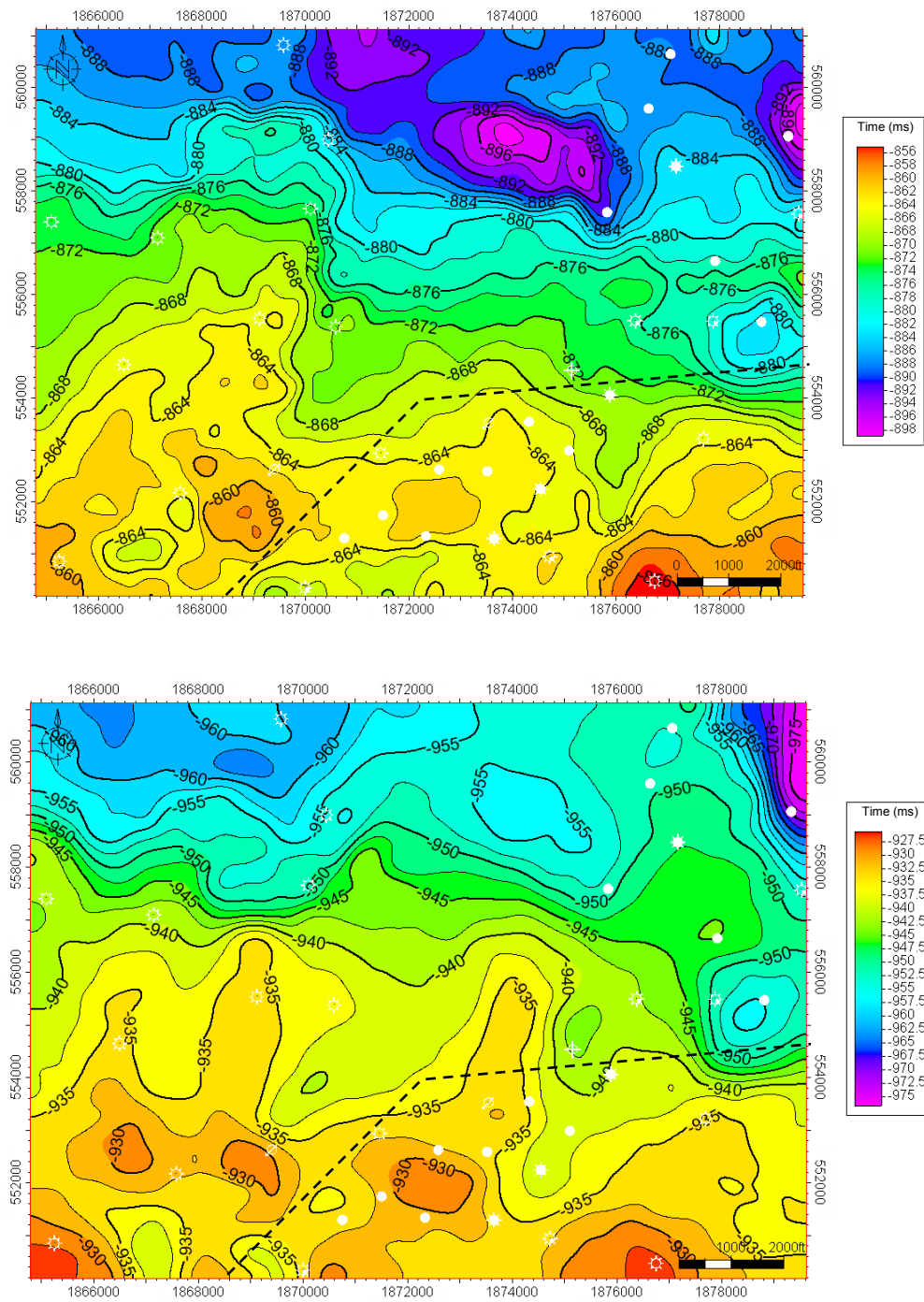


Figure 3.15 Two-way time structure map of the Caddo (MFS90) and David (MFS70) horizons respectively. Please note that, contour interval is 2 ms for Caddo and 2.5 ms for David levels, and blue color represents deepening. Circles in white color show well locations in the area. Dashed line illustrates the location of the composite seismic line (Figure 3.17).

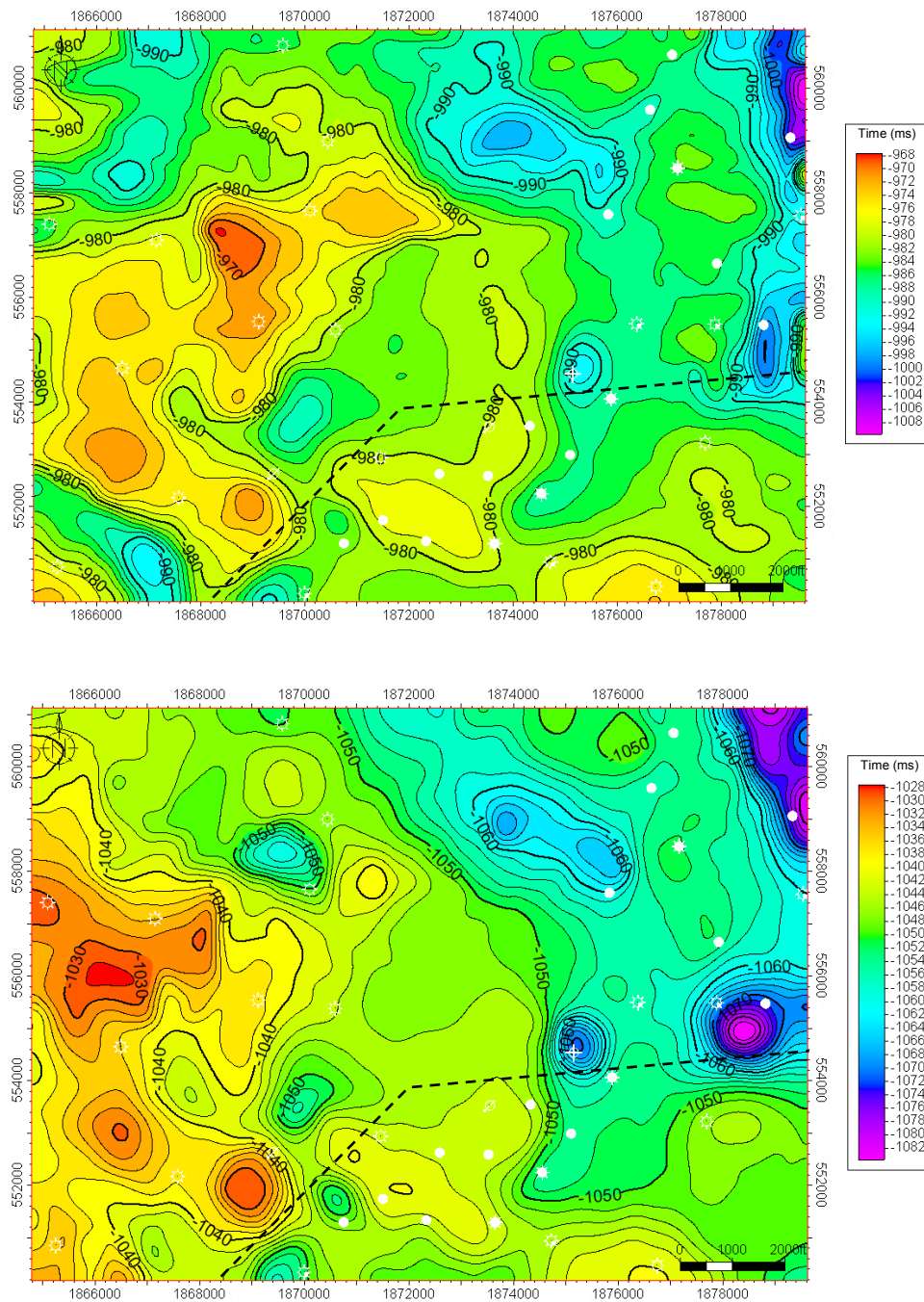


Figure 3.16 Two-way time structure map of the Runway (MFS53) and Vineyard (MFS20) horizons respectively. Please note that, contour interval is 2 ms for both levels, and blue color represents deepening. Circles in white color show well locations in the area. Dashed line illustrates the location of the composite seismic line (Figure 3.17).

structure map (Figure 3.16) exhibits some depression with a random pattern. These depressions having circular to oval shapes with changing areal extends and

collapse features appears along northwest-southeast trends and may indicate a relationship with the basement faults (Figure 3.17) (Hardage et al., 1996).

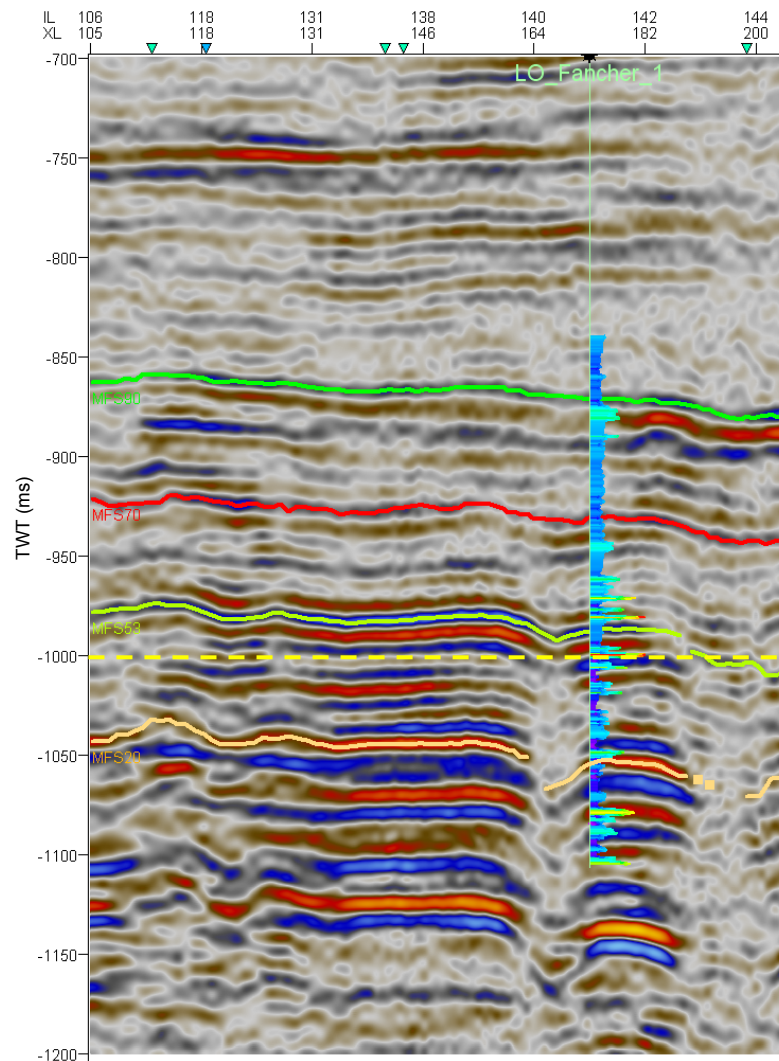


Figure 3.17 Seismic composite line over the study area. LO Fancher 1 well with its RILD log was posted on the line along with the four interpreted horizons. Collapse features can clearly be seen on the section near the well. Please refer to Figures 3.15 and 3.16 for the location of the seismic line. Dotted straight line shows the location of the time slice at Figure 3.18.

Hardage et al. (1996), stated that collapse type stratigraphic disruptions occurs within the Pennsylvanian section, some of these Ordovician-related structural sags were a significant influence on Pennsylvanian and Mississippian sedimentation. These zones of collapses are believed to be caused by post-Ellenburger carbonate solution weathering, which occurred during periods of subaerial exposure.

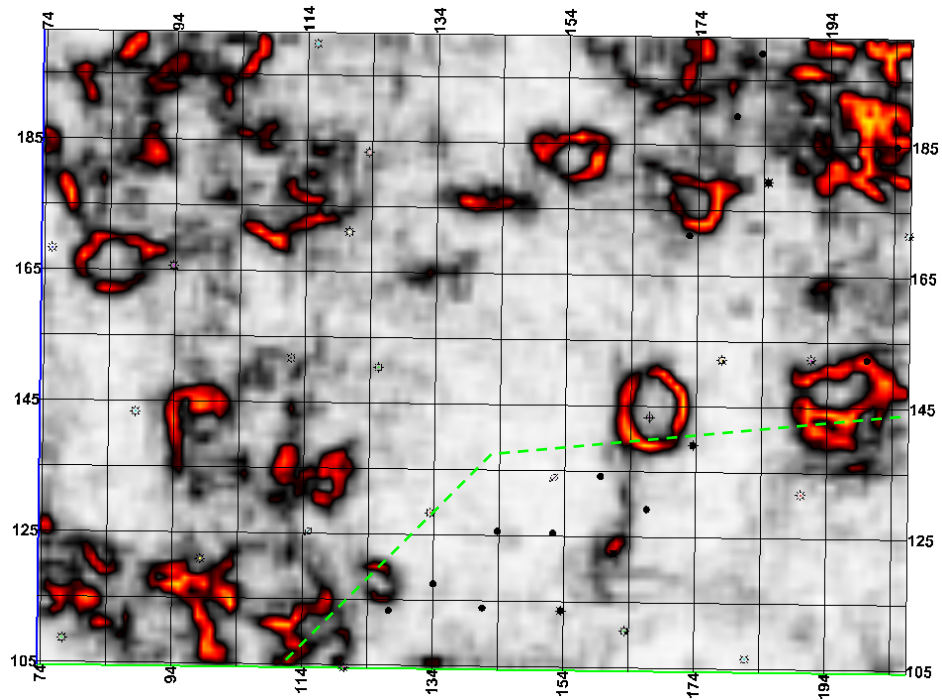


Figure 3.18 Variance time slice at 1,093 ms from the seismic survey. Dotted green line shows the location of the composite section in Figure 3.12. Circular depression can be seen clearly through the time slice. Location of the time slice can be followed on the seismic section in Figure 3.17.

3.5 VELOCITY MODEL AND DEPTH CONVERSION

Successful depth conversion is crucial for placing the reflectors from time domain to depth domain. The best way to achieve this is use of check-shot (CS) information in the boreholes. Check-shots usually provide very precise time-depth information and velocities derived from them are trustable. On the other hand, because their sampling interval is sparse, 10 to 20, velocities obtained are representing coarse information. Conversely, sonic velocities provide very high resolution information but they suffer from providing precise velocity values due to several reasons discussed before.

In this part the velocity model will be built using the check-shots from three wells as a guide. Interpreted time values at the horizon well intersections and depth values of the formation tops at the same locations will be used to create T-D pairs for the wells where no time-depth information is available. Figure 3.19 shows the corrected sonic logs using the CS information from the well B Yates 18D.

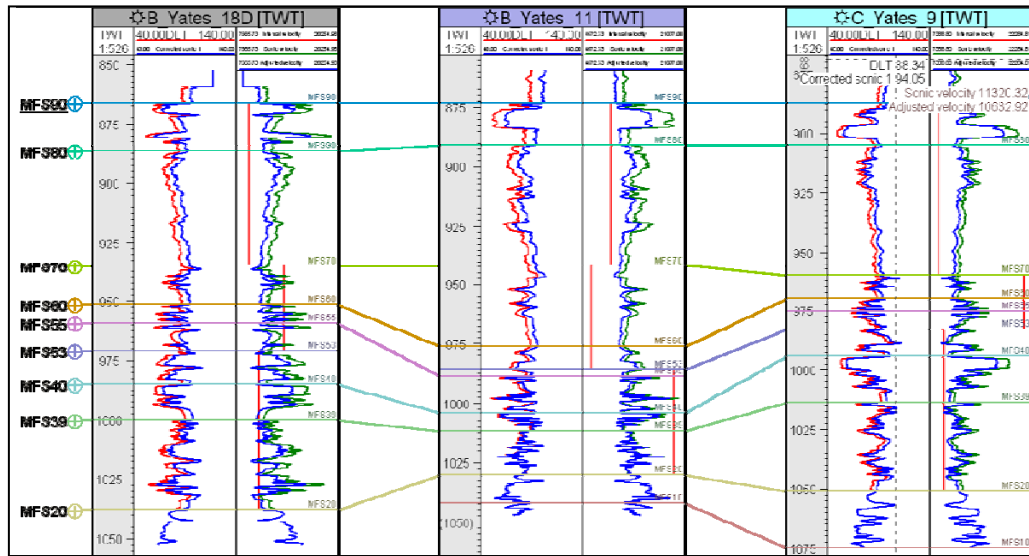


Figure 3.19 Corrected sonic curves for the wells B Yates 18D, B Yates 11, and C Yates 9. In the first tracks, red and blue curves show original and corrected sonic curves; in the second tracks red line shows interval velocities, green and blue curves show sonic and corrected velocities.

Formation top times which they were created from the derived and adjusted CS pairs, checked for errors against time interpretation at well locations. Most of the depth conversion issues arise from poor matching of well tops to seismic horizons. Therefore, the time values of the formation tops that is created by T-D relationship from the wells need to be checked for errors before velocity modeling.

In Figure 3.20, time interpretation of the Caddo (MFS 90) horizon gridded again by tying the MFS 90 top times. The map shows, contours of the Caddo horizon and deviation from the formation times presented in colors (red to blue). This information is useful primarily for showing the bad well top times that needs to be edited before velocity modeling. It can be clearly seen that residuals appear at the well locations in the map. This is mainly due to difference in times between wells and mapped horizons. Residual maps were prepared for other three horizons also to check the consistency between time values.

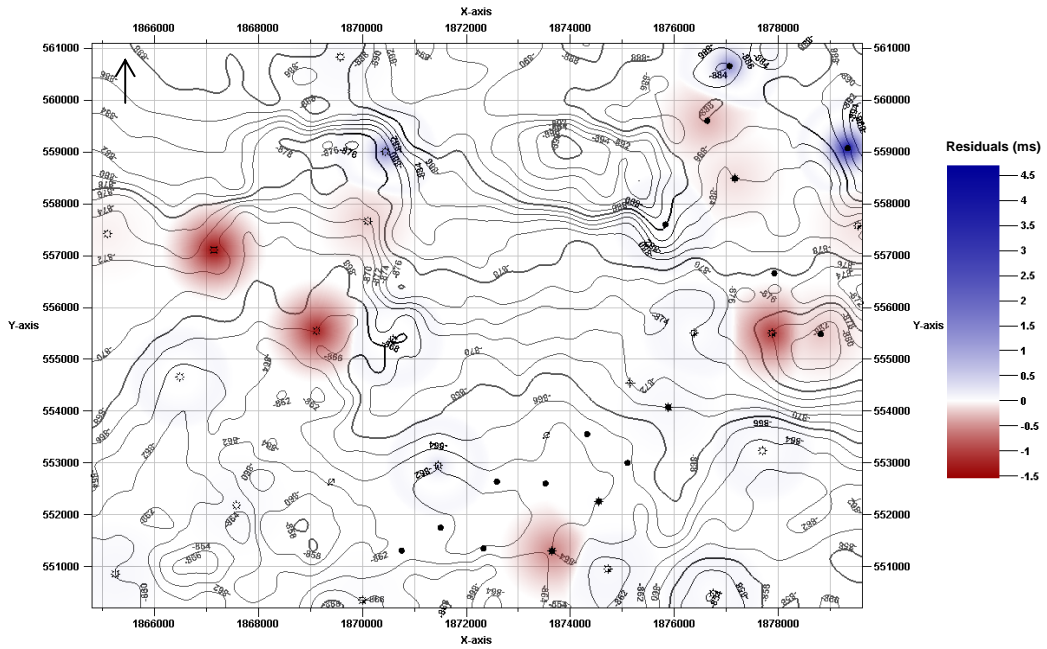


Figure 3.20 Two way time map (ms) of the Caddo horizon overlain by residual values. Positive residuals are in blue and negative residuals are in red color.

Figure 3.21 shows time errors for four horizons. The errors are, for the Caddo horizon; -1.55-4.71 ms, for David; -1.77-1.88 ms, for Runaway; -1.63-4.15 ms, and for Vineyard; -3.26-3.08 ms.

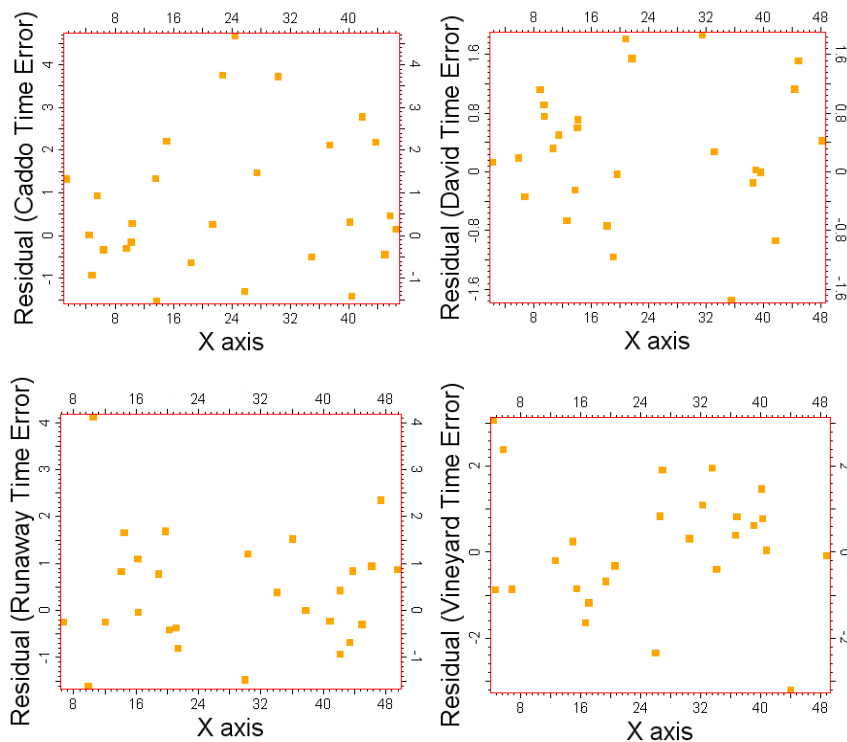


Figure 3.21 Time error plots for the horizons Caddo, David, Runaway, and Vineyard.

Errors obtained from the well top time are relatively low in value, ranges between -1.77 to 4.71 ms. This shows that the errors can be ignored for the velocity model building but it can be suggested that further investigation of these error can exhibit some more information about the study area. For instance, creating variogram of the errors can indicate a direction dependent nature and may be linked to a geological phenomenon, e.g., certain facies type, or petrophysical character.

Velocity model for the area was built using all wells inside the study area. Among them, B Yates 18D has CS and DT logs, B Yates and C Yates 9 have only DT logs. T-D information from these log were populated the other wells using the relationship between interpreted horizon's times and formation top's depths.

Before building the model, the most commonly used seismic velocities will be discussed briefly (Dix, 1955):

- Average Velocity: defines the velocity of the reflection below a reference surface $V_{ave} = z / t$, where; z is the layer thickness and the t is the one-way travel time (OWT). It should be used in geologically simple cases.
- Interval Velocity: gives the velocity between two reflection levels. It does not account for the changes of velocity with depth. They can be used in simple geological situations and when well velocities or dense stacking velocities are available. $V_{int} = (z_{i+1} - z_i) / (t_{i+1} - t_i)$, where; z is depth and t is OWT.
- Instantaneous Velocity: If the velocities continuously change with depth, V_{ins} can be expressed as, dz/dt , where; dt is the derivative of the infinitive thickness of the layer approached to depth z , t is the OWT.
- Linear Velocity: Assumes velocity changes with depth proportional to a constant k , $v = v_0 + k*z$, where; v_0 is the datum velocity, k is the rate of change with depth, and z is the depth of the layer. Modified version of this type is the changing velocity in each layer: $v = v_0 + k*(z - z_0)$, where; in each layer, the velocity is changes at the rate of k .

In this study, $v = v_0 + k*(z - z_0)$ velocity model will be used. Because this model not only consider the velocity at each layer top but also velocity changes inside the same layer. v_0 was derived from the velocities at the horizon well intersections and gridded along the area and k constant was determined automatically from the well T-D relationships. Figure 3.22 shows the instantaneous velocity cube created which is consistent with the well velocities and T-D relationship built from well tops. As it can be noticed, velocities increase with depth following the rules of the velocity model mentioned above.

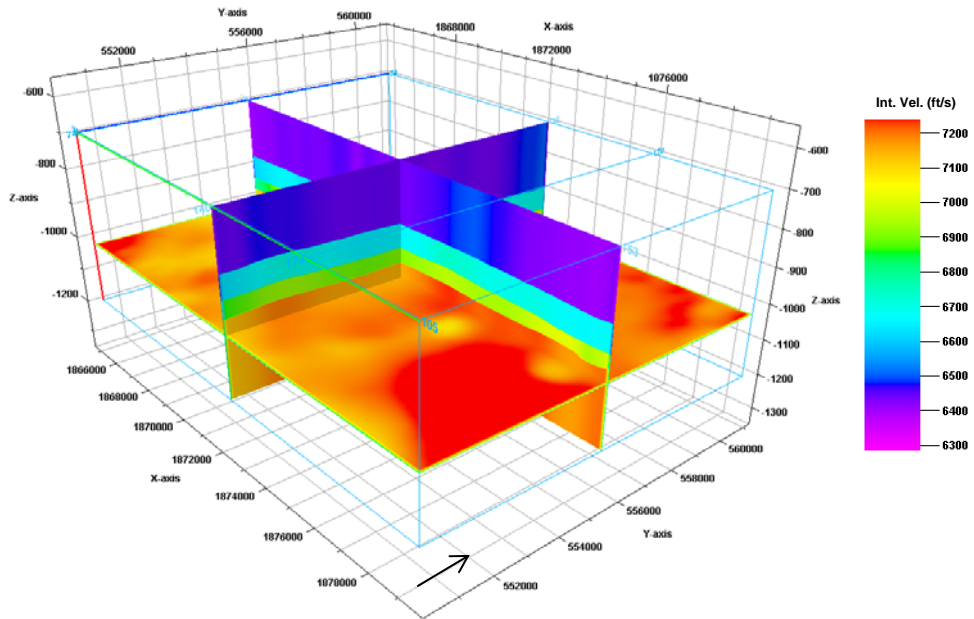


Figure 3.22 3D velocity model built for the whole area. Color scale shows the interval velocity values in ft/s.

Figure 3.23 shows seismic amplitude section (in-line 153) is overlain by interval velocity attribute. Well B Yates 18D with a sonic log and formation tops were also posted on the seismic section.

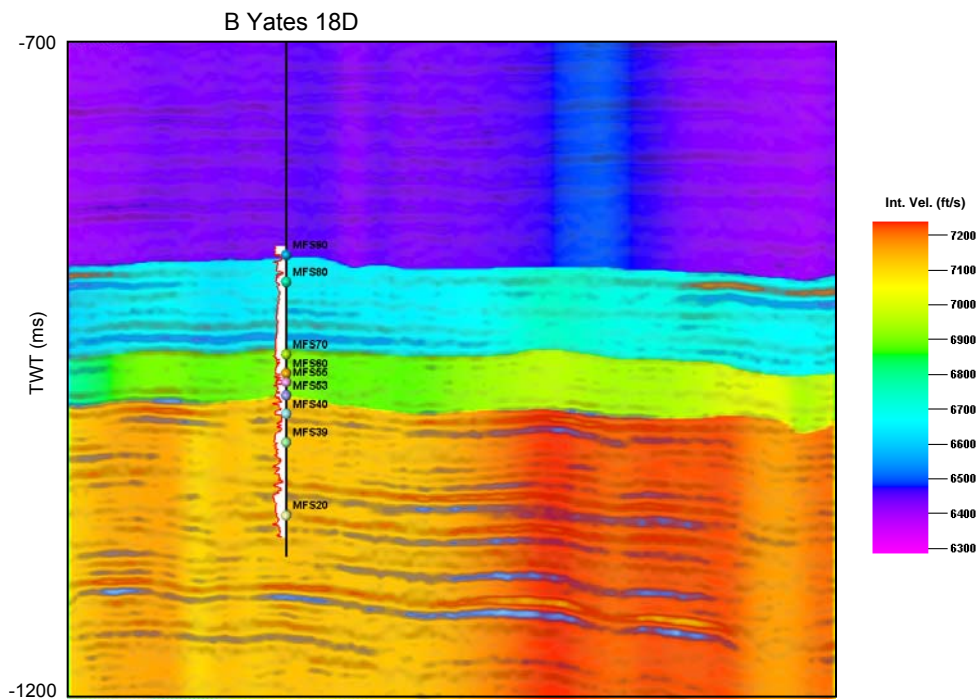


Figure 3.23 Interval velocity field was posted on seismic in-line 153. Displayed wellbore is B Yates 18D with its sonic log and formation tops. Note that vertical axis is in time (ms).

As it can be noted from the Figure 3.23, interval velocities vary in both vertical and lateral directions presenting the local changes in the seismic data. Because velocity boundaries defined from datum to four interpreted horizons, there is clear velocity boundaries appear in the section. This 3D velocity field was smoothed and used for depth converting the 3D seismic data and interpreted surfaces.

Figure 3.24 shows comparison of time and depth converted seismic sections. Section on the left hand side is the time version and the right hand side section is the depth converted seismic data. The sampling interval of the time seismic is 1 ms and the depth seismic has 3.5 ft sampling interval.

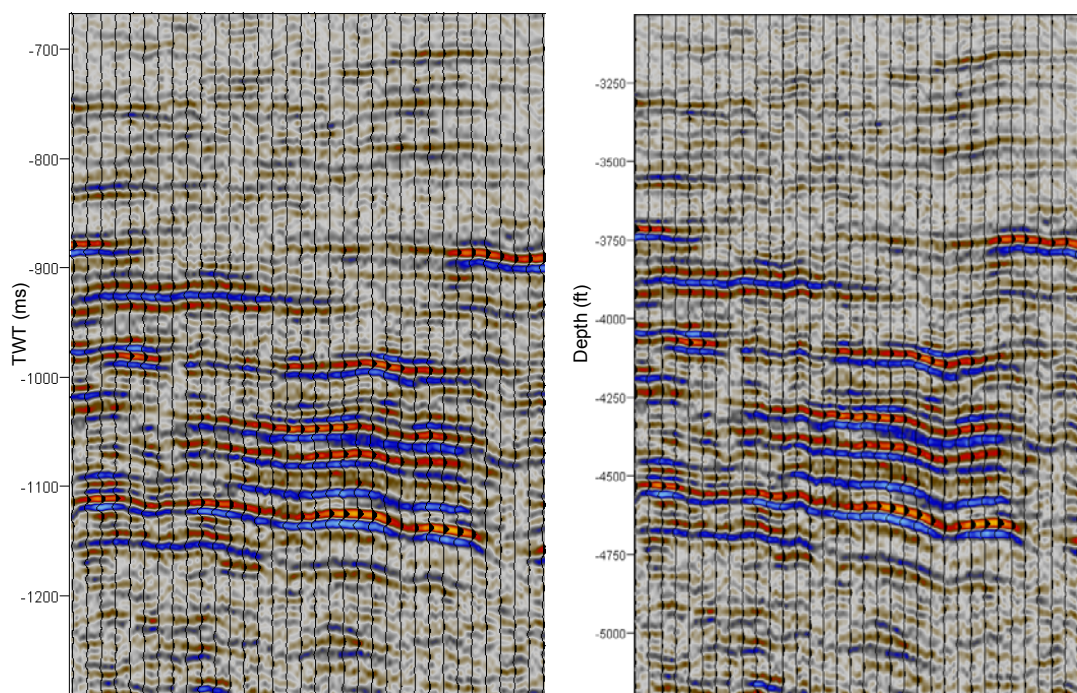


Figure 3.24 Seismic in-line 153 showing time and depth converted versions. Velocity field created in previous section is used for conversion. Note that, vertical axis is in ms and ft for the time and depth sections respectively.

After having velocity model for the area, it is now possible to convert each item separately to depth, or construct the structural model of the area and convert whole model from time to depth. Second option will be considered in this study. Because all the data inside the model were placed on each grid node inside the 3D grid, converting whole model in time to depth using the 3D velocity field provides consistency.

3.6 STATIC MODEL BUILDING

For reservoir characterization studies, one of the main steps is constructing the static model. To achieve this, first, new grid spacing was applied to area to be modeled. The grid spacing was chosen as 50x50 ft laterally. Figure 3.25 shows the initial model having three zones between the four formation tops. This model represents the time domain as the input horizons come from seismic time interpretation.

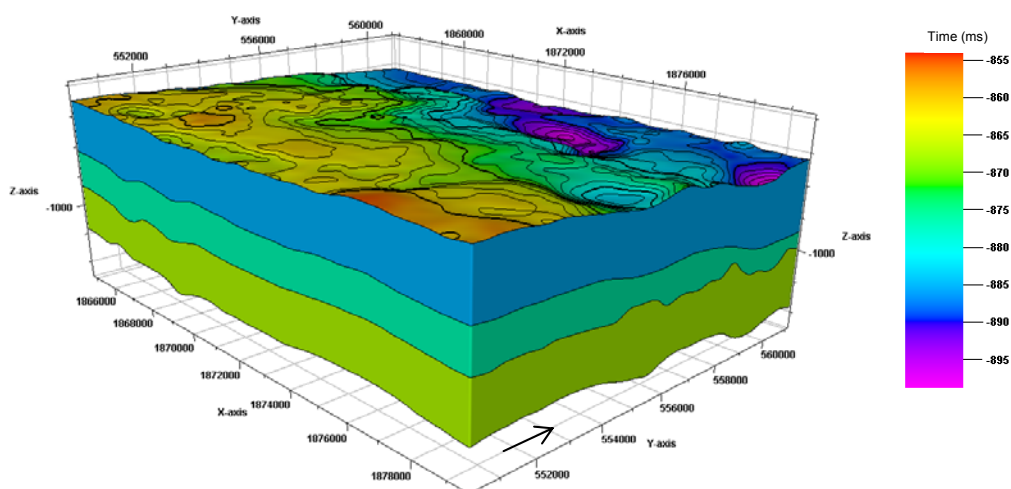


Figure 3.25 Initial structural model for the area. Four interpreted horizon were used to build the structural model. Three zones can be seen in different colors and the domain is in time (ms).

After completing the initial model, the layers were subdivided into stratigraphic intervals. The complete list of formation tops can be seen in Figure 3.7. Figure 3.26 shows the updated zoned in the study area. To build this model, first time maps of the each formation tops were prepared then the thicknesses were calculated for each zone. Then, each thickness was summed up starting from base to top. During this operation, the sum normally does not match the top horizon. Therefore, a proportional volume correction was applied to thicknesses. The error is distributed proportionally into each zone depending to their thickness and the last zone thickness at the top matched the upper most horizon. Finally the whole model is converted to depth using the smoothed velocity model prepared in the previous section.

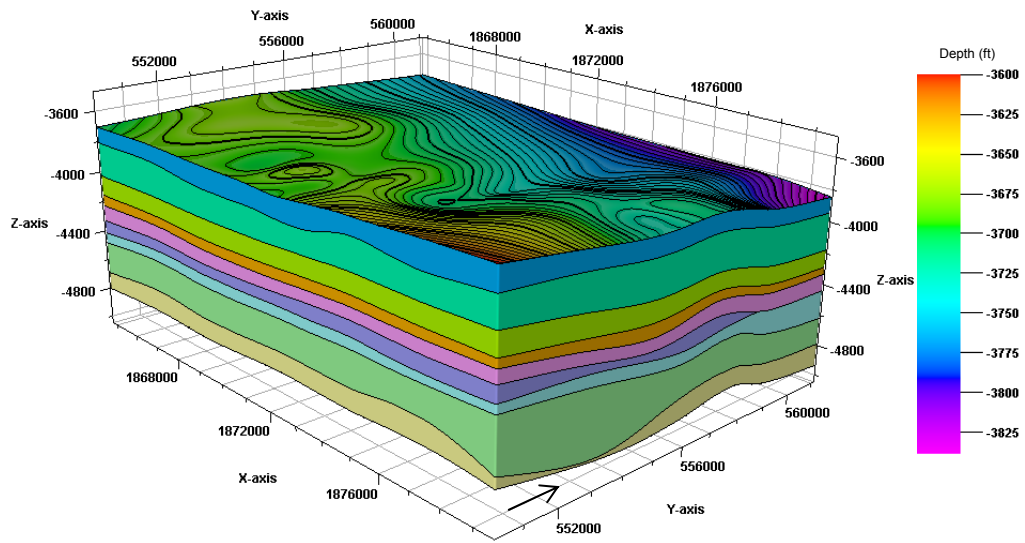


Figure 3.26 Structural model for the are which was divided into stratigraphic intervals. Each colored zone represent different stratigraphic interval. The top horizon is the Caddo (MFS 90).

The last step in static model building is defining the fine layering of each zone. This operation is necessary to be able to resample the properties into the model. The most important parameter for this operation is deciding the layer thickness which will be the guide for the well log upscaling in the next chapters. For the purpose of this study, each zone is divided into 2 ft intervals which are believed to be good representative of the properties. Figure 3.27 shows the layering results for one of the zones.

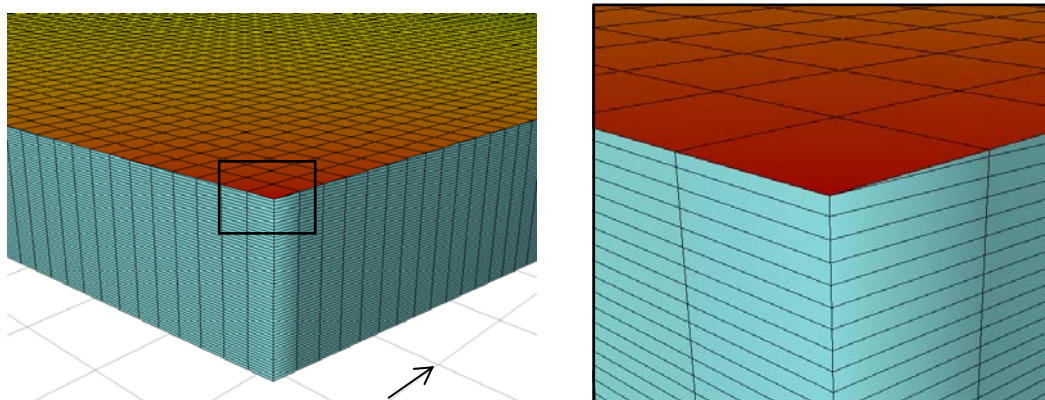


Figure 3.27 Layering results for the zone 7 (light blue color zone in Figure 3.26). Each layer represents 2 ft thickness in vertical direction and the grid on the horizon level shows 50x50 ft X-Y spacing.

CHAPTER 4

ESTIMATION OF MISSING LOG SETS

As it can be inferred from the previous chapters, the study area contains 38 wells with various logs but full suite of well logs is available for only few wells. Because the aim of this study to predict the reservoir properties, porosity, saturation, net thickness etc., there is a need for complete set of logs due to two main reasons. The first one is seismic inversion study will require the Acoustic Impedance (AI) at well locations to be able to create reasonable outcomes. The second reason is ANN study needs some group of logs to be trained and verified. Therefore, the same type of logs should exist in all well locations.

There are several approaches to predict missing logs. Among them, empirical relationships (e.g. Gardner's approximation) and regression techniques are commonly used ones. In this chapter, estimation techniques will be applied to data and results will be compared to ANN estimation outcomes.

4.1 EMPRICAL METHODS

First, a sonic log will be estimated using Faust relationship. Faust (1953) developed the following empirical relationship to estimate sonic logs from resistivity logs:

$$\text{Sonic Velocity} = C_1 * (R*Z)^{1/6} \quad (4.1)$$

where; C_1 is a constant term (~2000), R is the resistivity, and Z is the corresponding depth. This relationship was applied to few wells having sonic log and results were compared. Figure 4.1 and 4.2 show sonic log estimation results for wells Ashe C5, B Yates 11, B Yates 18D, and C Yates 9. Since the relationship is linear, predicted sonic curves appear as mirror images of the resistivity curves having different values. In order to check the consistency of the method, cross plots were created between estimated and original sonic values and correlation coefficient was obtained. Figures 4.3 and 4.4 present these plots. For the first two wells correlation coefficients (CC) are 0.80 and 0.91 respectively and for the other two wells CCs are 0.85. Correlation between original and estimated log looks very reasonable but due to fact that it is built on a linear relationship, results should be used with care as the reservoir properties usually exhibits a non-linear relationships in the subsurface.

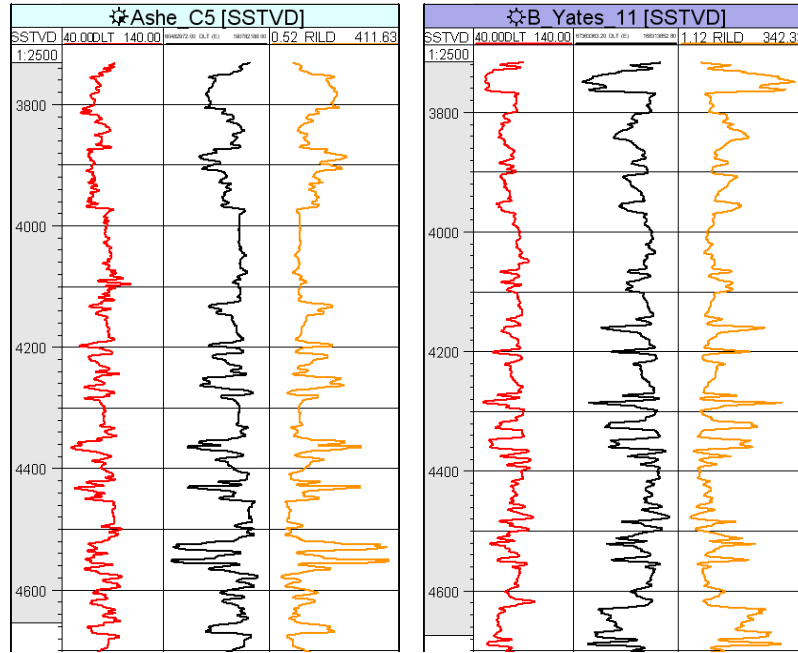


Figure 4.1 Sonic estimation results using Faust's relationship for wells Ashe C5 and B Yates 11. Red curve is original DT, black curve shows estimated DT, and yellow curve is RILD.

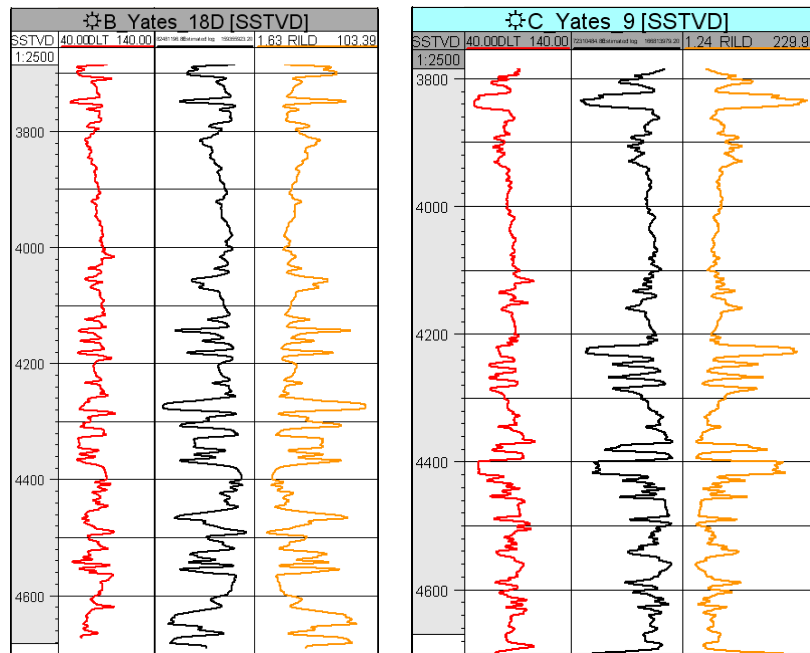


Figure 4.2 Sonic estimation results using Faust's relationship for wells B Yates 18D and C Yates 9. Red curve is original DT, black curve shows estimated DT, and yellow curve is RILD.

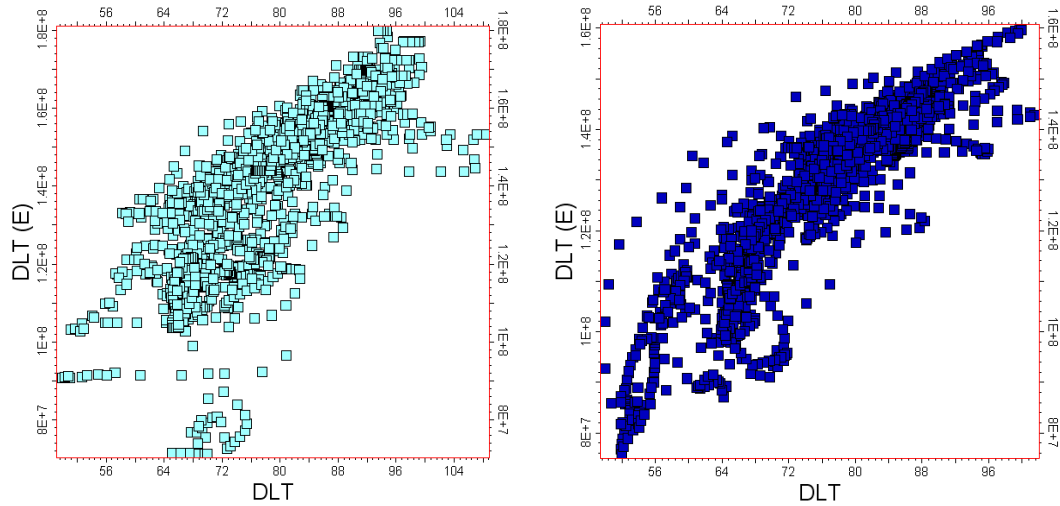


Figure 4.3 Sonic versus sonic estimated (DLT-E) cross plots for Well Ashe C5 and B Yates 11 respectively. Correlation coefficient (CC) is 0.80 for the first plot and for the second plot CC is 0.91.

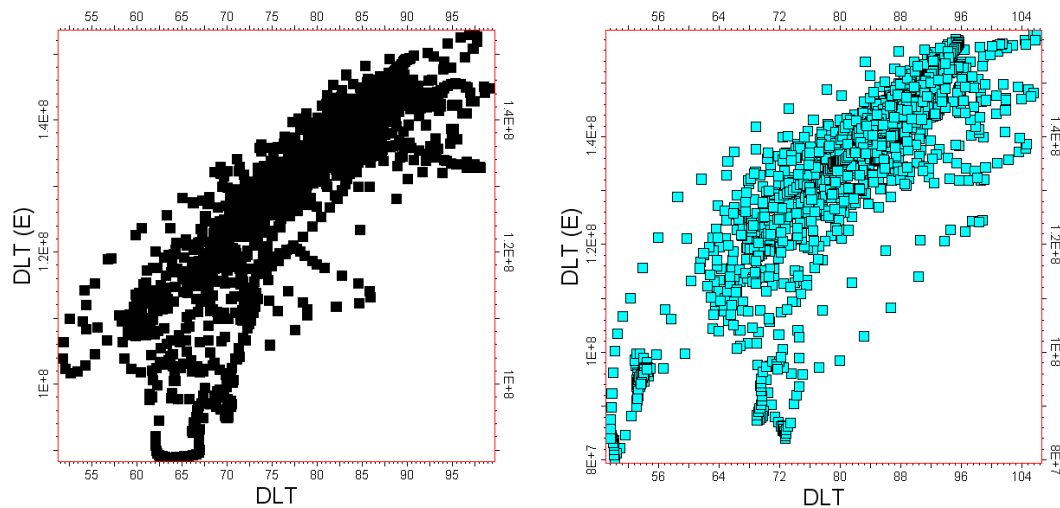


Figure 4.4 Sonic versus sonic estimated (DLT-E) cross plots for Well B Yates 18D and C Yates 9 respectively. Correlation coefficient (CC) is 0.85 for the first and second plots.

Another empirical relationship is established by Gardner (1974). In this relationship, approximation to density using sonic is given by:

$$\text{Density} = C_2 * DT^{(1/e)} \quad (4.2)$$

where; C_2 is a constant depending on the rock type, DT is sonic log, and e is the exponent (Table 4.1). Figure 4.5 and 4.6 show the result of density approximation using Gardner's relationship.

Table 4.1 Gardner's velocity-density relationship constants for the different lithologies (modified from Mavko et. al., 1998).

Lithology	C_2	e	Vp range (km/s)
Shale	1.75	0.265	1.5-5.0
Sandstone	1.66	0.261	1.5-6.0
Limestone	1.50	0.225	3.5-6.4
Dolomite	1.74	1.252	4.5-7.1
Anhydrite	2.19	0.252	4.6-7.4

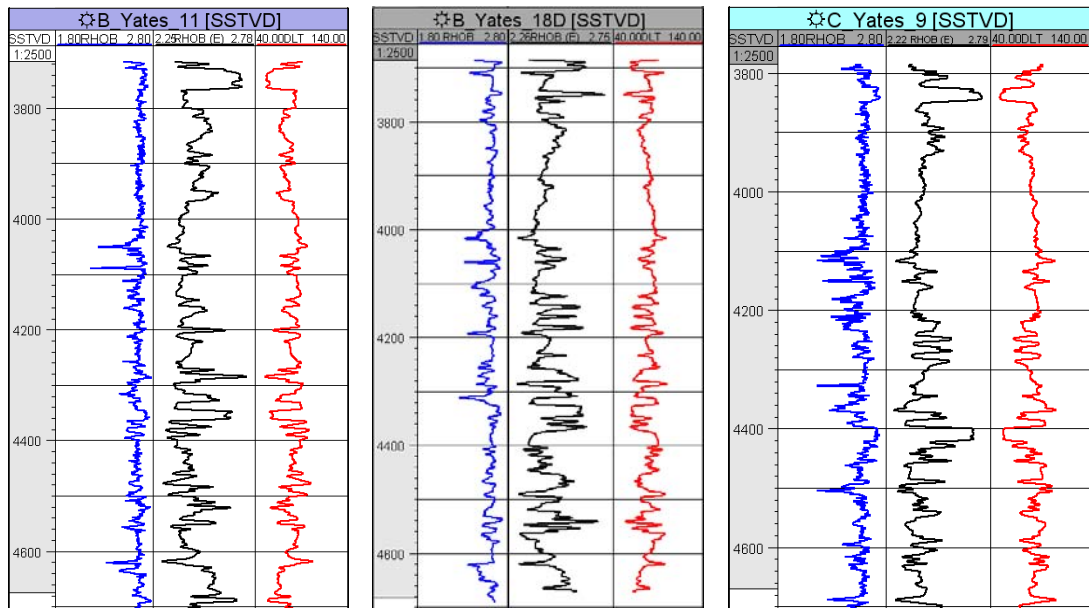


Figure 4.5 Density estimation results using Gardner's relationship for wells B Yates 11, B Yates 18D, and C Yates 9. Blue curve is original RHOB, black curve is estimated RHOB and red curve is original sonic.

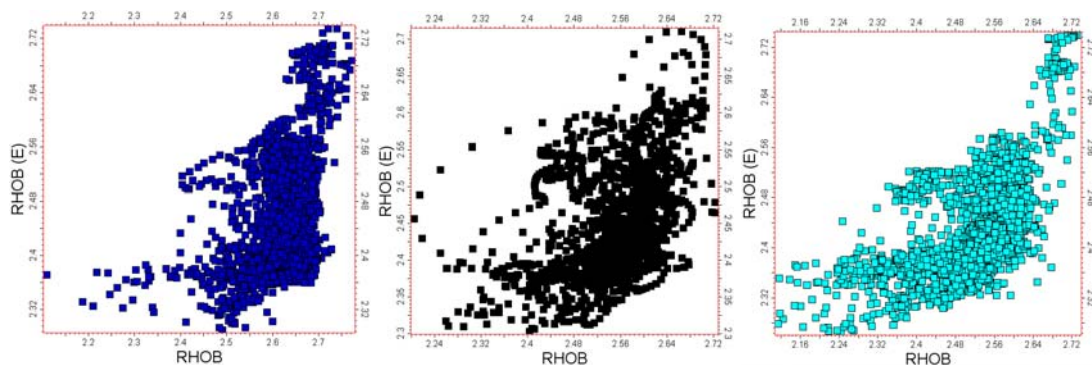


Figure 4.6 Density versus density estimated (RHOB-E) cross plots for Well B Yates 11, B Yates 18D, and C Yates 9 respectively. Correlation coefficients (CC) are 0.44, 0.39, and 0.60 respectively.

As it can be inferred from above figures, estimated density curves again similar to sonic curves as the approximation equation states. CCs are relatively low and these results indicate that using empirical relationships does not generally produce reliable results to be able to populate reservoir properties to whole field, Therefore, in the next section; a neural network approach will be used for prediction purposes.

4.2 NEURAL NETWORK APPROACH

As it can be concluded from the previous section, using empirical relationships to estimate well logs, in general, does not provide the best solution approach. Therefore, ANN techniques will be used to predict missing log sets in the study area. ANNs provide a very effective solution for prediction studies with its flexibility to find out non-linear relationships from the existing data and applying it to estimate missing logs. In this part of the study, two different well logs estimation were performed, sonic (DT) and neutron-porosity (NPHI). DT estimation was conducted using a single layer network and the results were satisfying. For NPHI estimation, a similar method was used together with the Principal Component Analysis and Correlation Analysis. It has been observed that improved results were obtained.

Well logs are one of the most commonly used data type in hydrocarbon exploration, production and development studies. They contain valuable detailed information about subsurface but usually they are too expensive to acquire and sparse. On the other hand, the computing techniques bring efficient and low-cost solutions to estimation of missing data. Once the relationship has been derived between different log types, missing or target log types can be derived.

The process presented involves usage of artificial neural networks to estimate well logs. First, the most correlated logs were selected and then based on this selection, two different set of logs were used for DT and NPHI estimation; NPHI-RHOB-RILD and GR-RILD-DT respectively.

The objective of this part is to apply neural networks to predict missing log sets in the area. The reason of choosing neural networks for this prediction study is its ability to establish non-linear relationship between training data and populating this relationship to boreholes having missing log types. The most important artifact of the technique is the overtraining issue which can be overcome using parameter change and result validation.

There are three main steps to be followed. The first step involves the editing, loading and quality checking of the well log data. The second step is selecting the most correlated logs versus other log(s) to be estimated. The last step consists of applying the neural network technique to data set for prediction (Arzuman, 2009).

The main aspects of the ANN are their ability to estimate or classify the data sets which can be performed in two ways for the training data: supervised or unsupervised. In this study, the supervised training will be used.

A single hidden layer has been used in this work. In Figure 4.7, there are three layers: In the input layer, the nodes (circles) are connected with weights (w), in the hidden layer; the nodes carry a nonlinear activation function.

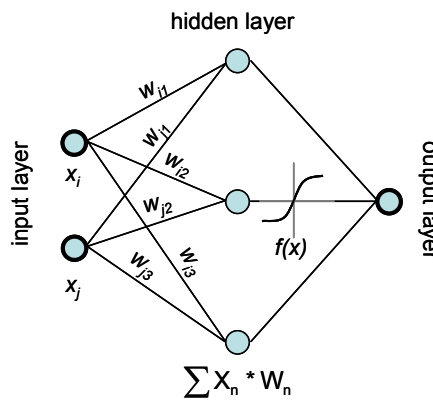


Figure 4.7 A multilayer neural network structure with a single hidden layer. Input layer, hidden layer and output layer have 2, 3 and 1 neurons respectively. Weights (w) are computed, summed and distributed to the output layer with a non-linear activation function, $f(x)$ (modified from Schraudolph and Cummins, 2009).

The resistivity log basically measures the formation's resistivity. The resistivity logs can be used to determine hydrocarbons presence, lithology, fluid saturations, and compaction, overpressure and shale porosity (Rider, 1986). The gamma ray log measures the radioactivity of the uranium, thorium and potassium of the formation is generally used to determine the shale volume (Rider, 1986). The sonic log determines the formation's interval transit time and changes with lithology and rock texture (Boyer and Mari, 1997). It is mainly used to determine porosity in liquid-filled holes. The neutron log detects the hydrogen presence and neutron-derived porosity can be measured for certain type of minerals as they exhibit known responses (Ransom, 1995). The density log measures the overall density (solid matrix and fluid in pores) of the formation. It is basically used to determine the

porosity and can be useful for lithology, overpressure and fracture identification (Rider, 1986). As it can be seen, there are clear relationships between DT, RILD, GR, NPHI, and RHOB logs.

Wireline logs sonic travel time (DT) was estimated based on Deep-Induction Resistivity (RILD) and Compensated Neutron Porosity (NPHI) was predicted based on Gamma Ray (GR), DT and RILD. Prior to selection of the input logs to be used for prediction, logs were normalized and checked for consistency in log cross-plots. For the first estimation part, DT log was cross plotted versus NPHI, RHOB, RILD, and RHOB was plotted versus NPHI, RILD, and GR (Figure 4.8) for well B Yates 18D. It was observed that the most correlated log types with the DT were NPHI, RHOB, and RILD. Therefore, ANN was initially run using these log types.

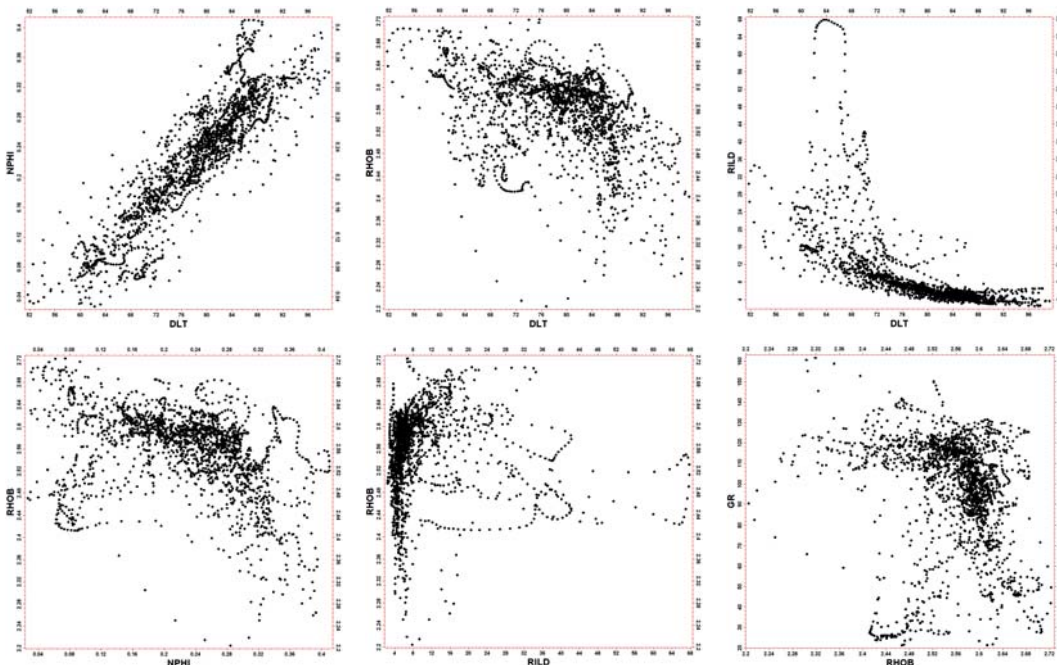


Figure 4.8 Log data cross plots for the well B Yates 18D. Cross plots from left top to right bottom: NPHI versus DT with CC: 0.89, RHOB versus DT with CC: -0.40, RILD versus DT with CC: -0.65, RHOB versus NPHI with CC: -0.36, RHOB versus RILD with CC: 0.07, and GR versus RHOB with CC: -0.07.

Error measurement is one of the most important criteria for measuring the artificial neural network prediction results. Akin et. al. (2008) defines two types of error description: “mean squared error (MSE) which is the squared difference between the actual output and the predicted output and the absolute relative error

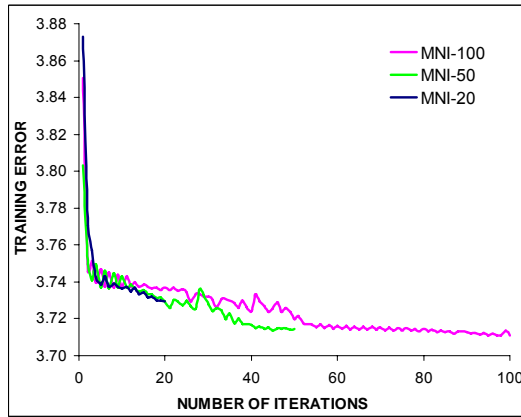
(ARE) which is the absolute value of the actual output minus predicted output divided by the actual output”.

In this study, three following types of error estimation will be used to decide for the best network parameters for prediction. Training error (TE) is the root-mean-square (RMS) error between the training data and the estimated values. Checking error (CE) is the error between the modeled values and the estimated values to validate the model. Relative error (RE) is the ratio between the initial checking error when the model is created and the current checking error. RE is the RMS error normalized by the standard deviation of the training data and therefore ranges from 0 to 1 (Schlumberger, 2009).

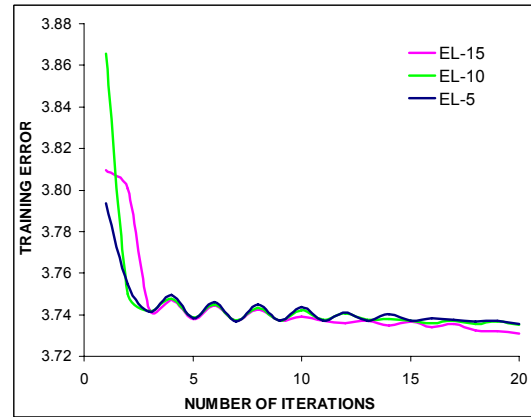
Two main considerations were pointed out by Akin et. al., (2008) for estimation procedure using artificial neural networks: memorizing and over saturation. If the training allowed going too far where the TE is notably smaller than the CE, the network is over trained. In this point, the algorithm cannot distinguish data characteristics any more. This problem can be overcome by dividing the data set into two parts (cross validation, CV): one part is used for training to optimize the weights and the other part is used to measure the error levels on the training.

Train and estimation models created by neural networks are iterative processes. The results are checked at the end of each iteration and new iteration begins depending on the error criteria. Better results can be obtained with more iterations but deciding the number of iterations (convergence criteria) is an important step for obtaining better estimation results. Maximum number of iterations (MNI) can be increased if the error limit (EL) is decreasing even if the iteration maxima is reached. If the model converges quickly and reaches the error limit as the RE is still diminishing, the EL can be decreased to improve the estimation results. If the EL is kept constant and MNI is reached, the estimation process produces the best results but they might not be the best outcomes for the particular EL. Increasing the EL and decreasing the MNI stop the estimation process earlier. If the results are not good as expected, the input data might need to be rechecked and the network parameters could be changed.

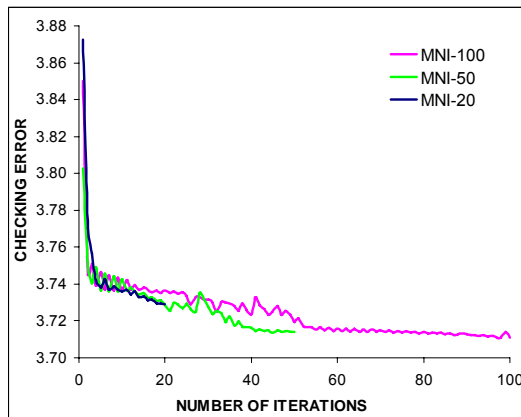
After quality checking and editing of the well logs, the most correlated logs were selected based on their correlation strength. Parameter selection for the ANN algorithm was done based on the following three factors: MNI, EL, and CV. Figure 4.9 shows the optimum parameter selection tests for the network algorithm used to estimate missing well logs.



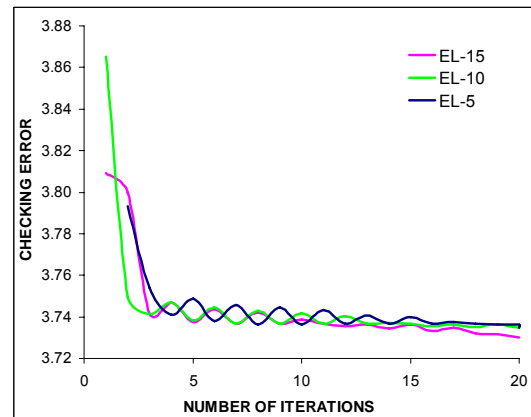
(a-1)



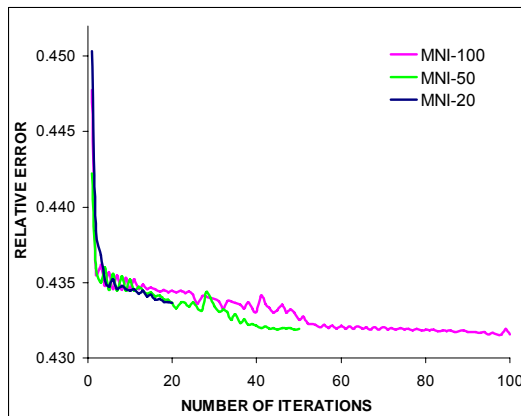
(b-1)



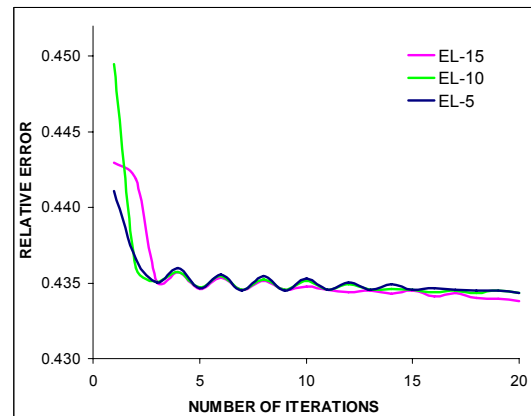
(a-2)



(b-2)

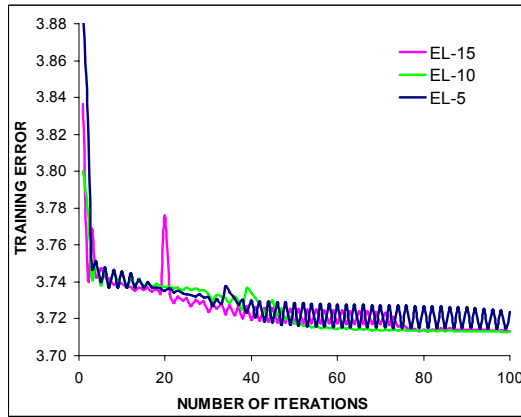


(a-3)

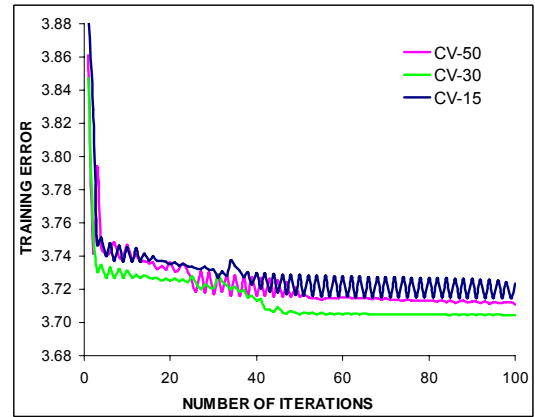


(b-3)

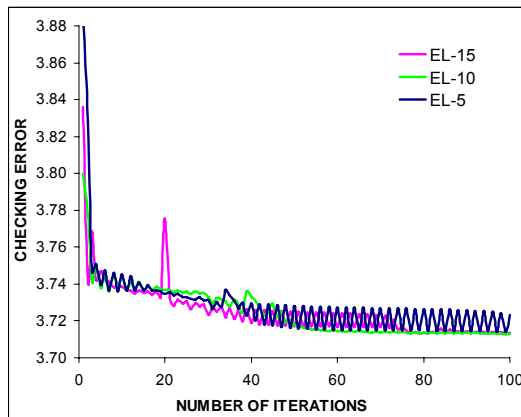
Figure 4.9 ANN optimum parameters (MNI, EL and CV) selection error plots. In plots (a), EL:10 and CV:50 are constant and MNI is 20, 50, and 100 for each error plot. In plots (b), MNI: 20 and CV:50 are constant and EL is 5, 10, and 15 for each error plot.



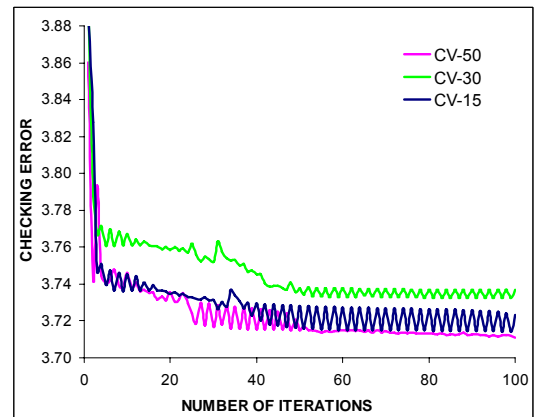
(c-1)



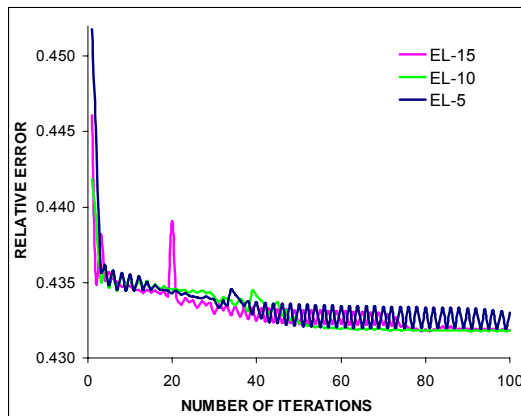
(d-1)



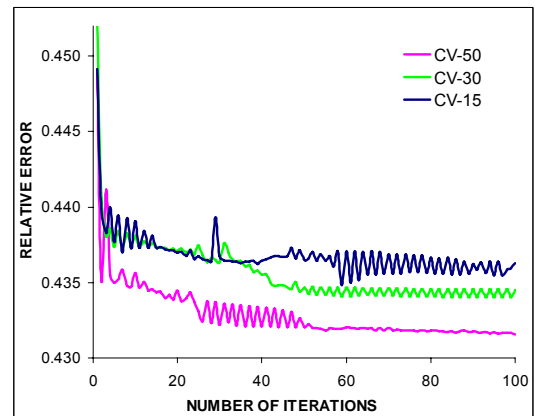
(c-2)



(d-2)



(c-3)



(d-3)

Figure 4.9 (continued) In plots (c), MNI:100 and CV:50 are constant and EL is 5, 10, and 15 for each plot. In plots (d), MNI:100 and EL:10 are constant and CV is 15, 30, and 50 for each plots.

In Figure 4.9 (a), EL and CV were kept constants as 10 and 50 respectively and effect of MNI on training, checking and relative errors were observed. The effect of changing the MNI produced similar responses for all error types. MNI: 20 showed

dramatic decrease in all errors until 5th iteration and the errors started to decline slowly. Using 50 MNI produced similar response except perturbations between the 5th and 13th iterations. The errors started to decrease gradually afterwards. Using 100 MNI created higher errors until 50th iteration and the errors reached the steady state condition thereafter. In Figure 4.9 (b), MNI was selected as 20 and CV is decided to be 50 as constant and EL is by a factor of 5. As it can be seen clearly, perturbations occurred until the 20th iteration to adjust the weights and errors reached the almost constant level. In Figure 4.9 (c), MNI: 100 and CV: 50 set as constants and EL levels 5, 10 and 15 were tested to check the network performance. In general, all errors produced similar responses. Selecting EL as a %5 showed decrease in error level until 30th iteration and high perturbations were observed afterwards. EL 10% gave smooth reduction in all error types until 50th iteration and then produced stable error level. Choosing EL as 15% exhibited strange behavior at the 20th iteration with a very high peak and then produced high perturbations between the 35th and 75th iterations. In Figure 4.9 (d), effect of the CV was tested. Three cases were selected: 15% CV used 1737 points for training and 307 points for cross validation. 30% CV used 1431 points for training and 613 points for cross validation. 50% CV used 1022 points for training and cross validation. 15% CV created high perturbations after the 40th iteration for TE and CE and did not show steady error level afterwards. On the other hand, it exhibited an unsteady error levels for the RE. 30% CV was increased the error levels in general and reached the sill condition after the 40th iteration. Using 50% CV produced similar responses in all error types. The errors decreased until the 26th iteration, created perturbations between the 26th and 50th iterations and started to become constant.

Analysis of the error characteristics was suggested that the optimum parameters for the ANN algorithm were MNI: 50, EL: 10% and CV: 50%. Table 4.2 shows the sample calculated error estimations for the ANN algorithm. Following parameters were used: Max number of iterations: 20, Error limit: 10% and Cross validation: 50%. Each time the relative error reaches for all time low, the results are saved and the comment “store” appears in the table.

The results of the training with optimum parameters can be seen in Figure 4.10. These results showed that the most correlated log for estimation of DT log was NPHI but because it was sparse in the study area, RILD was used to estimate DT for the rest of the field.

Table 4.2 Petrel ANN run DT estimation error results for the well B Yates 18D.

Training neural network			
Number of points for training = 2047 ==> 2044 = 1022 + 1022			
Epoch	Training error	Checking error	Relative error
1	3.86729	3.86691	0.44968 ... store
2	3.76958	3.76913	0.43831 ... store
3	3.74158	3.74109	0.43505 ... store
4	3.74948	3.74903	0.43597
5	3.73836	3.73785	0.43467 ... store
6	3.74632	3.74586	0.43560
7	3.73681	3.73627	0.43449 ... store
8	3.74520	3.74473	0.43547
9	3.73696	3.73642	0.43451
10	3.74410	3.74363	0.43534
11	3.73716	3.73662	0.43453
12	3.74127	3.74078	0.43501
13	3.73720	3.73666	0.43453
14	3.74015	3.73966	0.43488
15	3.73725	3.73671	0.43454
16	3.73741	3.73689	0.43456
17	3.73729	3.73675	0.43454
18	3.73585	3.73530	0.43438 ... store
19	3.73679	3.73624	0.43449
20	3.73531	3.73474	0.43431 ... store

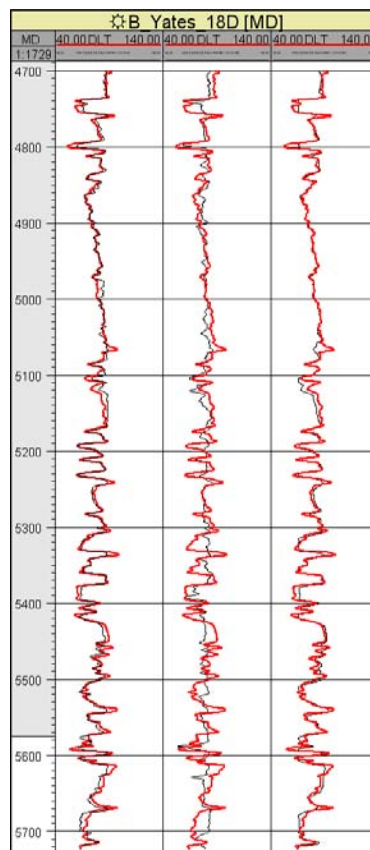


Figure 4.10 DT estimation results from ANN versus original DT logs. Well B Yates 18D estimated DT logs (in black) are displayed along with the original DT logs (in red). The first track is NPHI, the second is RHOB, and the third track is RILD results respectively.

To obtain the CCs of this training phase, cross plots were also prepared (Figure 4.11). From these cross plots, the most correlated log found as NPHI with a 0.90 correlation coefficient but because there are only few wells having complete NPHI log, RILD was used to train and estimate DT. During the training phase, the

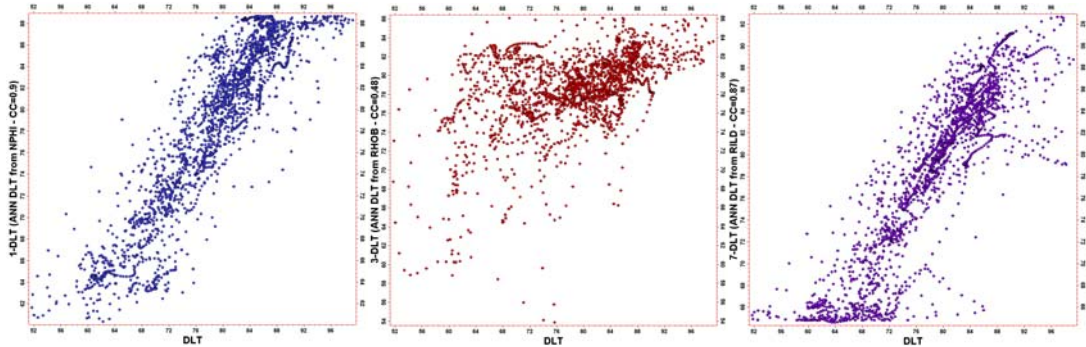


Figure 4.11 Estimated versus original DT log cross plots. Cross plots show trained DT log versus original DT logs obtained from NPHI, RHOB, and RILD. CCs are 0.90, 0.48, and 0.89 respectively.

Training part of the study was repeated using three other wells in the study area due to fact that single well cannot be use to populate the relationship obtained to whole area.

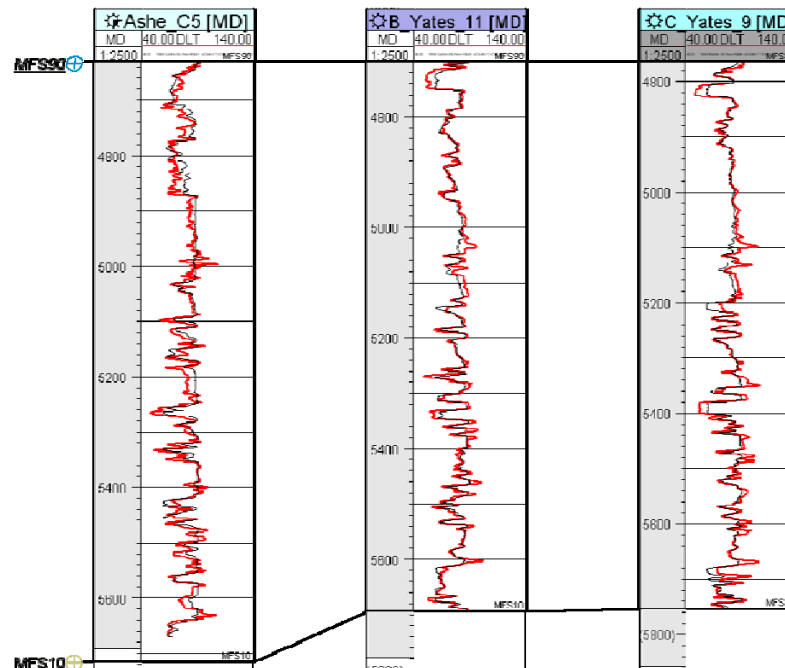


Figure 4.12 DT estimation results from RILD logs. Red color curve represents the original DT and black curve show estimated DT logs.

Previously used well B Yates 18D was not included into this training to compare the results from the single well estimation outcome. This comparison basically shows the effect of incorporating wells from different parts of the study area to prediction study. Training and estimation results can be seen in Figure 4.12.

To obtain the CCs of this training phase, the cross plots were also prepared (Figure 4.13). From these cross plots, the most correlated well found as B Yates 11 with a 0.91 correlation coefficient.

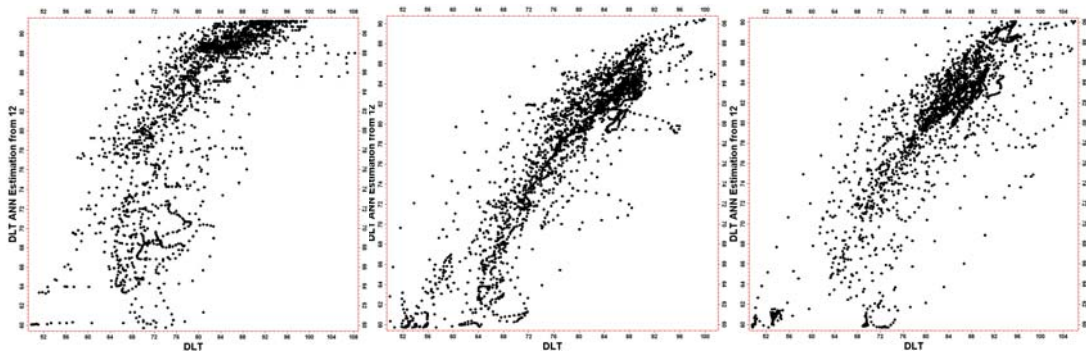


Figure 4.13 Cross plots of the estimated DT log versus original DT logs. Results obtained from wells Ashe C5, B Yates 11, and C Yates9. CCs are 0.79, 0.91, and 0.85 respectively.

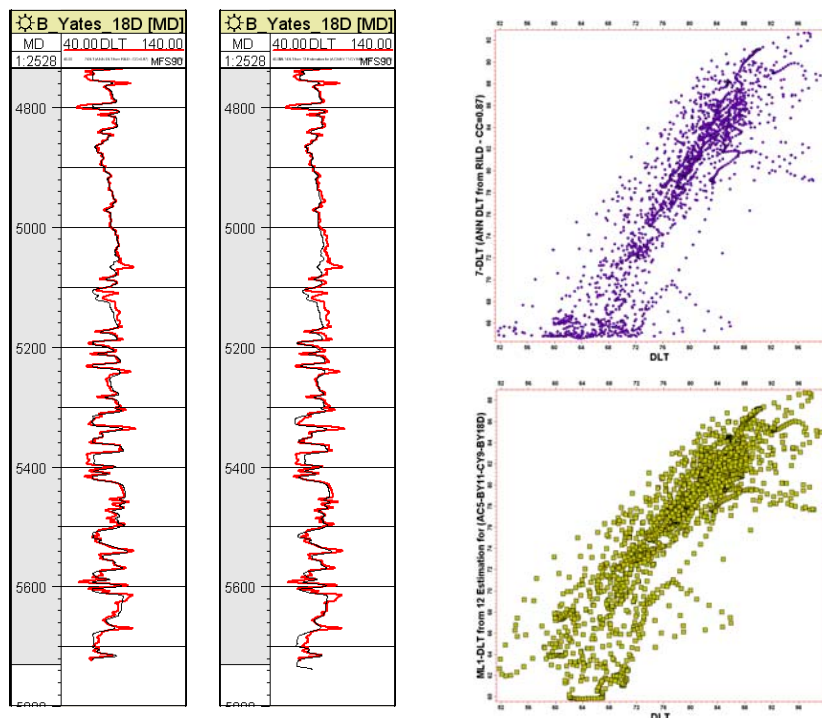


Figure 4.14 DT estimation results for well B Yates 18D using RILD from one and three other wells. The first track shows DT estimation (black curve) using RILD from B Yates 18 D well and the second track presents the results using wells Ashe C5, B Yates 11, and C Yates9. CCs are 0.89 and 0.87 respectively.

Training results were also applied to B Yates 18D well to be able check to stability of the network. Figure 4.14 shows the results of this analysis.

As it can be noticed, CCs of second training is lower than that of the first one but because it has a better areal representation of the area, estimating the DT log using the first training set was not suggested. Wells chosen for the training phase should have a better representation of the area.

Similar study is executed for the NPHI estimation. Figure 4.15 shows cross-plot of original NPHI log versus other logs for Well B Yates 18D to determine which log to be used for training the ANN.

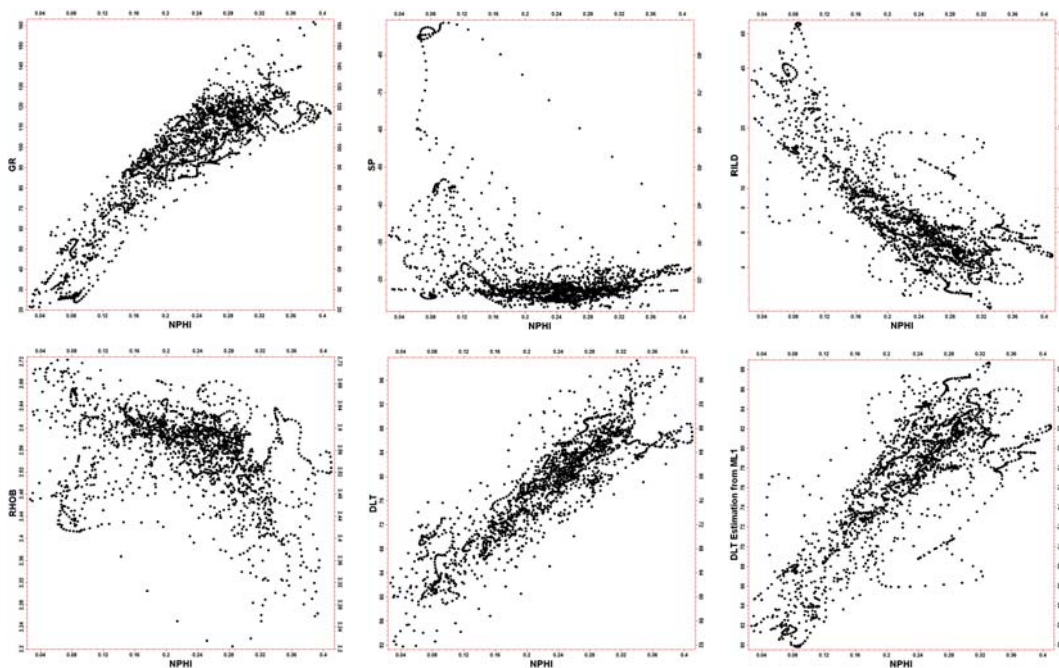


Figure 4.15 NPHI versus GR, SP, RILD, RHOB, DT and estimated DT cross plots. CCs are 0.891, 0.419, -0.792, -0.363, 0.890 and 0.804 respectively (Well B Yates 18D).

It is obvious that the GR is the most correlated log with NPHI and it was used to train the network. Training parameters were kept the same and the Figure 4.16 shows the results of the trained network for five wells, Ashe C6, B Yates 13, -15, -18D, and IG Yates 9 in the study area. CC of the training was found as 0.84 using the GR log. In general, NPHI estimations were produced meaningful result for all wells even though B Yates 15 and -18D correlations were not perfect. Correlation coefficient was 0.84. Individual cross plots for each well can be found in Figure 4.17.

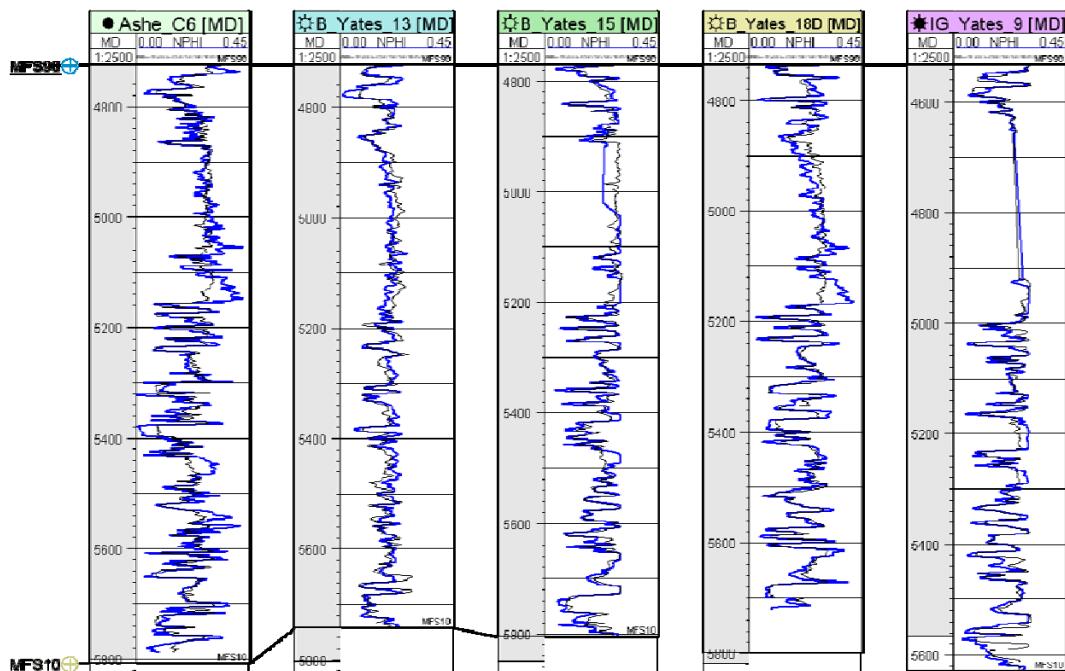


Figure 4.16 NPHI estimation results for 5 wells (Ashe C6, B Yates 13, -15, -18D, and IG Yates 9). Original log is blue in color and CCs are 0.847, 0.763, 0.822, 0.893 and 0.864 respectively.

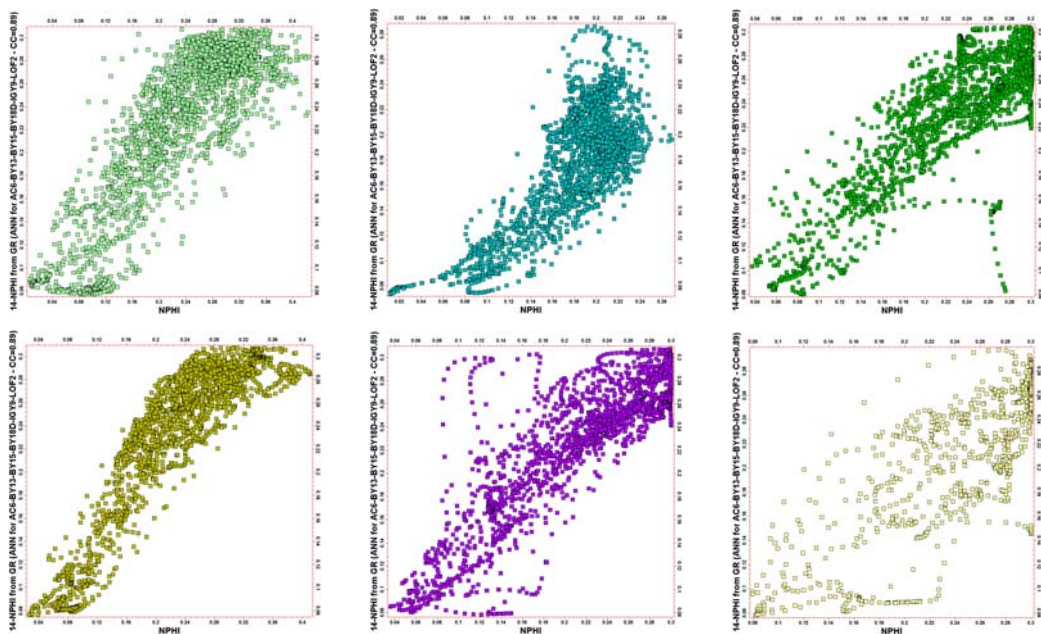
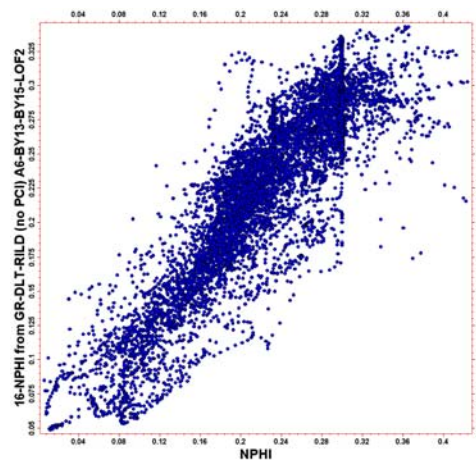


Figure 4.17 NPHI versus estimated NPHI cross plots for wells Ashe C6, B Yates 13, -15, -18D, and IG Yates 9. Corresponding CCs are 0.847, 0.763, 0.822, 0.893 and 0.864 respectively.

Beside Correlation Analysis (CA) which we performed using cross-plots, Principal Component Analysis (PCA) another very useful technique to help ANN process was used. PCA simplifies a dataset by reducing multidimensional datasets to lower dimension for analysis. The main use of PCA is to reduce the dimensionality of a data set while retaining as much information as is possible. PCA is a linear transformation that transforms the data to a new coordinate system. The new few coordinates contain the most important aspect of the data.

Figure 4.18 below represents the training results for NPHI estimation for wells Ashe 6, B Yates 13, B Yates 15, and LOF 2 using GR, RILD and DT logs at the same time. PCA was not used in this training process.



	RILD	GR	ML2-DLT from 12	NPHI
RILD	1.0000	0.6602	0.9894	0.751118
GR	0.6602	1.0000	0.6511	0.8201
ML2-DLT from 12 for all	0.9894	0.6511	1.0000	0.7577
Total	0.9896	0.6604	0.9894	0.8731

Figure 4.18 Cross-plot of the training results for the NPHI estimation from GR, RILD and estimated DT using wells Ashe 6, B Yates 13, B Yates 15, and LOF 2 (CC=0.884845). Table shows the correlation coefficient for the logs against each other.

NPHI estimation was also performed using PCA analysis. Table 4.3 shows PCA for NPHI estimation. Eigenvalues present the relative importance of the Principal Components (PCs). The sum of these values equals the number of PCs. This is equal to “3” in our example and PC1 has the biggest variation with 84.86% contribution in the data set and the PC3 has the lowest one. It should also be noted that PC may show a very low eigenvalue but can show a good correlation. Therefore, it always a good practice to check the correlation table using CA (linear or non-linear).

Table 4.3 PCA results for NPHI estimation using RILD, GR, estimated DT for wells Ashe 6, B Yates 13, B Yates 15, and LOF 2.

Correlation Coefficients	PC1	PC2	PC3
RILD	0.9689	0.2363	0.0729
GR	-0.8208	0.5712	0.0012
ML2-DLT from 12 for all wells	-0.9660	-0.2484	0.0721
Eigenvalue	2.5457	0.4438	0.0105
Contribution (%)	84.86	14.79	0.35
Cumulative Contribution (%)	84.86	99.65	100.00

	PC1	PC2	PC3	NPHI
PC1	1.0000	0.0000	0.0000	0.8378
PC2	0.0000	1.0000	0.0000	0.2316
PC3	0.0000	0.0000	1.0000	0.0816
Total	0.0000	0.0000	0.0000	0.8731

Based on the result of PCA, PC3 was not included the training process as it has the lowest contribution. Figure 4.19 represents the results of the training. As it can be noticed from the both training results, reducing the least contributed data and dimension from the data set improves the results: CC (no PCA)= 0.884845 and CC (with PC1 and PC2)= 0.885236.

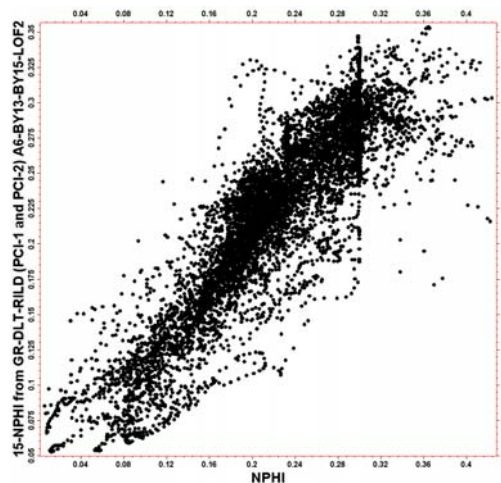


Figure 4.19 Cross-plot of the training results for the NPHI estimation using PC1 and PC2. GR, RILD and estimated DT were used from wells Ashe 6, B Yates 13, B Yates 15, and LOF 2 (CC=0.885236).

To represent the contribution of using the more than one type of log and PCA into estimation results, three different run were performed for the same four wells. The first estimation has been done using only GR log with no PCA, the

second estimation with GR, DT, RILD and the third one was done using GR, DT and RILD with reducing PC3 (Figure 4.20).

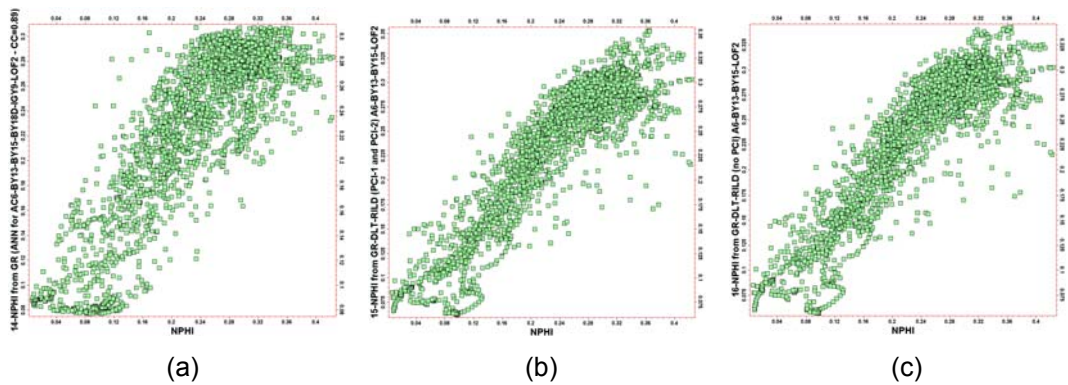


Figure 4.20 Cross-plot of the training results for the NPHI estimation versus original NPHI logs with and without PCs. NPHI estimation (a) using GR (CC=0.846961), (b) with GR, DT and RILD – no PCA (CC=0.898196) and (c) from PCA 1 and PCA 2 using GR, DT and RILD (CC=0.898351).

Figure 4.21 shows the result of above three trainings for NPHI estimation for well Ashe C6 corresponding to cross-plots a, b and c in Figure 4.20.

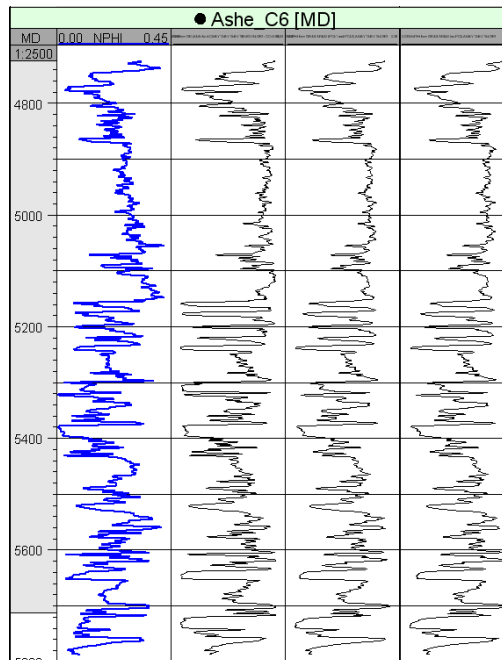


Figure 4.21 Estimated NPHI log for the well Ashe C6. Dark blue curve in the first track is the original NPHI log and the curves in tracks a, b and c represents the estimated NPHI logs with GR, GR-DT-RILD-no PCA and GR-DT-RILD-PC1-PC2 respectively.

In this section, DT and NPHI logs were estimated using ANN technique. Optimal network parameters were selected by analyzing error response of the different cases. Among them the best parameters were found as; 50 MNI, 10% EL and 50% CV. It was observed that increasing the number of iterations started to converge the estimation results after certain number. Defining the correct error limit is also critical for the obtaining the best prediction for the ANN algorithm. Memorizing problem was overcome by increasing the number of point used for training to 50%. Only one hidden layer was used for the network algorithm with a hyperbolic tangent activation function.

Application of the ANN showed that prediction of the DT logs based on NPHI and RILD was successful in the study area with very high CC using single well. Incorporating other wells lowered the training results slightly. NPHI prediction was performed using combination of GR, DT and RILD logs. Incorporating the PCA for data reduction improved the estimation results.

4.3 SEISMIC INVERSION

Interpretation of seismic data is done by using amplitude sections with a limited vertical resolution. The picked reflectors which indicate impedance contrast between two subsequent the layers, are usually not appropriate for interpolating reservoir properties (Duboz et. al., 1998).

Seismic inversion is the process of determining what physical characteristics of rocks and fluids could have produced the seismic record. Simply, it is determining the input by looking at the output. Transforming a noisy, processed seismic trace into a density log or a sonic log is the inverse of transforming these two logs into a synthetic seismogram, hence the name inversion.

In many cases the physical parameters of interest are impedance, velocity and density. It is also possible to move on to an estimation of properties that are more familiar like porosity or even sand/shale ratios or gas saturation. The common methods of performing seismic inversion attempt to remove the effects of the wavelet. This leads to a higher resolution display and in this sense acoustic impedance inversion can be thought of as a form of deconvolution.

Another way to approach the inversion concept is to realize that standard acoustic impedance inversion requires model building that usually incorporates well log data from all the nearby wells. The forward model is created by carefully calibrating the seismic data with log-based synthetic seismograms. Therefore the

final inversion result is a data set that ties all the wells and also honors all the seismic data. In this sense, inversion can also be considered a sophisticated method of integrating well logs and seismic data (Russell, 1988).

Main advantages of inversion application can be summarized as follows:

- AI directly represents layer properties; amplitudes are represent a contrast between layers
- AI improves vertical resolution and layering; amplitudes affected by thin layer interfaces
- AI often free from noise and thin layer interfaces; amplitudes disturbed by noise and rarely display heterogeneities
- AI measured at well location; amplitudes do not (Duboz et. al., 1998).

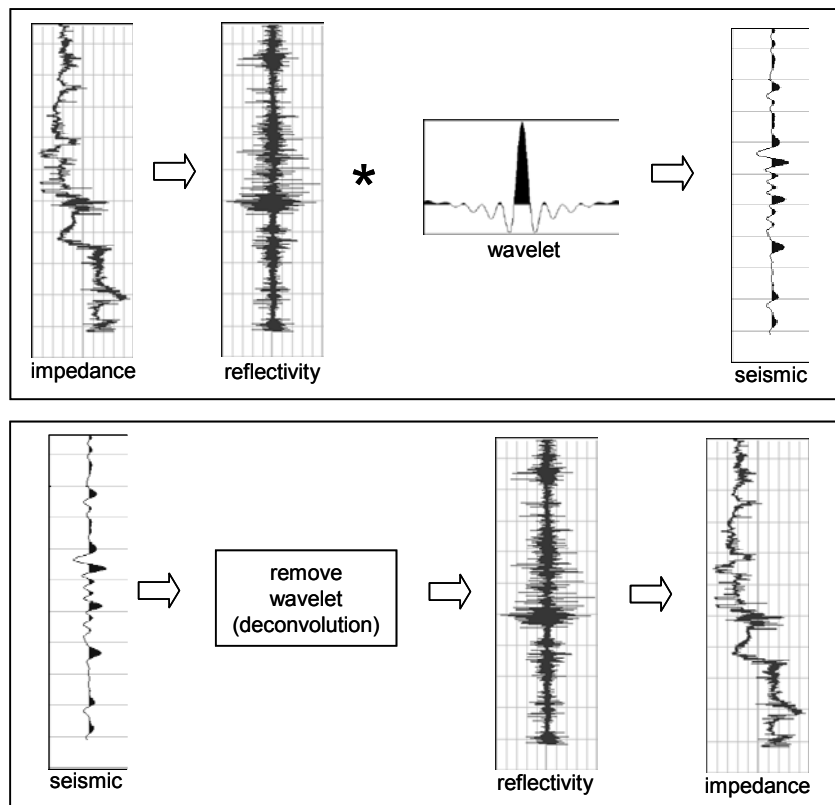


Figure 4.22 Schematic diagrams of the forward and inverse modeling concepts. Above diagram shows how seismic data is obtained with forward solution and diagram below presents the inverse modeling (modified from Russell, 2006).

The synthetic trace was obtained, first by converting the density-velocity model (impedance) to reflectivity model which is the ratio of the reflected wave amplitude to the incident wave amplitude (Lindseth, 1979). Then, a wavelet was

combined with reflectivity series. Inversion starts with removing the wavelet from the amplitude preserved seismic trace to produce reflectivity series. The final product, acoustic impedance, was created from the reflectivity series (Figure 4.22) (Barclay et. al., 2008).

There are many different techniques used in seismic inversion. These can be roughly grouped into two sets of categories: pre-stack vs. post-stack, and seismic resolution vs. well log resolution. Pre-stack techniques are usually applied to pre-processed seismic data before final stack and post-stack inversion applied to amplitude preserved stacked data. The combination of these categories yields four technical approaches to the inversion problem, and the selection of a specific technique depends on the desired objective and the characteristics of the rocks in the subsurface. A more detailed grouping of the seismic inversion techniques can be summarised as (Russell, 1988).

<u>Post-Stack Inversion</u>	<u>Pre-Stack Inversion</u>
<ul style="list-style-type: none"> • Model-Based Inversion • Recursive Inversion <ul style="list-style-type: none"> ○ Narrow Band ○ Sparse-Spike • Travelttime Inversion (Tomography) • Wavefield Inversion 	<ul style="list-style-type: none"> Linear Methods Non-Linear Methods

Understanding the process involved in building the seismic data is the first step to be able to gain some knowledge from the seismic inversion methods. Therefore, the basic convolution model of the seismic trace with its three components, reflectivity, seismic wavelet, and noise will be the initial considerations for any seismic inversion study (Russell, 1988).

Seismic trace simply is obtained by convolving reflectivity series with a wavelet (Oldenburg, 1983) or in more simple terms “replacing each RC with a scaled version of the wavelet and summing the results” (Russell, 1988). This process is usually coarsen the resolution. In time domain, 1D model of the seismic trace can be written as:

$$s(t) = r(t) * w(t) + n(t) \tag{4.3}$$

where; $s(t)$: seismic trace, $r(t)$: earth reflectivity, $w(t)$: seismic wavelet, and $n(t)$: additive noise.

In the frequency domain, convolution operation multiplies the amplitude spectra and adds the phase spectra. If the Fourier transform of the Equation 4.3 was taken:

$$S(f) = R(f) \times W(f) \quad (4.4)$$

where; $S(f)$, $R(f)$, and $W(f)$ are Fourier transform of the $s(t)$, $r(t)$, and $w(t)$ respectively and f is the frequency. The amplitude and the phase spectra of the $S(f)$ can be represented as (Russell, 1988):

$$|S(f)| = |R(f)| \times |W(f)| \quad (4.5)$$

$$|\theta|(f) = \theta_r(f) + \theta_w(f) \quad (4.6)$$

where; $| \cdot |$: amplitude spectrum and θ : phase spectrum. As it can be noted, in frequency domain the problem becomes loss of frequency content.

The reflection coefficient series (RC) show the changes of the shape of the wavelet due to acoustic impedance (AI) change within the layered subsurface. RC at the boundaries of two layers for the normal incidence case is (Oldenburg, 1983):

$$RC_i = \frac{Z_{i+1} - Z_i}{Z_{i+1} + Z_i} = \frac{\rho_{i+1}V_{i+1} - \rho_iV_i}{\rho_{i+1}V_{i+1} + \rho_iV_i} \quad (4.7)$$

where; ρ : density, V : velocity, Z : AI, and i : layer sequence index.

AI usually computed by multiplying the sonic and density logs from the wells, then RC can be extracted. In general, correct RC series cannot be estimated from seismic trace with the effects of amplitude, noise and wavelet. Therefore, most of the post stack inversion methods are only approximations to the real state (Russell and Hampson, 1991).

4.4 ACOUSTIC IMPEDANCE ESTIMATION

Because the AI is the product of the density and velocity, it carries important information regarding the rock physical properties in the subsurface. Therefore, AI logs will be estimated using ANN techniques to assist predicting reservoir properties in the next chapter of this study.

In the study area, there are only three wells, B Yates 11, B Yates 18D, and C Yates 9, have DT and RHOB logs to calculate the AI. To compute the AI logs for these three wells, first sonic logs were corrected against check-shot values, synthetic seismograms were extracted and AI logs were calculated using the corrected sonic velocities. Please refer to Chapter 3, Seismic to Well Tie section for more detailed explanations on sonic correction and synthetic creation.

Figure 4.23 shows calculated AI logs along with the corrected DT and RHOB logs for the wells B Yates 11, C Yates 9 and B Yates 18D. Computed AI logs perfectly follow the main sequence boundaries. One of the most important effects of

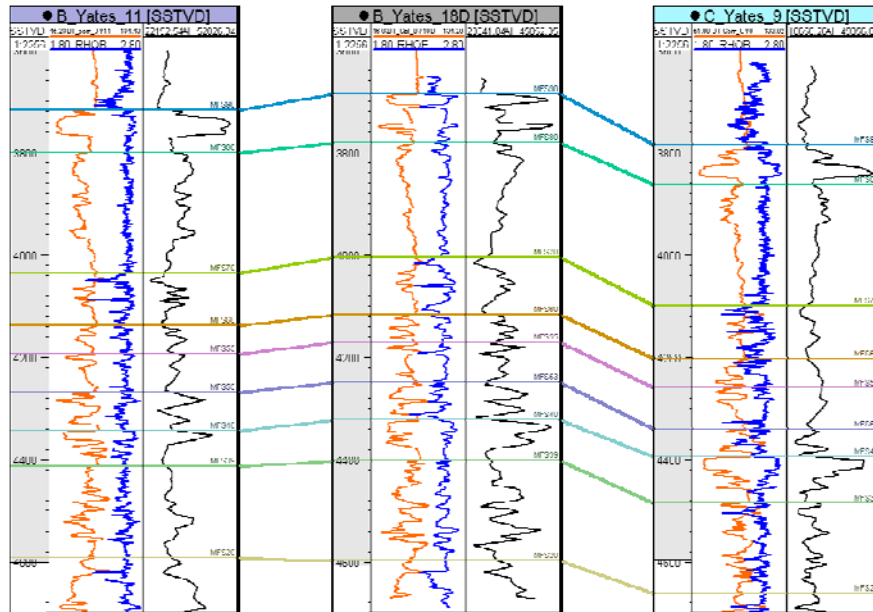


Figure 4.23 Computed AI logs for the wells having DT and RHO logs. Orange and blue curves in the left tracks shows corrected DT and RHO logs and black curve in the right track show computed AI logs.

the convolution appears as a loss of frequency content of the AI logs due to wavelet. Please note that, wavelet used for convolution was extracted along the each borehole from the seismic data.

Dependency of the AI logs to DT values (Equation 4.7) was presented in Figure 4.24. As it can clearly be seen, very high correlation exists between these logs. Correlation coefficients are, -0.91, -0.93, and -0.89 for the wells B Yates 11, C Yates 9, and B Yates 18D respectively. These results are very encouraging that AI logs for the other wells can be easily estimated using this relationship.

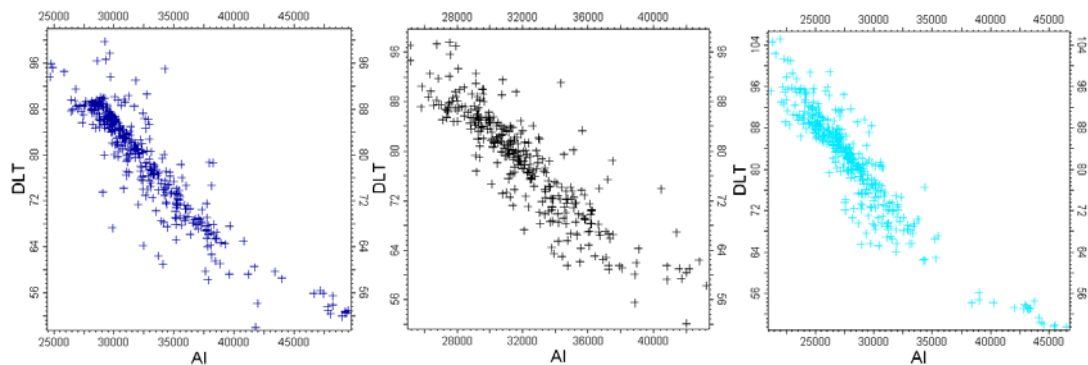


Figure 4.24 Sonic versus Acoustic Impedance cross plots for the wells B Yates 11, B Yates 18D, and C Yates 9.

The drawback at this point is the non-existence of the DT logs for the other wells inside the study area. Therefore, first, DT logs will be estimated, and then AI logs will be computed for the rest of the area.

Estimation of the DT logs was performed using the existing RILD and AI logs for the wells B Yates 11, -18D, and C Yates 9 using ANN methodology. The best ANN parameters were selected with an error sensitivity analysis similar to one applied in Section 4.2. Figure 4.25 shows the estimated DT logs from RILD and AI.

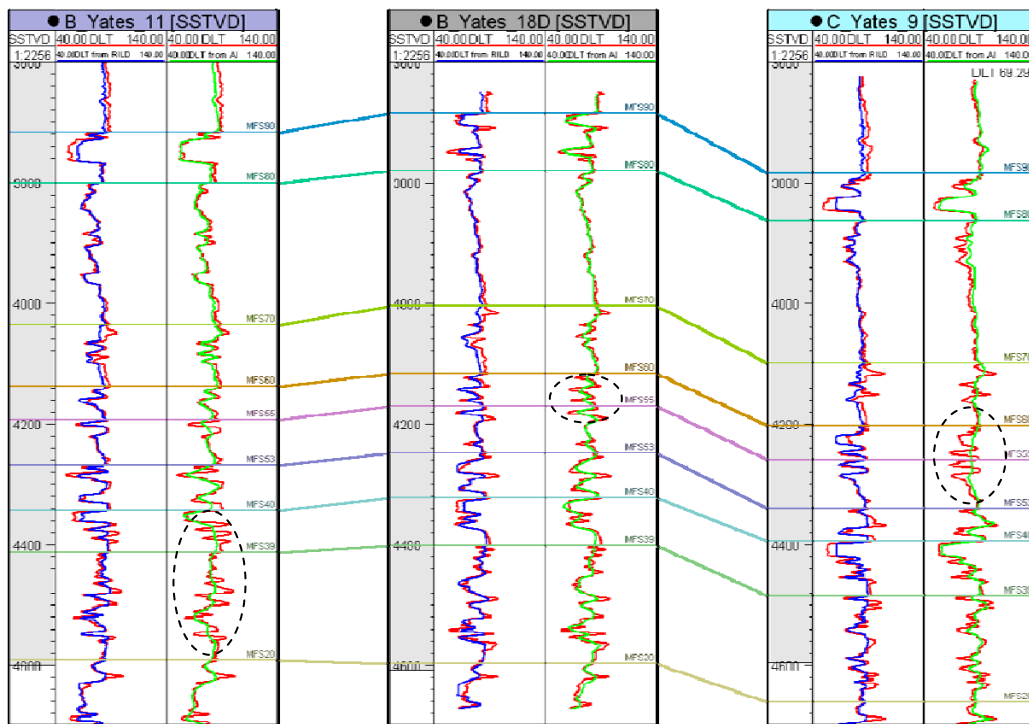


Figure 4.25 DT prediction results for the wells B Yates 11, B Yates 18D, and C Yates 9. Red curve in the tracks show original corrected DT, blue curve estimation results from RILD logs, and green curve presents estimation results from AI logs. Lines between wells show the main formation tops in the study area.

Estimation of the DT from RILD logs represents a good coherency and most of the major deviations of the sonic log were followed by the estimated sonic (blue curves in Figure 4.25). Prediction results from AI logs, on the other hand, present smoother sonic logs (green curves in Figure 4.25). Another noticeable characteristic of this estimation is the loss of frequency content. Sonic estimation contains less peaks especially where the original sonic curve exhibits frequent deviations (dotted circles in Figure 4.25). This is, again, because of the effect of the wavelet used for the AI calculation.

To be able to understand the contribution of each log for estimating the DT, cross plots have been prepared (Figure 4.26).

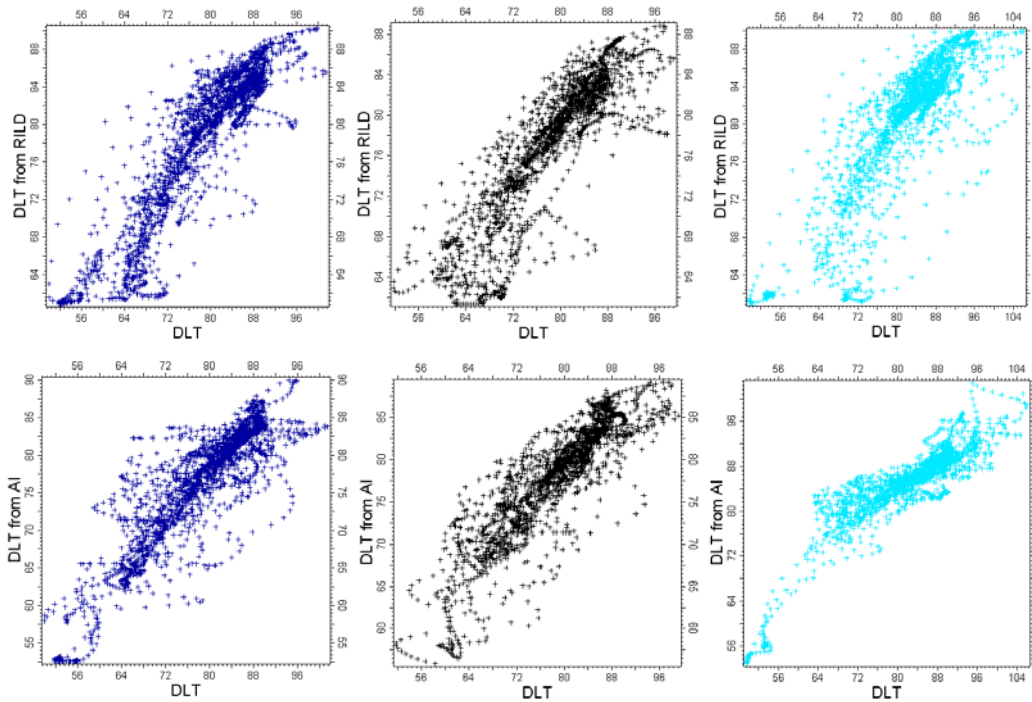


Figure 4.26 Original DT versus estimated DT results from RILD and AI logs. Wells B Yates 11 is in blue, B Yates 18D is in black, and C Yates 9 is in cyan color respectively.

Cross plots in Figure 4.26 represent very close results. The correlation coefficients for the B Yates 11 well are 0.91 and 0.90, for the B Yates 18D well; 0.88 and 0.88, and for the C Yates 9 well; 0.85 and 0.89. One conclusion that can be drawn from this analysis is that there is a high dependency between the sonic and AI values that can be used to predict missing DT logs.

Even though good estimation results were obtained using the RILD and AI logs separately, both logs were used together to predict DT logs to improve the accuracy. Figure 4.27 shows the DT estimation using both resistivity and acoustic impedance logs. As it can be seen, using both RILD and AI logs produced better DT estimation. Even though predicted DT (blue curve) exhibits smoothed DT curve than that of the original DT curve, most of the peaks. Comparison of Figure 4.25 and 4.27 suggests that, using RILD and AI logs produce the best results to predict DT logs in the study area. Correlation plots were also prepared to check the quality of the estimation. Figure 4.28 shows the correlation cross plots for the original and estimated DT logs.

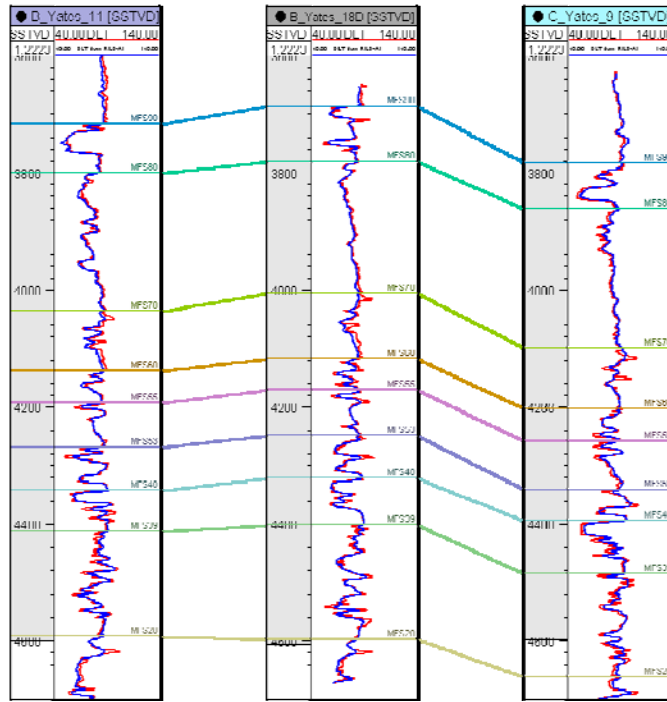


Figure 4.27 DT estimation results from RILD and AI logs for the wells B Yates 11, B Yates 18D, and C Yates 9. Red curve shows original DT and blue curve presents predicted DT curves. Lines between the wells show main sequence boundaries in the study area.

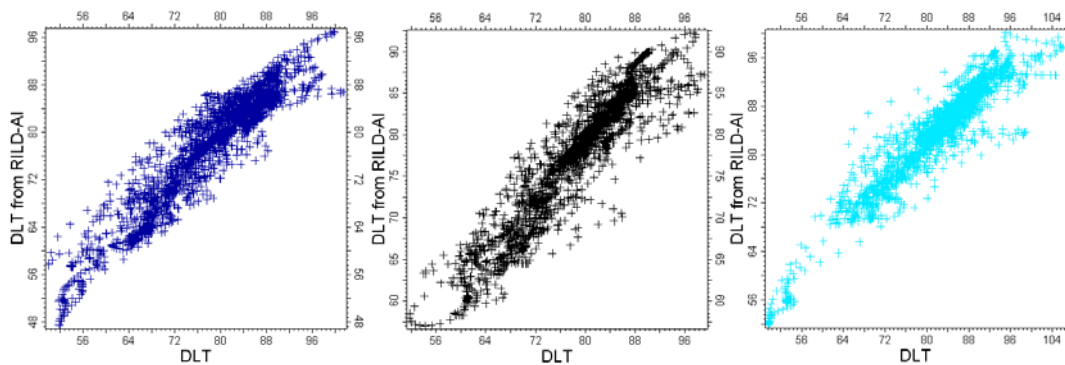


Figure 4.28 DT versus estimated DT cross plots using RILD and AI logs. Plots represent the results for the wells B Yates 11, B Yates 18D, and C Yates 9 respectively.

The correlation coefficients for the cross plots are 0.95, 0.93, and 0.95 respectively for the wells B Yates 11, B Yates 18D, and C Yates 9. These outcomes also indicated that AI logs to be used in seismic inversion study can be estimated using the DT and RILD logs in the study area. Figure 4.29 shows the calculated AI logs for the whole field. As it can be noted some of the wells do not have AI logs due to fact that they do not have either RILD or DT logs to be able to calculate the acoustic impedance.

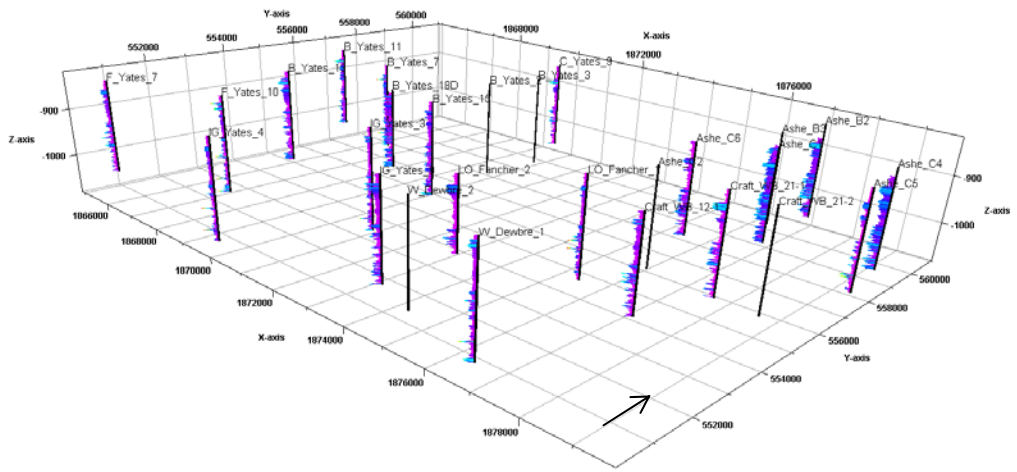


Figure 4.29 Distribution of the computed AI logs in the study area.

CHAPTER 5

ESTIMATION OF RESERVOIR PARAMETERS BASED ON SEISMIC

Availability of 3D seismic data is usually considered as interpretative purposes, namely horizon and fault picking and the results are produced an input to structural model for the study area. Seismic data measures: travel time, amplitude, the character of the events, and the patterns of the events (Sheriff, 1992). Using this information, the following parameters can be computed: seismic velocities, contrast in rock properties, stratigraphic changes, dip, and discontinuities (Chambers, 2002).

On the other hand, there is more information that we can extract from seismic data to provide inputs for the reservoir property estimation studies. If we consider the main sources of reservoir studies are well and 3D seismic data, the integration of these two can bring valuable help for defining the parameters at undrilled locations. The possible correlation between vertically high resolution well logs and laterally dense sampled 3D seismic data can lead to more precise reservoir property description. There are several methods are available to accomplish this task: geostatistics, artificial neural networks, and regression analysis are some of them.

In this part, reservoir properties, porosity, net thickness, saturation etc. will be estimated using well log data and seismic attributes. The results from geostatistical algorithms and neural networks will be discussed at the end of the chapter.

5.1 SEISMIC ATTRIBUTES

Seismic attributes are defined as all of the measured, computed or implied quantities obtained from the seismic data. Attributes computed from seismic data in time domain (due to fact that positioning of the reflectors) is more precise than those in depth domain (Taner, 2000). On the other hand, the correct use of attributes requires special processing steps including zero-phase, true amplitude, and migration. For AI inversion studies, the data must be zero-phase with true amplitude recovered, otherwise the resulting inverted cube will be useless for quantitative interpretation (Chambers, 2002).

Attributes can be classified into two main group based on their direct relations:

Physical Attributes relate the lithology, wave-propagation, and other physical properties directly to seismic measurements. They are divided into two categories: pre-stack and post-stack attributes and they have two sub-classes; instantaneous and wavelet attributes. Instantaneous attributes use sample by sample methodology for computation and change of the attribute values can be reflected along time and space axis. The wavelet attributes, show the characteristics of wavelet and their amplitude spectrum (Taner, 2000). Please refer References section and Appendix C for more information on seismic attributes.

Brown (2001) summarizes the post-stack seismic attributes as:

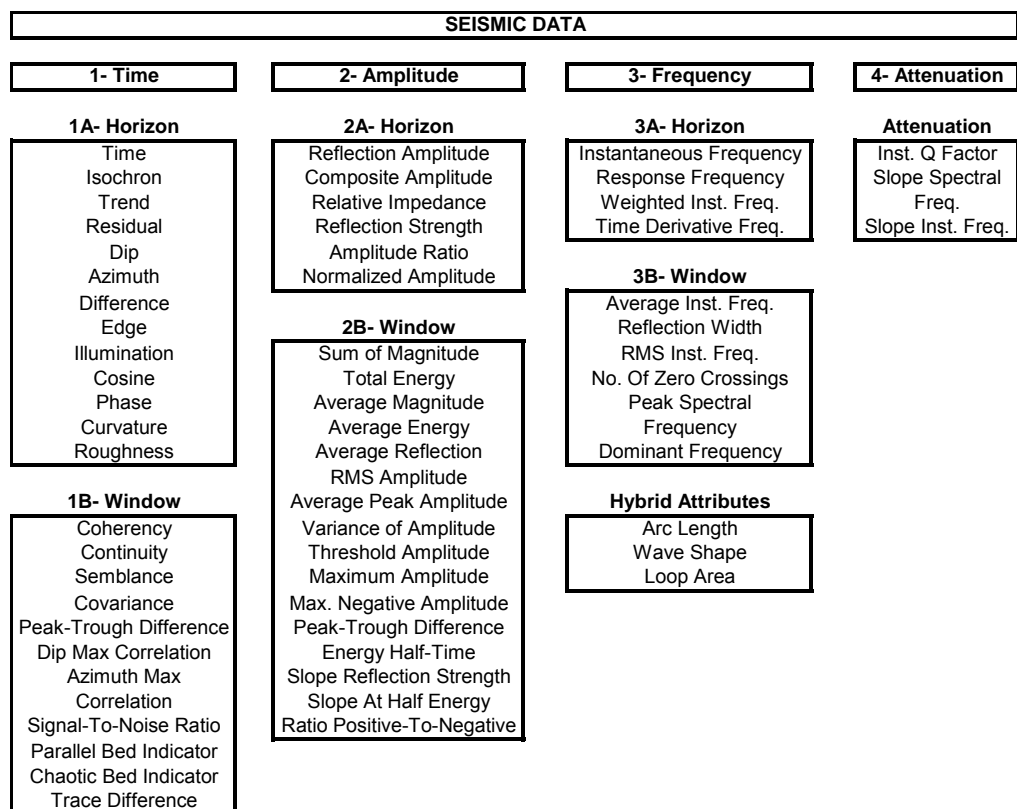


Figure 5.1 Classification of post-stack seismic amplitudes (modified from Brown, 2001).

At this point, selection of suitable seismic attributes becomes very important as they can be misleading for property estimation practices. Cooke (1999) explains the usage of seismic attributes for reservoir characterization studies in a detailed way. In this study, selected attributes will be discussed in the following paragraphs. On the other hand, selecting the proper seismic attributes may not be helpful due to assumptions were made, physical correspondence of the attributes, scale differences with well logs etc.

Assumptions made for the calculation of seismic attributes basically concern to formulations to express the relationship between the seismic signal and interfaces in the subsurface. Another one is the geological validity of the relationship between attributes and well log data. Scale difference between seismic and log data is also a consideration.

In recent years, the number of attributes computed from seismic data increased parallel to the technological advances. As a result, more attributes become available and it was more difficult to select the most appropriate ones. Therefore, before starting the use of attributes it will be very efficient to discard the attributes producing similar responses.

In this study, 25 seismic attributes were extracted from the 3D volume and their correlation was checked against several properties. Table 5.1 shows the correlation of employed attributes against each other.

Table 5.1 Seismic attributes correlation table calculated in this study.

	AP	C	CP	DF	FD	GM	IF	IP	IQ	RI	RA	V	DD
Apparent Polarity (AP)	1	0.0324	0.2859	0.0016	0.0088	0.0246	0.0033	0.0215	0.0164	0.0583	0.0576	0.0103	0.0063
Chaos (C)	0.0324	1	0.0190	0.0616	0.0232	0.5155	0.0760	0.0322	0.1240	0.5545	0.5959	0.4548	0.2528
Cosine of Phase (CP)	0.2859	0.019	1	0.0232	0.0053	0.0119	0.0428	0.0044	0.0219	0.0200	0.0227	0.0151	0.0002
Dominant Frequency (DF)	0.0016	0.0616	0.0232	1	0.0009	0.0132	0.8217	0.0178	0.0641	0.2939	0.2779	0.3116	0.1042
First Derivative (FD)	0.0088	0.0232	0.0053	0.0009	1	0.0073	0.0055	0.6862	0.0516	0.0154	0.0156	0.0071	0.0188
Gradient Magnitude (GM)	0.0246	0.5155	0.0119	0.0132	0.0073	1	0.1163	0.0087	0.0656	0.4965	0.5561	0.1190	0.0778
Instantaneous Frequency (IF)	0.0033	0.0760	0.0428	0.8217	0.0055	0.1163	1	0.0354	0.0460	0.1144	0.1028	0.1575	0.2322
Instantaneous Phase (IP)	0.0215	0.0322	0.0044	0.0178	0.6862	0.0087	0.0354	1	0.0352	0.0222	0.0211	0.0095	0.0399
Instantaneous Quality (IQ)	0.0164	0.1240	0.0219	0.0641	0.0516	0.0656	0.0460	0.0352	1	0.1500	0.1454	0.1350	0.0964
Reflection Intensity (RI)	0.0583	0.5545	0.0200	0.2939	0.0154	0.4965	0.1144	0.0222	0.1500	1	0.9919	0.6332	0.2157
RMS Amplitude (RA)	0.0576	0.5959	0.0227	0.2779	0.0156	0.5561	0.1028	0.0211	0.1454	0.9919	1	0.6419	0.2518
Variance (V)	0.0103	0.4548	0.0151	0.3116	0.0071	0.1190	0.1575	0.0095	0.1350	0.6332	0.6419	1	0.2991
Dip Deviation (DD)	0.0063	0.2528	0.0002	0.1042	0.0188	0.0778	0.2322	0.0399	0.0964	0.2157	0.2518	0.2991	1
Envelope (E)	0.0582	0.6145	0.0297	0.3023	0.0254	0.5639	0.0948	0.0241	0.1686	0.9675	0.9790	0.6301	0.2674
Instantaneous Bandwidth (IB)	0.0078	0.2553	0.0350	0.5943	0.0221	0.1666	0.0746	0.0291	0.2975	0.4044	0.3880	0.3533	0.1539
Iso-Frequency Component (IFQ)	0.0250	0.1646	0.0211	0.5277	0.0100	0.0118	0.4955	0.0264	0.0694	0.3048	0.3010	0.3808	0.0015
Local Flatness (LF)	0.0186	0.7072	0.0087	0.0618	0.0199	0.3408	0.1038	0.0321	0.1238	0.4628	0.4903	0.4899	0.2516
Local Structural Azimuth (LSA)	0.0116	0.0223	0.0023	0.0010	0.0093	0.0441	0.0074	0.0042	0.0132	0.0207	0.0179	0.0046	0.0127
Local Structural Dip (LSD)	0.0232	0.4875	0.0348	0.0157	0.0154	0.2622	0.1744	0.0112	0.1523	0.3974	0.4588	0.4839	0.6362
Original Amplitude (OA)	0.3167	0.0403	0.8640	0.0248	0.0084	0.0381	0.0397	0.0009	0.0354	0.0578	0.0619	0.0068	0.0164
Phase Shift (PS)	0.3167	0.0403	0.8640	0.0248	0.0084	0.0381	0.0397	0.0009	0.0354	0.0578	0.0619	0.0068	0.0164
Quadrature Amplitude (QA)	0.0095	0.0275	0.0004	0.0023	0.9620	0.0173	0.0105	0.7131	0.0544	0.0402	0.0395	0.0156	0.0295
Relative Acoustic Amplitude (RAA)	0.0573	0.0447	0.1360	0.0114	0.8284	0.0470	0.0156	0.6624	0.0611	0.0966	0.0954	0.0342	0.0484
Second Derivative (SD)	0.3494	0.0077	0.7420	0.0116	0.0032	0.0150	0.0145	0.0055	0.0397	0.0474	0.0424	0.0027	0.0073
Structural Smoothing (SS)	0.2998	0.0481	0.8330	0.0316	0.0065	0.0491	0.0458	0.0089	0.0319	0.0575	0.0636	0.0051	0.0192

	E	IB	IFQ	LF	LSA	LSD	OA	PS	QA	RAA	SD	SS
Apparent Polarity (AP)	0.0582	0.0078	0.0250	0.0186	0.0116	0.0232	0.3167	0.3167	0.0095	0.0573	0.3494	0.2998
Chaos (C)	0.6145	0.2553	0.1646	0.7072	0.0223	0.4875	0.0403	0.0403	0.0275	0.0447	0.0077	0.0481
Cosine of Phase (CP)	0.0297	0.0350	0.0211	0.0087	0.0023	0.0348	0.8640	0.8640	0.0004	0.1360	0.7420	0.8330
Dominant Frequency (DF)	0.3023	0.5943	0.5277	0.0618	0.0010	0.0157	0.0248	0.0248	0.0023	0.0114	0.0116	0.0316
First Derivative (FD)	0.0254	0.0221	0.0100	0.0199	0.0093	0.0154	0.0084	0.0084	0.9620	0.8284	0.0032	0.0065
Gradient Magnitude (GM)	0.5639	0.1666	0.0118	0.3408	0.0441	0.2622	0.0381	0.0381	0.0173	0.0470	0.0150	0.0491
Instantaneous Frequency (IF)	0.0948	0.0746	0.4955	0.1038	0.0074	0.1744	0.0397	0.0397	0.0105	0.0156	0.0145	0.0458
Instantaneous Phase (IP)	0.0241	0.0291	0.0264	0.0321	0.0042	0.0112	0.0009	0.0009	0.7131	0.6624	0.0055	0.0089
Instantaneous Quality (IQ)	0.1686	0.2975	0.0694	0.1238	0.0132	0.1523	0.0354	0.0354	0.0544	0.0611	0.0397	0.0319
Reflection Intensity (RI)	0.9675	0.4044	0.3048	0.4628	0.0207	0.3974	0.0578	0.0578	0.0402	0.0966	0.0474	0.0575
RMS Amplitude (RA)	0.9790	0.3880	0.3010	0.4903	0.0179	0.4588	0.0619	0.0619	0.0395	0.0954	0.0424	0.0636
Variance (V)	0.6301	0.3533	0.3808	0.4899	0.0046	0.4839	0.0068	0.0068	0.0156	0.0342	0.0027	0.0051
Dip Deviation (DD)	0.2674	0.1539	0.0015	0.2516	0.0127	0.6362	0.0164	0.0164	0.0295	0.0484	0.0073	0.0192
Envelope (E)	1	0.4492	0.3098	0.5086	0.0121	0.4661	0.0683	0.0683	0.0484	0.1046	0.0327	0.0720
Instantaneous Bandwidth (IB)	0.4492	1	0.2370	0.2929	0.0156	0.2482	0.0326	0.0326	0.0331	0.0599	0.0211	0.0258
Iso-Frequency Component (IFQ)	0.3098	0.2370	1	0.1683	0.0193	0.0870	0.0133	0.0133	0.0145	0.0280	0.0055	0.0142
Local Flatness (LF)	0.5086	0.2929	0.1683	1	0.0328	0.4363	0.0265	0.0265	0.0264	0.0468	0.0028	0.0341
Local Structural Azimuth (LSA)	0.0121	0.0156	0.0193	0.0328	1	0.0067	0.0022	0.0022	0.0073	0.0017	0.0146	0.0037
Local Structural Dip (LSD)	0.4661	0.2482	0.0870	0.4363	0.0067	1	0.0502	0.0502	0.0246	0.0482	0.0153	0.0570
Original Amplitude (OA)	0.0683	0.0326	0.0133	0.0265	0.0022	0.0502	1	1.0000	0.0051	0.1510	0.8407	0.9746
Phase Shift (PS)	0.0683	0.0326	0.0133	0.0265	0.0022	0.0502	1.0000	1	0.0051	0.1510	0.8407	0.9746
Quadrature Amplitude (QA)	0.0484	0.0331	0.0145	0.0264	0.0073	0.0246	0.0051	0.0051	1	0.9368	0.0070	0.0068
Relative Acoustic Amplitude (RAA)	0.1046	0.0599	0.0280	0.0468	0.0017	0.0482	0.1510	0.1510	0.9368	1	0.1332	0.1441
Second Derivative (SD)	0.0327	0.0211	0.0055	0.0028	0.0146	0.0153	0.8407	0.8407	0.0070	0.1332	1	0.7560
Structural Smoothing (SS)	0.0720	0.0258	0.0142	0.0341	0.0037	0.0570	0.9746	0.9746	0.0068	0.1441	0.7560	1

In Table 5.1, color codes represents the correlation degree; colors from white to red shows high correlation. As it can be inferred from this table, the highest correlations (>0.8) were found between the following attribute pairs (Table 5.2):

Table 5.2 The most correlated seismic attributes and their correlation coefficients (refer to Table 5.1 for explanation of the abbreviations).

OA	CP	0.8640
PS	CP	0.8640
IF	DF	0.8217
QA	FD	0.9620
RAA	FD	0.8284
RA	RI	0.9919
E	RI	0.9675
E	RA	0.9790
PS	OA	1.0000
SD	OA	0.8407
SS	OA	0.9746
SD	PS	0.8407
SS	PS	0.9746
RAA	QA	0.9368

As it can be inferred from the above table, one of the attributes of each pair with high CCs was not used to estimate the properties in the study area. This is mainly, due to fact that if two attributes are correlated well, it means that the contribution of them and results obtained will be closer to each other. These attributes produced from seismic data represent the properties of the reflector interfaces and therefore they are limited to resolution of the seismic data. On the other hand, acoustic impedance (AI), which was explained and produced in previous chapters, exhibit different characteristics. AI is basically the product of velocity and density and reflects the rock or layer property. Therefore it can be linked to reservoir porosity, pore fluids, lithology etc.

Principal Component Analysis (PCA) is also applied to remaining attributes to be able to reduce the uncorrelated data size and bring up the relationship between correlated attributes easily.

The methodology used in this study is data originated, means that relationships between seismic attributes and logs were obtained directly from the data itself. Relationships can be allowed or disregarded. Therefore, the data from different area may show different relationship characteristics.

5.2 GEOSTATISTICAL APPROACH

As it was stated in Chapter 3, in the initial state, the data quality was checked and the errors were removed from. To be able to build the static model, fine layers with 1 ft intervals were created horizons were embedded into the model.

In this part of the study, the reservoir properties will be estimated using geostatistical techniques and empty static model will be filled with these properties. In the study area, there were several well logs are available. On the other hand, gross thickness, net pay, porosity, and water saturation values do not exist as continuous logs. Therefore, neutron-porosity (NPHI) log will be considered as a reservoir property to be estimated.

First of all, NPHI values will be sampled along the main formation tops where horizon interpretations were performed. Because NPHI logs are available for 12 wells among 38 wells, remaining NPHI logs were calculated from estimated AI logs using 1-hidden layer GRNN algorithm. Then, geostatistical tools will be employed to distribute the values in the area with and without help of the seismic data.

Estimated NPHI logs were checked for errors and outliers using histogram and well section views. Some degree of smoothing was applied to logs to remove the sharp effects of AI logs. Recalling Chapter 3, Figure 3.27, model is divided into cells in X-Y and Z direction and in this stage none of the cells have been assigned a value, they are simply empty. To be able to assign them a certain property values, well logs needs to be upscaled. Upscaling can be defined as assigning values to cells in 3D grid that is penetrated by wells. In this case, each cell should have only one value and well log information can be used in property modeling, for instance, distribution of property values between wells.

Upscaling

Averaging of the log values directly depends on the cell thickness. Figure 5.2 show this effect. The track on the left is original NPHI log, second track shows upscaled NPHI with 2 ft interval, and last track presents upsclaed NPHI log with 10 ft layer thickness. As it can be concluded easily, defining finer cell thickness intervals allow better representation of the original log curve values. Because the purpose of this process to assign values from logs to each cell in the model by averaging methods, the final modeled property will be directly depended on the quality of the

upscaled logs. In the following figure, it is clear that, smaller cell thicknesses may provide more realistic representation of the real situation.

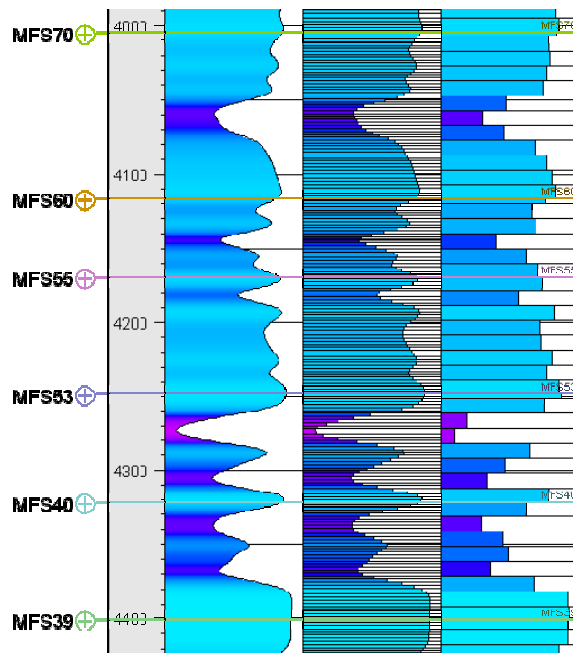


Figure 5.2 Upscaled NPHI logs for the Well B Yates 18D. The first track is original NPHI log, second track is upscaled with 2 ft thickness, and last track is upscaled with 10 ft layer interval.

Quality checking of the upscaled values is another step after the process was completed. Figure 5.3 shows the histogram of the original and upscaled logs. Values of the upscaled logs are very close to original values. As the 10 ft upscaled logs can represent the original values, 10 ft layer thickness will be used through the area.

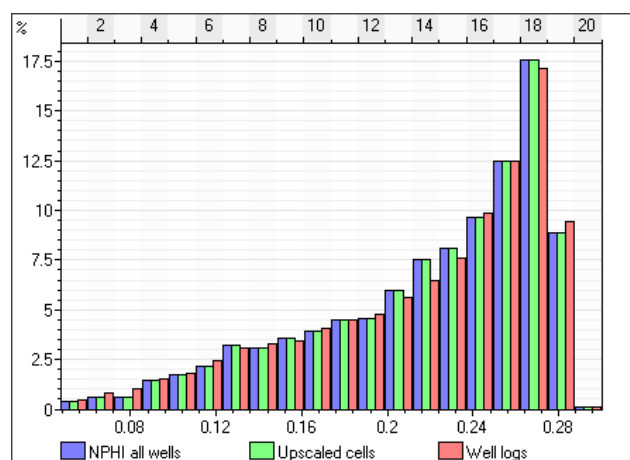


Figure 5.3 Histogram of the original, upscaled, and to be modeled NPHI logs.

Upscaling the logs into the model will be followed by geostatistical data analysis. To be able to define the heterogeneities in the area, first, anisotropies will be defined. Variogram analysis will be used to define the anisotropy direction for the upscaled properties. Please refer to Chapter 2 for more detailed information about variogram analysis.

Exploratory Data Analysis

Figure 5.4 shows the variogram map for the upscaled NPHI logs for the following parameters: number of lag in X-Y direction is 4, search distance in X-Y direction is 5,000 ft, and vertical search distance is 3 layers. Dotted red line on the map represents the major direction for anisotropy, meaning, in this direction sample values are close to each other and does not vary. On the other hand dotted black arrow is placed perpendicular to major direction and indicates the minor direction for anisotropy. In this direction, and within this distance values change rapidly. The anisotropy mentioned in this case is the zonal anisotropy, where sills are different and ranges are same for different directions.

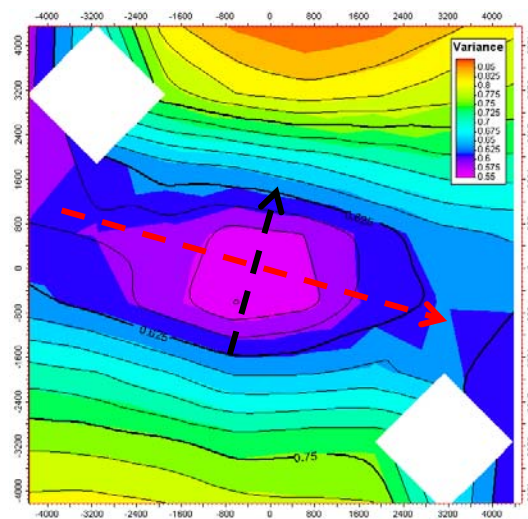


Figure 5.4 Variogram map for the upscaled NPHI logs. Empty partitions in the map are areas where variance cannot be calculated.

Variogram map presents variograms that have been calculated for several directions. The center of the map shows 0.0 lag distance and from this point the lag distance increase in different directions. As it can be noted in X-Y axes in the map, coordinates do not correspond to distance units in the project; they are simply

positive and negative lag distances. Contour values on the map correspond to variance values calculated for a specific lag distance on this particular point.

Figure 5.5 show vertical and horizontal sample variograms calculated from the variogram map of the NPHI upscaled logs. The left window shows the vertical sample variogram. The main goal of the horizontal variogram analysis is to: 1) determine if anisotropy is present, 2) quantify the degree of anisotropy in terms of major and minor variogram model ranges. The blue line was calculated using the horizontal search radius of 5,000 ft and 4 lags, and the green line was constructed with same radius and same number of lags. In both variograms 30 ft Z-range was used. The right window represents sample variogram calculated for horizontal direction. X-Y range, number of lags and Z-range were kept same with the vertical variograms but the -60 degree which is the major direction (green line) was used for the orientation.

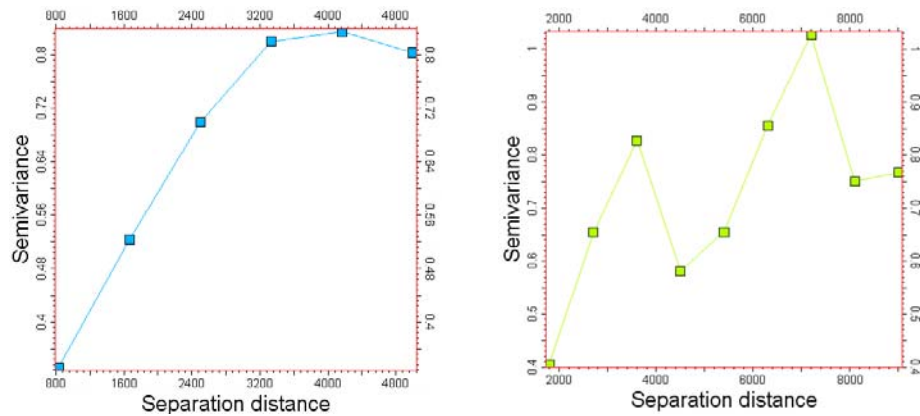


Figure 5.5 Sample variograms calculated for upscaled NPHI logs. The left plot is the sample vertical variogram and the right plot is the sample horizontal variogram for major direction.

As it can be seen in Figure 5.5, the vertical variogram show more reliable curves than that of the horizontal variogram. The reason of this variation is that the density of number of samples in vertical and horizontal direction is different. Sampling is always denser in vertical direction (throughout the well bore) compared to that of the horizontal direction (well spacing).

After completing the structural model which is a framework of the reservoir model the next goal is to populate the entire framework of cells with reservoir properties. This could be the discrete data like facies or petrophysical properties like porosity, permeability, water saturation etc. Existing well data will be used as the control points for feeding the interpolation or simulation algorithms used in this step.

Many algorithms (depending on the data type and the choice of the algorithm), would require parameters which describe the spatial relationship of the data points supplied to them. Therefore, finding out the spatial characteristics of the data (how do they vary in space, is the variation smooth or sudden, is there any anisotropy present i.e. variation specific to any direction, is the distribution of data showing some patterns) is a very important step. This can be time consuming but essential as the final output from the algorithms are dependant on how these spatial characteristics are defined.

Data analysis process tries to answer the following questions:

- Is there a trend in the data set?
- Is there a pattern by which the facies proportion changes laterally and vertically?
- Is there any pattern of correlation between a seismic attributes and the facies?
- What are the variogram parameters like Range (in the major, minor and vertical directions), nugget, and the variogram type etc. for the properties to be modeled?

The first step for the data analysis procedure is the data transformations. Figure 5.6 show typical workflow for this process. Transformations were applied at the initial state, among them 1D, 2D, 3D, scale shift, and logarithmic are the common ones. The importance of removing trend from the data is the assumption of *stationary*. This requires that data should not contain any trend, in other words, the mean of the data should not be change with direction.

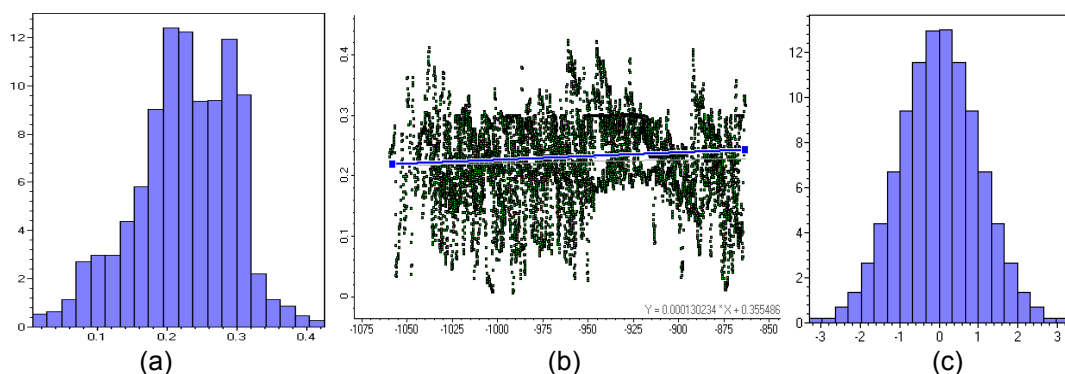


Figure 5.6 Data transformation process for the NPHI logs. (a) Input histogram of the original NPHI logs, (b) trend line for the NPHI values at all well locations (Y-axis) versus depth values along Z-axis, and (c) trend-free normally distributed log values.

Some certain simulation algorithms, e. g. Gaussian Simulation, require that the data should be normally distributed. Removing trend(s) from the data does not mean that the final result will be trend free. Back transformation is usually applied to data at the last stage of the process and all original values kept as they are. Data follows the original distribution and preserves the original trends.

Variogram Analysis

The next step is the variogram analysis. As it was discussed in Chapter 2, variogram study forms the base of the stochastic modeling process. Basically, it describes the natural variations in the data set in specific directions. In general, variography involves three steps (please refer to Appendix D for more details on variogram parameters):

- Calculating experimental variogram
- Create the model variogram
- Obtain the variogram parameters

Basically, dissimilarity between data points can be defined by the variogram as a function of the distance h , lag distance (Equation 2.16). If two different properties were included, the cross variogram (Armstrong, 1998) can be defined by Equation 2.18.

Now, the effect of parameter selection on variogram modeling will be investigated. Figure 5.7 shows the experimental and modeled vertical variograms for the NPHI logs. In Figure 5.7 a, upscaled log were used with 10 ft lag distance, 200 ft search radius, 50 ft band width. Grey line represents the experimental variogram and the blue line shows the modeled variogram. Black squares show averaged semi-variance and bars represent the number of sample pairs in each lag. Fluctuations on the averaged semi-variance values represent the existence of the trend on the data. As it was stated in previous paragraphs, this trend will be removed during modeling and added back at the end of the process. Figure 5.7 b shows the same upscaled logs with different lag parameter which is 44 ft in vertical direction. If we consider that the vertical resolution of the upscaled NPHI log was 10 ft, obtaining a reasonable variogram model is difficult using coarse lag distances. In Figure 5.7 c, the only parameter changed is the search radius, which was selected as 100 ft. A dramatic change can easily be seen on the variograms. The last variogram model was obtained using the original logs instead of upscaled logs. In this model, the number of data points was increased and the effect of the trend is smoothly removed due to fact that the data is displayed in real coordinates instead

of XYZ coordinate system which was used in previous three modeled variograms. As a result, parameter selection for the modeled variograms is direct effects on obtaining a better variogram models and eventually producing better realizations of the properties.

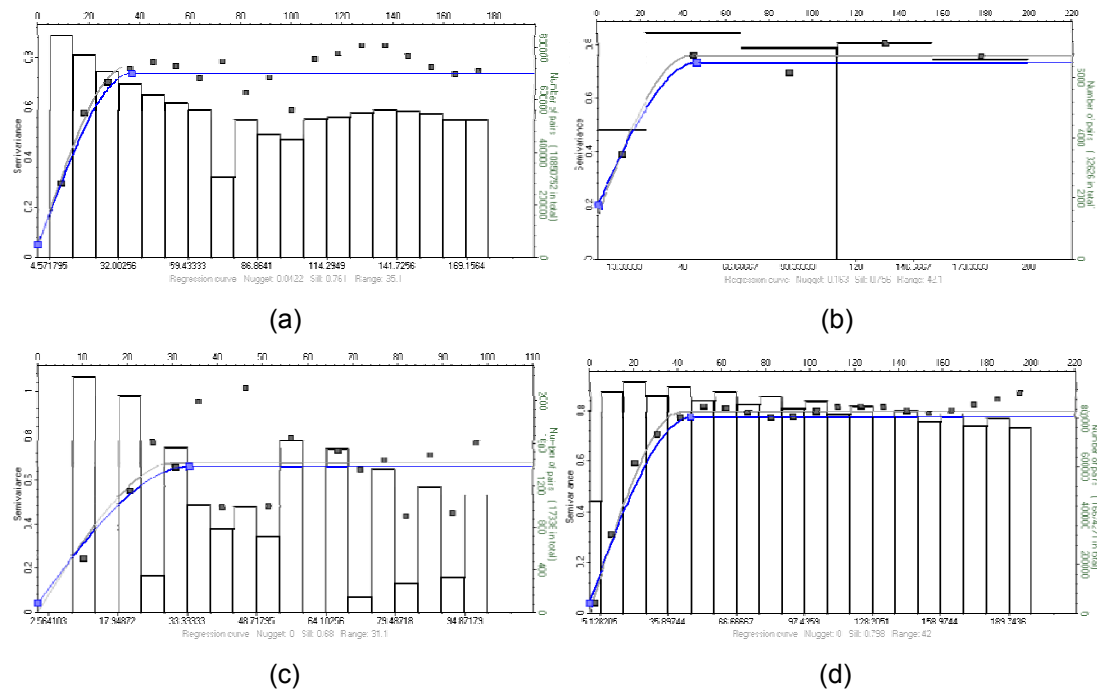


Figure 5.7 Experimental (grey line) and modeled variograms (blue line) for vertical direction for the NPHI logs. See text for more details.

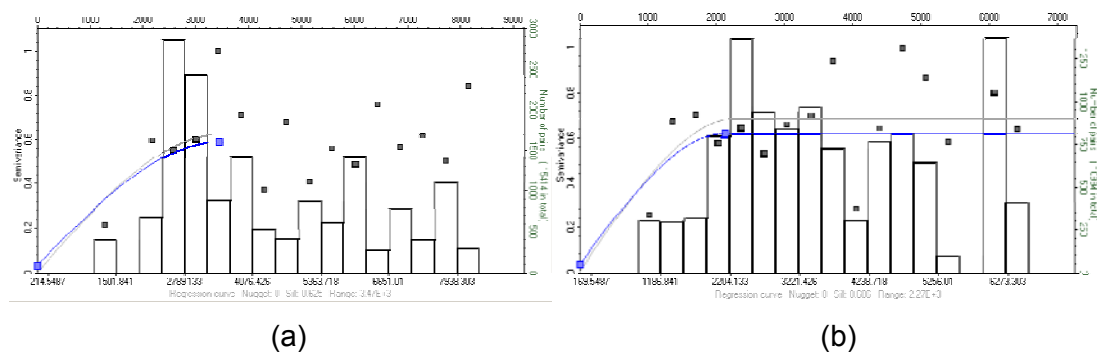


Figure 5.8 Experimental (grey line) and modeled variograms (blue line) for horizontal major and minor directions for the NPHI logs.

Because well data is usually sparse in horizontal direction, obtaining a considerable variogram model is often difficult (Figure 5.8). Therefore one should always expect to get more reasonable variogram models in vertical direction where

the sampling is very dense. Another aspect during variogram modeling is the considering the stratigraphic intervals in vertical direction. The analysis should be done separately for each interval as they may represent different geological characteristics.

Sequential Gaussian Simulation (SGS)

Now, the upscaled properties can be distributed to area. First, Sequential Gaussian Simulation (SGS) algorithm will be used for estimation. In SGS, desirable variables were produced using conditional distributors. The algorithm works as follows: $Z(x_n)$ where x is the location and $n=1,2,3,\dots,N$. The objective of the algorithm is generating multiple realizations of; $z^l(x_n)$ where, $l=1,2,3,\dots,L$ using data itself and variogram models.

Multivariate distributions of N -point can be expressed as N -one point conditional cumulative distribution functions (CDF) as (Caers, 2000);

$$F(x_1, \dots, x_N; z_1, \dots, z_N | (n)) = F(x_N; z_N | (n + N - 1)) * F(x_{N-1}; z_{N-1} | (n + N - 2)) \dots (5.1)$$

where; $F(x_N; z_N | (n + N - 1))$ is the conditional CDF of $Z(x_N)$.

This decomposition allows producing a realization by visiting each location. The algorithm works as following:

- Determine the CDF representing the model
- Transform the input data into normal distribution
- Generate a random path within the grided model and calculate the mean and the standard deviation at the first visited grid node x ,
 - At unknown point x calculate the value (kriging e.g.) using neighbouring data and already estimated values (if exist)
 - Calculate the conditional cumulative distribution function (CCDF) based on original and previously simulated data
 - Estimate a simulated value from CCDF, CCDF is updated continuously and simulated values is drawn from CCDF
 - Go to another grid node (random path by seed number)
 - Back transform the data into original distribution after simulation is done

In this part, SGS results from upscaled NPHI logs will be discussed and then, few well which were not included into the simulation and used for correlation purposes.

Four different realizations were obtained using random seed numbers. Spatial correlation was taken from the variogram analysis mentioned in previous paragraphs. Simple kriging was used to estimate unknown values and output distribution was taken from the upscaled NPHI logs. Figure 5.9 shows the results of SGS algorithm.

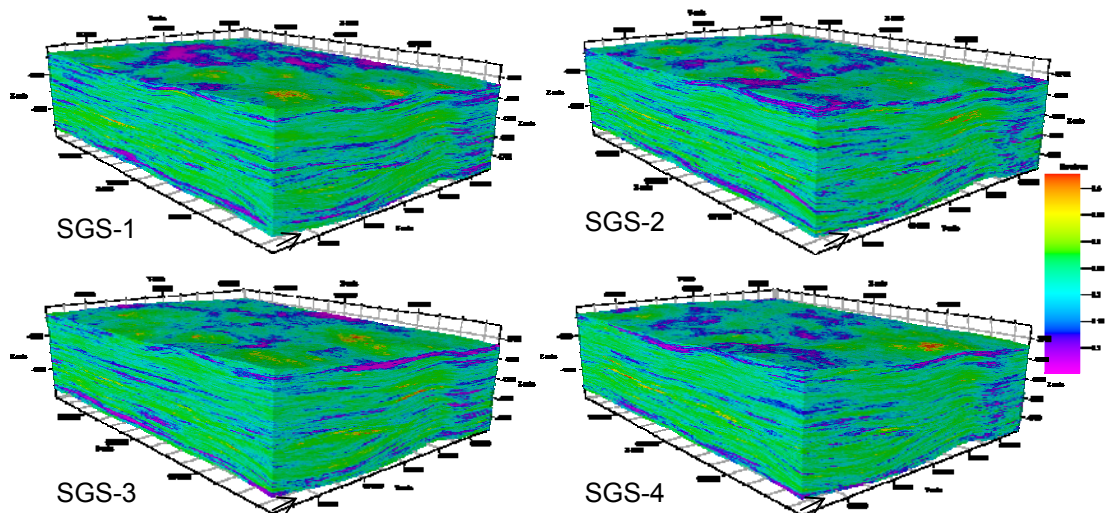


Figure 5.9 SGS realizations using upscaled NPHI logs.

As it can clearly be seen from the simulation results, each realization has different results than the others. This is basically the idea behind the algorithm, the cell visitation order to estimate the unknown values decided by the random seed number. As the starting point changes, the result changes as well. Histograms of these runs can be seen in Figure 5.10. For the first three runs, simulation results are similar to upscaled NPHI values, where as, for the last run; there is difference through high values between the simulated and upscaled logs. On the other hand, original log values have some deviations from the upscaled and naturally simulated values. Table 5.3 shows the summary statistics for the simulated property.

Table 5.3 Summary statistics for the SGS simulation results.

Name	Min	Max	Delta	N	Mean	Std	Var	Sum
Upscaled	0.05	0.37	0.32	2081	0.22	0.05	0.00	460.08
Well logs	0.05	0.40	0.35	39765	0.22	0.06	0.00	8728.94
Property	0.05	0.43	0.38	7161570	0.22	0.05	0.00	1580506.17
Property	0.05	0.43	0.38	7161570	0.22	0.05	0.00	1577202.40
Property	0.05	0.43	0.38	7161570	0.22	0.05	0.00	1575252.46
Property	0.05	0.43	0.38	7161570	0.23	0.05	0.00	1612155.56

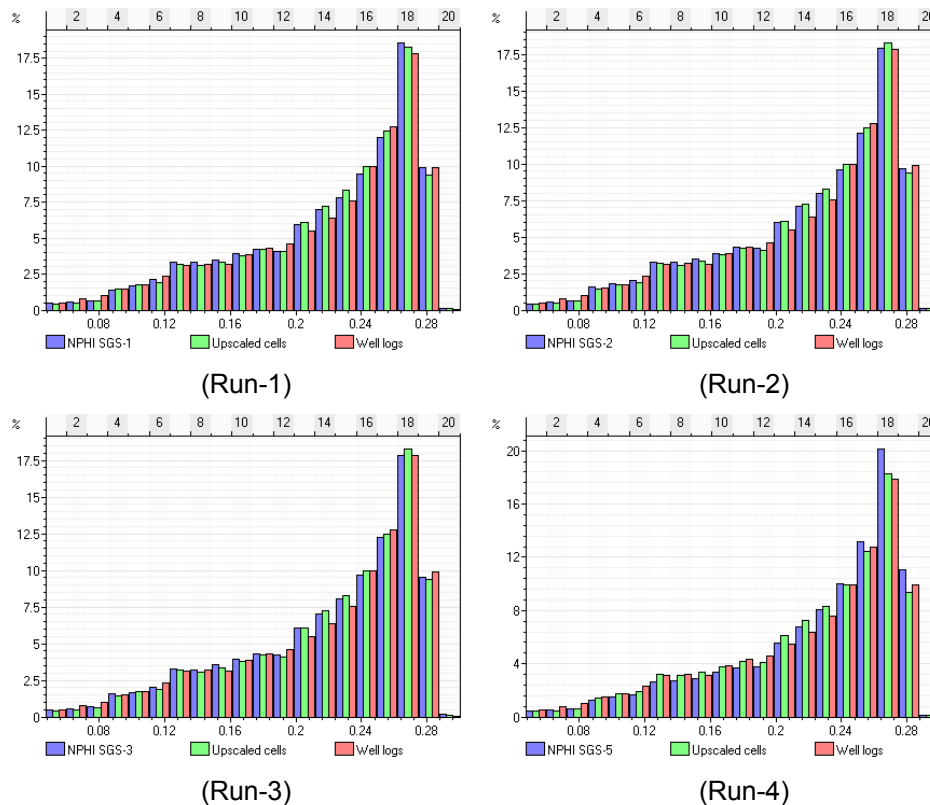


Figure 5.10 Histograms of the simulated, upscaled, and original NPHI logs for four runs respectively.

As it can be inferred from the summary statistics, all statistical measurements have same values except summation of the values. This result also indicates that SGS outcome changes depending on the start position of the estimation. Now, the results can be compared with the upscaled NPHI logs to be able to make quality checking of the simulation. NPHI logs were extracted from three well locations selected randomly (away from each other) throughout the model area. Figure 5.11 shows the comparison of original NPHI logs versus NPHI estimations from SGS simulation runs for the wells LO Fancher 1, B Yates 7, and Ashe C 1 respectively. Please note that the resolution of the derived synthetic NPHI logs from simulation is same as the upscaled logs.

SGS simulation results were showed close values at the control well locations but considering the precise definition of the reservoir parameters, this relationship can be used to some extends. This is mainly due to fact that, small number of simulation runs cannot be enough to obtain more precise results. Suggestion at this point can be made that it more likely that if the number of realizations increase, more realistic results can be obtained as the algorithm, after certain number of simulations, will start to produce similar results.

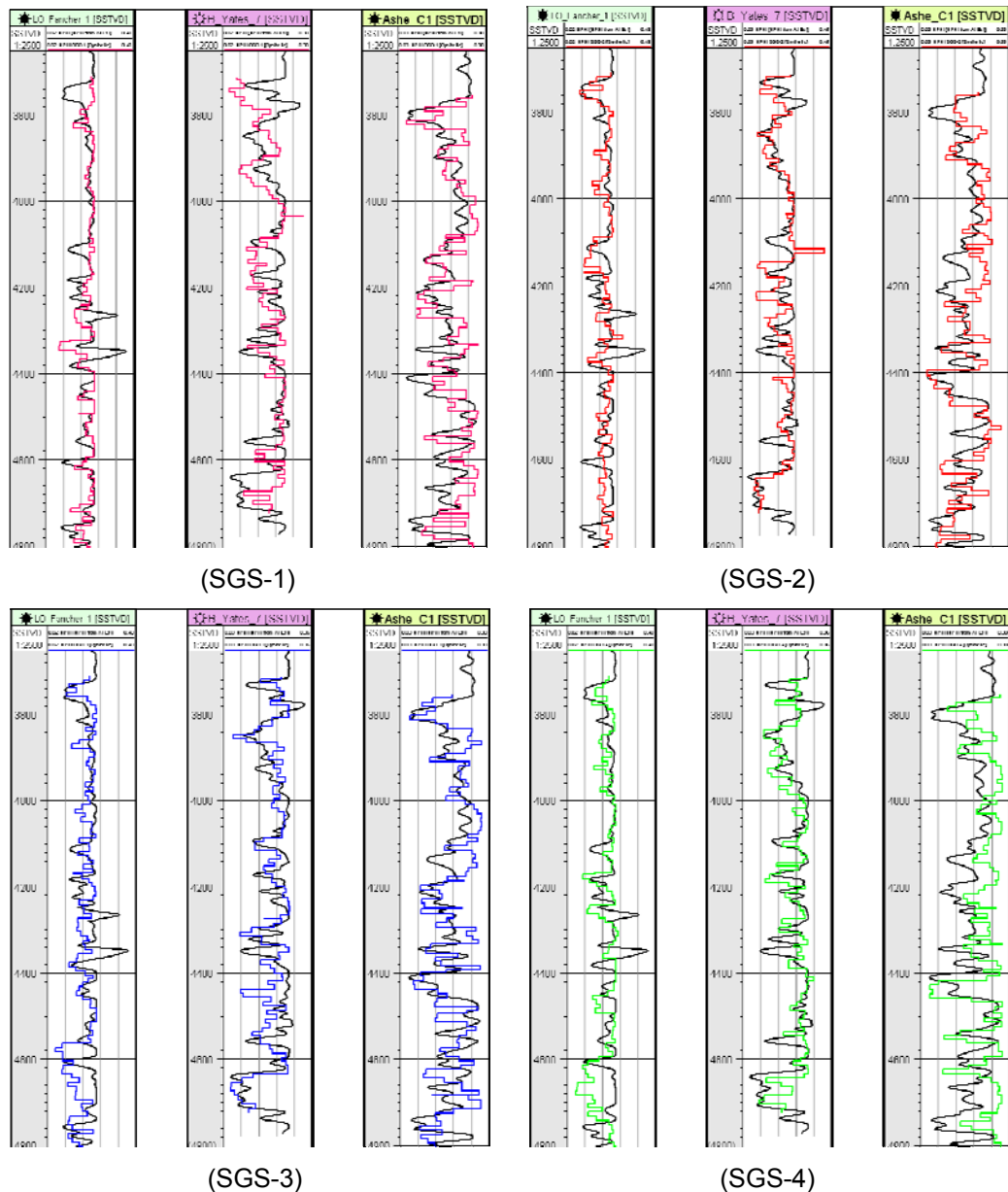


Figure 5.11 Comparison of original NPHI logs and SGS simulation results for the wells LO Fancher 1, B Yates 7, and Ashe C 1 respectively. Black curve shows original NPHI logs and pink, red, blue, and green curves show the results of the simulations.

Cokriging and Collocated Cokriging

In this part, estimation of the properties will be performed using a secondary variable, e.g. a seismic attribute. Kriging is an estimation technique which tries to solve the linear equation system with known variogram parameters and unknown kriging weights (see Chapter 2).

In cases, if the primary attribute of interest (such as well data) is sparse, but there is an abundance of related secondary information (such as seismic data), it is

possible to study the covariance between two or more regionalized variables. Types of co-kriging can be summarized as follows:

Simple cokriging uses a related secondary 2D attribute to guide the interpolation of a primary attribute known only at control points (such as well locations). The mean is assumed to be a global constant. Ordinary cokriging is similar to Simple cokriging in that the mean is still assumed to be constant, but it is estimated using the neighborhood control points rather than specified globally. Collocated cokriging is a reduced form of cokriging, which requires knowledge of the correlation coefficient between the hard and soft data, and the variances of the two attributes. There is also a modified search criterion used in Collocated cokriging. This method uses all the primary data, but, in its simplest form, uses only one secondary data value, the value at the target grid node (Wackernagel, 2003 and Delfiner and Haas, 2005).

In this part, NPHI logs will be simulated using co-kriging and collocated co-kriging, and the results will be discussed afterwards. Same wells and variogram settings were used to estimate NPHI with acoustic impedance logs. First of all, AI logs were upscaled to model resolution. Figure 5.12 shows the histogram of the AI logs along with the upscaled values.

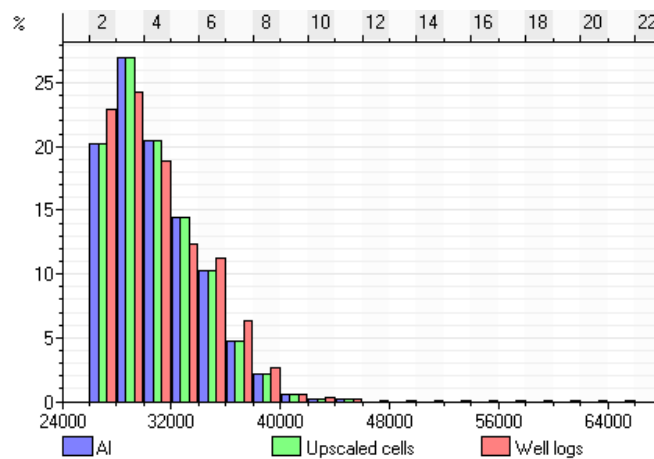


Figure 5.12 Histogram of the upscaled and original AI logs.

SGS algorithm was run with co-kriging option. Upscaled AI logs were chosen as a secondary attribute and output distribution was taken from the upscaled NPHI logs. For distribution of the second property (AI), Local Varying Mean (LVM) technique was used. LVM uses secondary data as local mean values for the primary

data. The mean varies at each location instead of being constant.

$$z(x_0) = \sum_i^n \lambda_i z(x_i) + \left[1 - \sum_i^n \lambda_i \right] m(x_0) \quad (5.2)$$

where; $z(x_i)$: data points, $m(x)$: secondary input with positive correlation value, λ_i : weights. The influence of LVM on the $z(x_0)$ value is inversely proportional to value of the weights. Secondary data should be available for all locations and have same units as the primary data (Schlumberger, 2009). The results of the co-kriging can be seen in Figure 5.13.

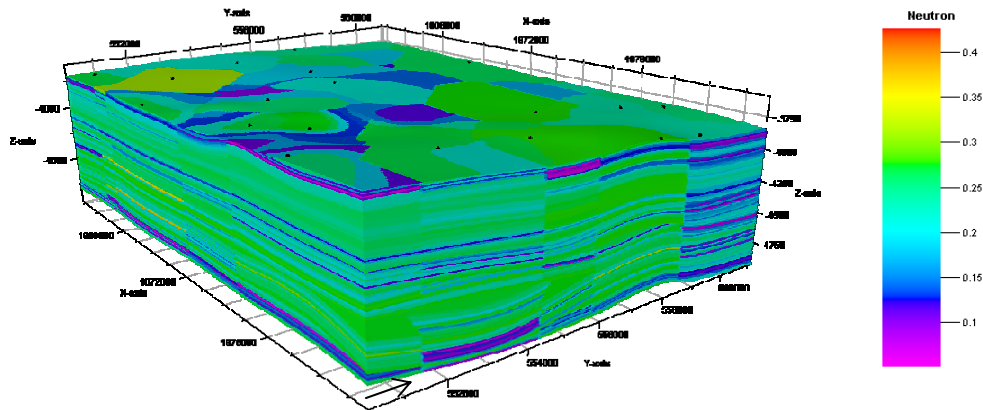


Figure 5.13 Result of the SGS with cokriging using NPHI as a primary and AI as a secondary data. LVM technique was used for distribution. Black dots on top of the model represent the upscaled well locations.

Effects of the LVM can easily be seen from the above figure. Varying mean across the model resulted in segmentations over the results. Therefore co-kriging simulation was repeated with the same parameters except the output distribution. Bivariate distribution was used from the previously simulated NPHI logs. The resulting simulation can be seen in Figure 5.14. This simulation result exhibits more geologically meaningful distribution. Comparison of both cokriging results can also be evaluated from their histograms in Figure 5.15. Distributed NPHI values with LVM exhibit very high values compared to those of from bivariate distribution.

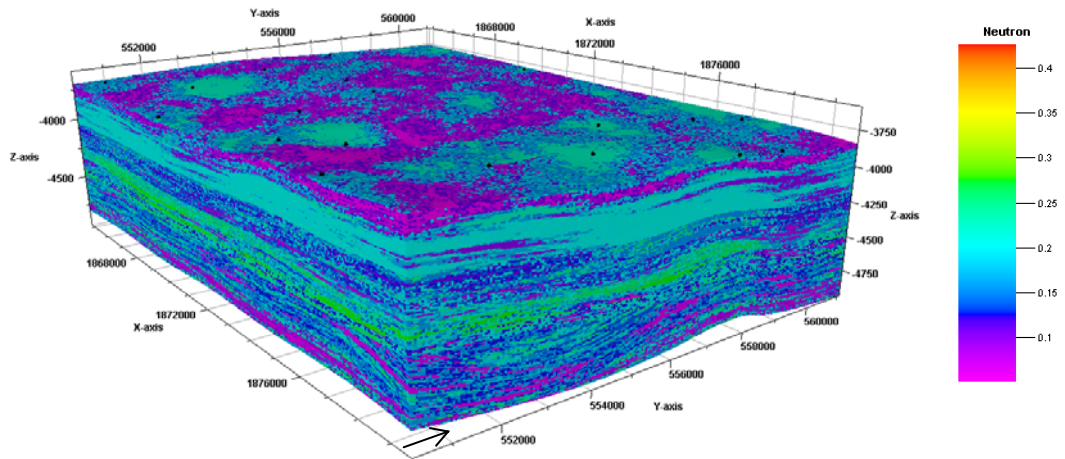


Figure 5.14 Cokriging SGS simulation results. NPHI used as a primary variable and the AI logs used as a secondary variable. Bivariate distribution was used to populate properties. Black dots on the top of the model represent the well locations used for upscaling.

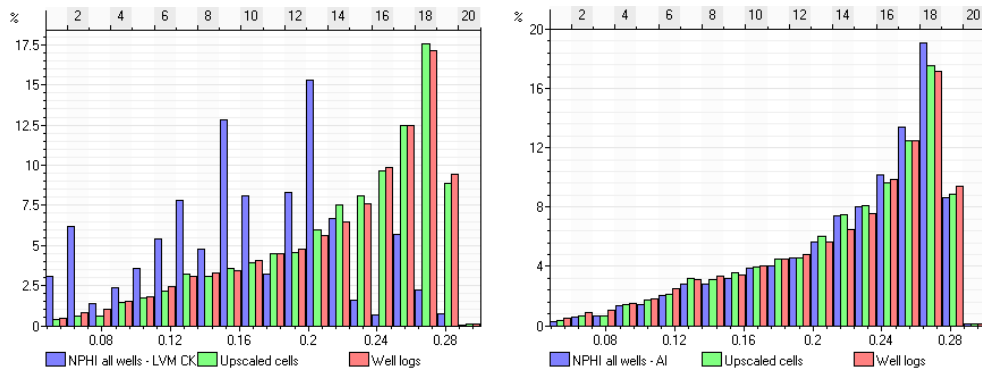


Figure 5.15 Histogram display of the cokriging results using LVM (on the left) and bivariate distribution (on the right).

Finally, NPHI estimation from SGS simulation using collocated cokriging technique was applied to data set. If the cokriging equation was recalled:

$$Z_{\text{cok}}(x_0) = \sum_i^n \lambda_i z(x_i) + \sum_j \mu_j Y(x_j) \quad (5.3)$$

This requires the primary, secondary, and cross variograms and considerably larger equation system to solve. On the other hand, collocated cokriging equation:

$$Z_{\text{cok}}(x_0) = \sum_i^n \lambda_i z(x_i) + \mu_j Y(x_0) \quad (5.4)$$

requires only primary variogram and uses correlation coefficient of secondary variable.

Same variogram parameters and wells were used to perform collocated cokriging for upscaled NPHI logs. AI logs, again, were used as a secondary variable. Correlation coefficient between these two variables is -0.88. Figure 5.16 shows the results of the simulations.

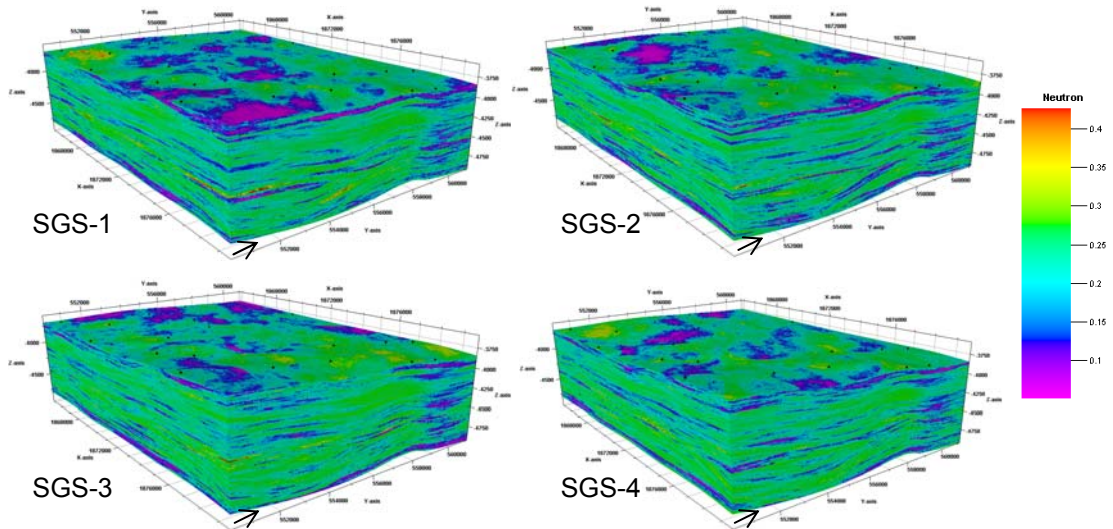


Figure 5.16 SGS collocated cokriging realizations. NPHI logs were used for primary and AI logs were used as a secondary property. Black dots at the tops surface represent upscaled well locations.

As it can be seen from the Figure 5.16, similar to SGS simulation results, each realization has different outcome than the others. This is basically the idea behind the algorithm, the cell visitation order to estimate the unknown values decided by the random seed number. Summary statistics of these runs can be seen in Table 5.4. Each realization has unique summation of total property values, whereas number of data points is the same. Another noticeable outcome from the statistics of the results is the minimum and maximum values of the upscaled and simulations. As the SGS algorithm implies, output distribution should be same with the input.

Table 5.4 Summary statistics for the SGS collocated cokriging results.

Name	Type	Min	Max	Delta	N	Mean	Std	Var	Sum
Upscaled	Cont.	0.05	0.43	0.38	2416	0.22	0.05	0.00	531.10
Well logs	Cont.	0.05	0.44	0.40	46170	0.22	0.06	0.00	10078.50
Property	Cont.	0.05	0.43	0.38	7161570	0.22	0.06	0.00	1570075.84
Property	Cont.	0.05	0.43	0.38	7161570	0.22	0.06	0.00	1570260.15
Property	Cont.	0.05	0.43	0.38	7161570	0.22	0.06	0.00	1568277.74
Property	Cont.	0.05	0.43	0.38	7161570	0.22	0.05	0.00	1587313.03

Final conclusion for the collocated cokriging realization will be drawn posting the original NPHI logs over the simulation results. Again, three wells (LO Fancher 1, B Yates 7, and Ashe C 1) were used for cross checking the results. Figure 5.17 shows the correlation between estimated and original NPHI logs.

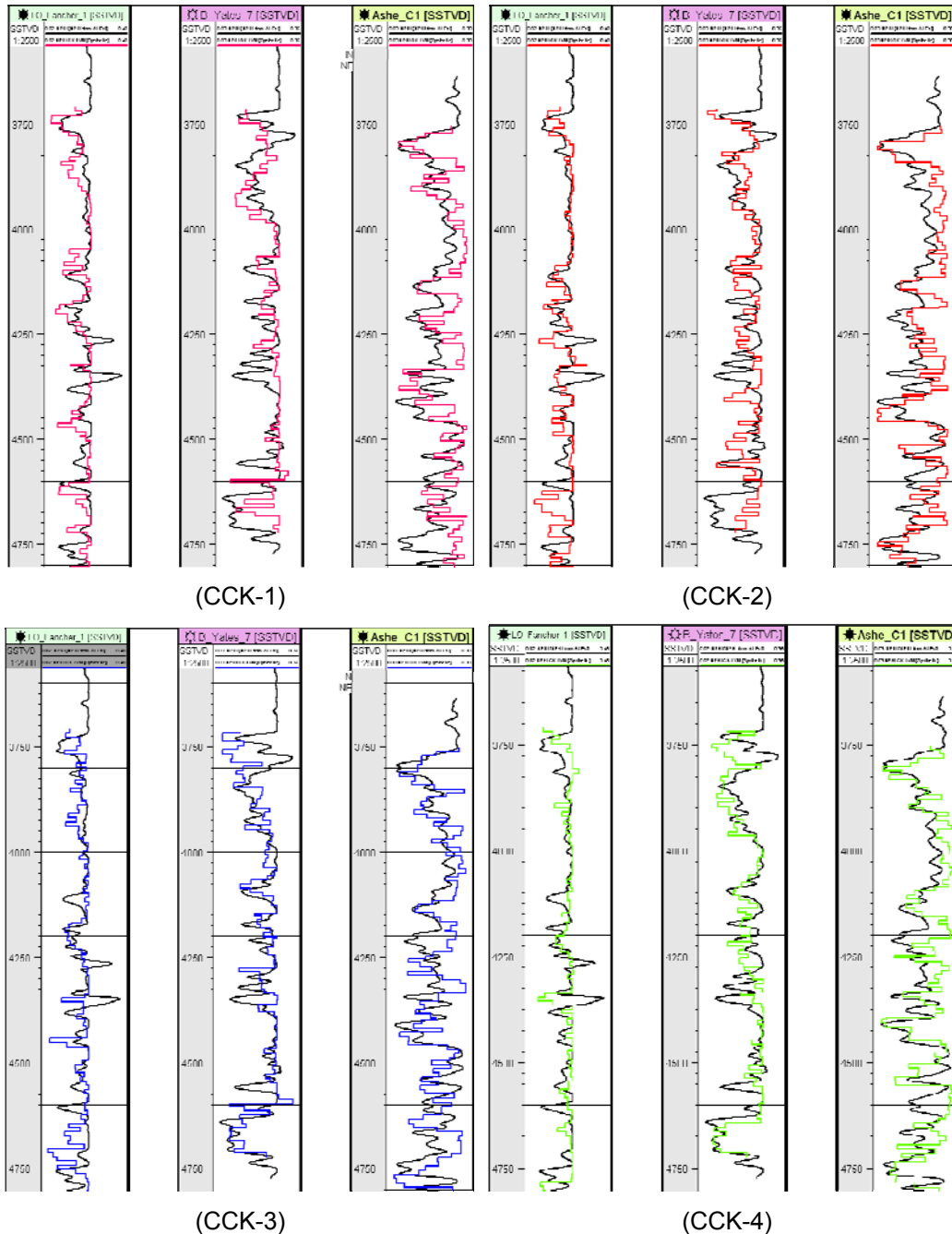


Figure 5.17 Comparison of original NPHI logs and collocated cokriging simulation results for the wells LO Fancher 1, B Yates 7, and Ashe C 1 respectively. Black curve shows original NPHI logs and pink, red, blue, and green curves show the results of the simulation.

In this section, NPHI logs were predicted using few simulation algorithms. NPHI logs are usually presented in “neutron porosity units” which is directly related to the formation’s hydrocarbon index and quantitatively, the water-filled pore spaces give a response to the neutron tool, therefore it measures the porosity.

Estimation procedure was applied to Atokan Interval in the study area which was bounded by MFS 90 and 20. The interval is mainly deposited in either delta or a marine basin margin (Hardage, 1996). Atoka interval contains sandstone and tight limestone with interbedded shale sequences. After the data were prepared and exploratory analysis was performed, four SGS were run to produce NPHI volume in the study area. As SGS produces the results by respecting the minimum and maximum input data values, all results were fallen into 0.005% and 0.43% NPHI interval. On the other hand, all realizations exhibited thin low-value NPHI layers across the area between thick high-value sonic porosity zones. These thin layers can be thought as a shale sequences between the sandstone and limestones.

Simulation was repeated using collocated cokriging algorithm to be able to incorporate secondary information as a guide to produce NPHI volume. The results of this run also fallen into same min-max NPHI interval as expected but comparing the Figures 5.9 and 5.16 showed that using seismic data as a secondary variable created more continuous and distinctive low-NPHI thin layers in the study area.

As a conclusion, using correlated secondary variable improved the results. The correlation coefficient of the original NPHI logs and the estimated NPHI logs from collocated cokriging is better than that of the SGS estimation with single variable. SGS only uses variogram models to populate the distance dependent relationship to areas where no well control is available. Therefore, results are mainly depending on the density of the data available (number of wells and logs) and the quality of the variogram model which is equal to quality of the relationship if it exists. On the other hand, including secondary information into simulation brings an add value to results. Final outcomes were proved that using seismically driven secondary information; it is possible to predict reservoir properties in the study area but still these results needs to be improved. In the next section, seismic attributes will be employed to estimate the reservoir properties.

5.3 NEURAL NETWORK APPROACH

In previous chapters, estimation of reservoir properties (data from well logs) was discussed and prediction examples were performed. The relationship were established between well log itself, namely, non-existent property was estimated using the existing data from well logs.

In this part, the idea of establishing a relationship between reservoir properties and seismic attributes at the well locations will be investigated. After this link is built, reservoir properties will be able to predict through the whole area of the seismic coverage. The relationship found can be linear (e.g. linear multi-regression analysis) or non-linear (ANNs).

Multi-layer feedforwarded neural network (MFNN) algorithm will be used mainly for the prediction of properties. Figure 6.18 shows the typical neural system for the network architecture.

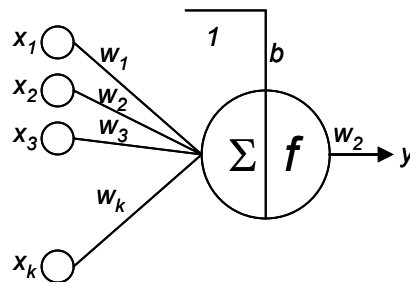


Figure 5.18 A typical neuron architecture for MFNN. ($y = f(\sum_{i=1}^{n-1} x_i w_i + w_n)$) (modified from Nikravesh et. al., 2001).

A typical network contains an input layer, an output layer, and at least one hidden layer. Each layer communicates with connections having weights (w). In this type of network, first, input signals (x) are multiplied by the corresponding weights (w), then the weighted input signals are summed, and finally, a non-linear activation function (f) is applied to sum outcome.

For each connection (pattern), the following equation can be written:

$$Z_i = x_1 w_1 + x_2 w_2 + \dots + x_n w_n + \theta_n \quad (5.5)$$

where x is input, w is connection weights, θ is bias, and z is output. Referred connections in Equation 5.5 can be written in matrix form Nikravesh et. al., (2001):

$$\begin{bmatrix} z^{(1)} \\ z^{(2)} \\ \cdot \\ \cdot \\ \cdot \\ z^{(P)} \end{bmatrix} = \begin{bmatrix} x_1^{(1)} & x_1^{(1)} & \dots & x_N^{(1)} & 1 \\ x_2^{(2)} & x_2^{(2)} & \dots & x_N^{(2)} & 1 \\ \cdot & \cdot & \dots & \cdot & \cdot \\ \cdot & \cdot & \dots & \cdot & \cdot \\ \cdot & \cdot & \dots & \cdot & \cdot \\ x_1^{(P)} & x_2^{(P)} & \dots & x_N^{(P)} & 1 \end{bmatrix} \begin{bmatrix} w_1 \\ w_2 \\ \cdot \\ \cdot \\ \cdot \\ w_N \end{bmatrix} + \theta \quad (5.6)$$

or it can be rewritten as:

$$z = X_1 * w_\theta = X * w + \theta \quad (5.7)$$

where; $w_\theta = [w^T \mid \theta]^T$ and $X_1 = [X \mid 1]$

1= column vector of ones with P rows;

X= PxN matrix with N input and P pattern

θ = bias vector, vector with P rows of θ and

w= weights, vector with N rows

*= Matrix multiplication

The activation function (f) determines the neuron output depending on its activity level. The most commonly used functions are sigmoid functions and they are range between 0 and 1. An example logistic function can be written as:

$$f(x) = \frac{1}{1 + e^{-x}} \quad (5.8)$$

and hyperbolic tangent function (another sigmoid function) having -1 to +1 can be expressed as:

$$f(x) = \tanh(x) = \frac{e^x - e^{-x}}{e^x + e^{-x}} \quad (5.9)$$

The estimation weights are done during the training phase of the network. During training a model is built using the input data provided. The input data in this phase should be the part of and representative of the whole input data set. Comparison of the network outputs with the desired outputs can be performed and error can be written in a square sum fashion:

$$e_k = \frac{1}{2} \sum_{i=1}^p (y_i - d_i)^2 \quad (5.10)$$

where y is the network output and d is the desired outcome. The purpose at this point is minimizing the error. This can be done by updating the weights and during training the error can become smaller. In the theory, this error can become zero with enough number of neurons and iterations. On the other hand, this can bring the

effect of random noise and specific trends from the data. This problem is called overtraining or memorizing. That is why the data is separated into training and validation. The training data is used to train the network and validation set is used to check the performance of the network. During training, hidden neurons are added one at a time and stopped when the best correlation is obtained. Resulting non-linear model now can be used to predict the properties within the whole area. More details regarding the ANNs can be found in Chapter 2.

The first step before building the network is the preparation of the input data. This step is very important to obtain the best performance from the ANN. As it was stated in previous sections, 25 seismic volume attributes were extracted from the seismic data. Instead of using all attributes, a selective method was used to eliminate the attributes having similar responses. Figure 5.19 shows the extracted seismic attributes along the B Yates 18D well. This analysis suggests that some of the attributes need not to be involved into ANN study as they have similar signatures. Attribute naming convention will be turned to numbers track them easily.

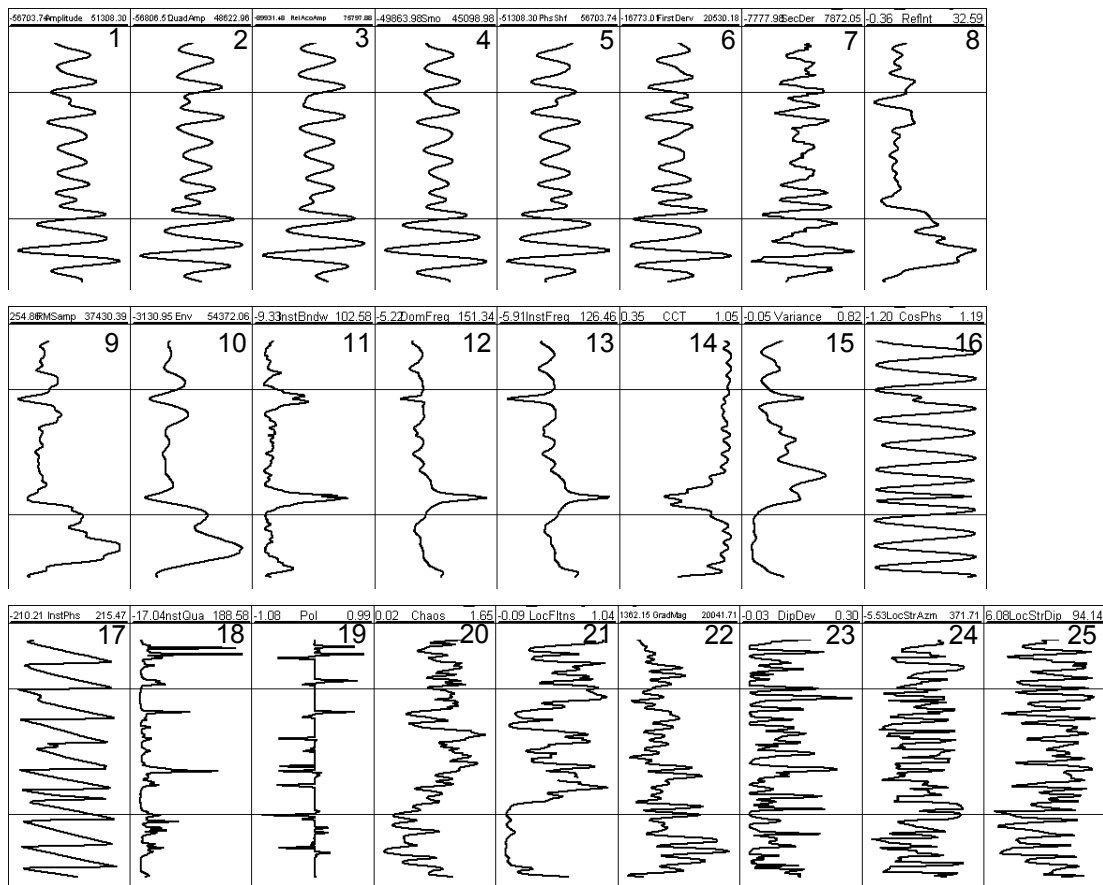


Figure 5.19 Enlarged display of the seismic attributes extracted along the B Yates 18D well. Please refer to Table 6.1 for the attribute names.

Attribute elimination is also useful for data dimension reduction which will require less computing time. Attributes 1, 2, 3, 5, and 6 were removed as they have similar response with the attributes 4 and 7. Attributes 9, 10 and 12 were also removed from the list. Attributes 16 to 19 are represent specific responses and they were not able to provide a correlation with the other information, therefore they were eliminated too. As a result, 12 seismic attributes were involved into ANN study. Please note that, vertical extension of the seismic attributes in Figure 5.19 does not represent the whole seismic vertical interval.

These 12 attributes were extracted along the borehole paths using the time-depth relationship built in Chapter 3.5. Vertical limits of the attributes were kept between the interpreted horizons (MFS90 and MFS20). Because, each attribute has its own value limits, all attributes were scaled to -1 to +1. As the attributes are definable at each point where well logs exist, upscaling of the log were not performed, smoothing operator was applied to wells as the attributes have larger sampling intervals then those of the well logs. This scaling was also applied to properties to be predicted. In this part, to be able to make the comparison with the other estimation techniques applied in previous chapters, NPHI property will be estimated based only on seismic attributes.

Completing the data preparation in matrix format, basic statistical analyses were applied. Following results were based on well B Yates 18 D for demonstrative purposes. Regression analysis (Figure 5.20) basically shows the visual trends between two properties if it exists and the outliers (extreme values) can be observed and eliminated from the data. Frequency distribution is also very helpful for visualizing

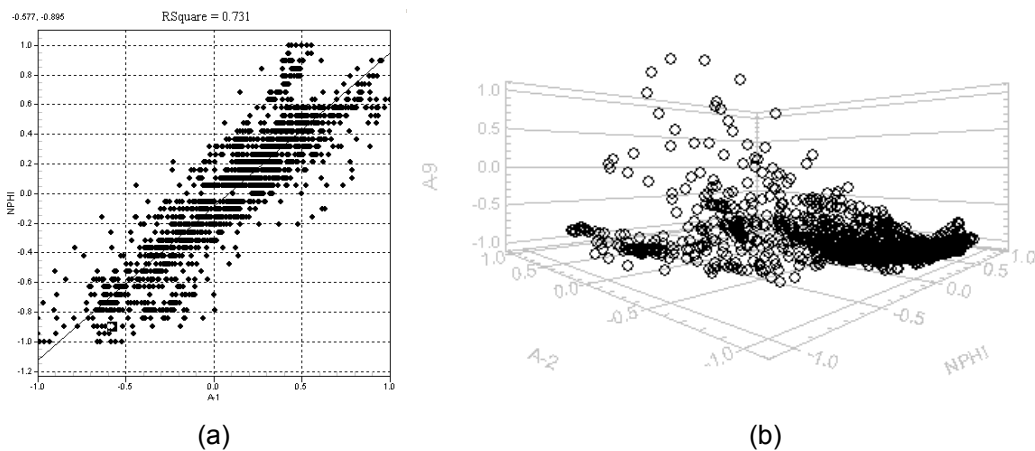


Figure 5.20 Linear regression plot and 3D cross plot for the well B Yates 18D. (a) NPHI versus A-1 attribute and (b) NPHI versus A-2 and A-9 attributes.

the value trends in the data. These analyses were performed on the attribute data set versus NPHI values. Figure 5.20 shows an example of regression analysis.

In previous paragraphs, number of attributes was reduced to 12 to overcome data dimensionality problem. In this part, irrelevant attributes among these 12 attributes will be taken out from the data. This will be done based on Fuzzy Pattern Recognition (FPR).

Fuzzy logic is simply a tool for overcoming the difficulties that classical logic cannot handle. Classical logic proposes “A thing either is or is not” statement giving the true or false description where no definition can be possible between. Fuzzy logic, in this point, offers a solution of partial truth. In fuzzy logic belonging to a set or category is not important in the meaning of absoluteness, the degree of belonging is important instead (Aminzadeh and de Groot, 2006). Table 5.5 shows the differences between classical and fuzzy logic.

Table 5.5 Classical and fuzzy logic comparison (Aminzadeh and de Groot, 2006).

	Classical Logic	Fuzzy Logic
Membership	An element either belongs To set or not	An element belongs to a set to a degree
Degree of membership	$\mu(x) = \{0,1\}$	$\mu(x) = [0,1]$
Binary vs fuzzy unit	Bit (0 or 1)	Fit (a number between 0 and 1)
Boundaries	Sharp	Fuzzy
Overlapping sets	An element cannot belong to two non overlapping sets	An element can belong to two sets having fuzzy boundaries
Law of contradiction	$A \cap \bar{A} = \emptyset$	$A \cap \bar{A} \neq \emptyset$
Excluded middle	$A \cup \bar{A} = 1$	$A \cup \bar{A} \neq 1$

FPR is based on a logic that as each input parameter impacts the output to a certain degree. On the other hand, it may be affected by other parameters in the process. For non-linear, complex, and dynamic problems interaction between the input parameters must also be taken into account. In other words, the effect of each parameter on the output can be more or less (in a non-linear fashion) by the existence of other parameters. Therefore, effect of each parameter on to other

parameters which produces the results should be analyzed (Intelligent Solutions Inc., 2008).

Figure 5.21 shows the result of this analysis as a tornado plot. From the figure, it is clear that the attributes 1, 3, and 2 have degree of influence higher than 47%. Therefore, from this point, the other attributes will not be included in the estimation process. The most influential attribute is ranked number 1 and is normalized to 100% for its contribution to output. The other attributes were normalized against 1st ranked attribute. Therefore, 100% influence does not mean that attribute A-1 has a 100% percent influence to output.

Rank	Feature	% Degree of Influence
1	A-1	100
2	A-3	93
3	A-2	47
4	A-6	43
5	A-8	29
6	A-11	25
7	A-9	23
8	A-10	15
9	A-7	15
10	A-4	15
11	A-5	9
12	A-12	1

Figure 5.21 Degree of influences of each attribute against each other.

This analysis can be done cross plotting each attribute against output (NPHI) and identifying the data points which have an influence on the output. Figure 5.22 shows results of this analysis. The blue circles represent the original data and the red dots in the plot the data were selected for the inspection analysis. In Figure 5.22 (a), entire data points were divided into 25 segments along X and Y axes which produced 25x25 bins. In this case, 17% of the data were selected as a representative of the entire data set (red dots). In Figure 5.22 (b), 50 segments were produced and selection percentage became 24. In both plots, X and Y axes range from -1 to 1. Selection of the points was also done using the fuzzy pattern recognition and the most representative data points were selected in both cases. The main idea behind this analysis is that selecting the most important points and reducing the data density to provide quick inspection for the sensitivity analysis (Intelligent Solutions Inc., 2008).

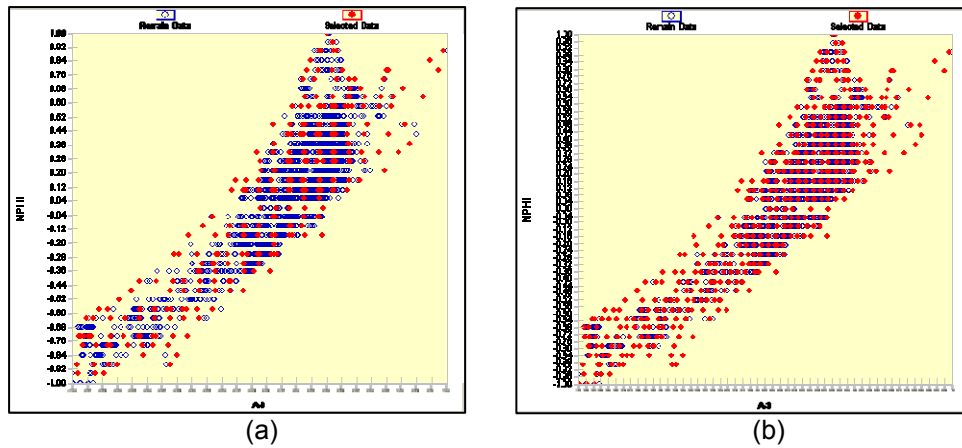


Figure 5.22 Data contribution cross-plot (NPHI versus A-3) for quick inspection. The red dots are selected data and the blue dots are remaining data. (a) Number of segments is 25 and selection is 17% and (b) number of segments are 50 and selection percentage is 24. Both X and Y axis range from -1 to 1.

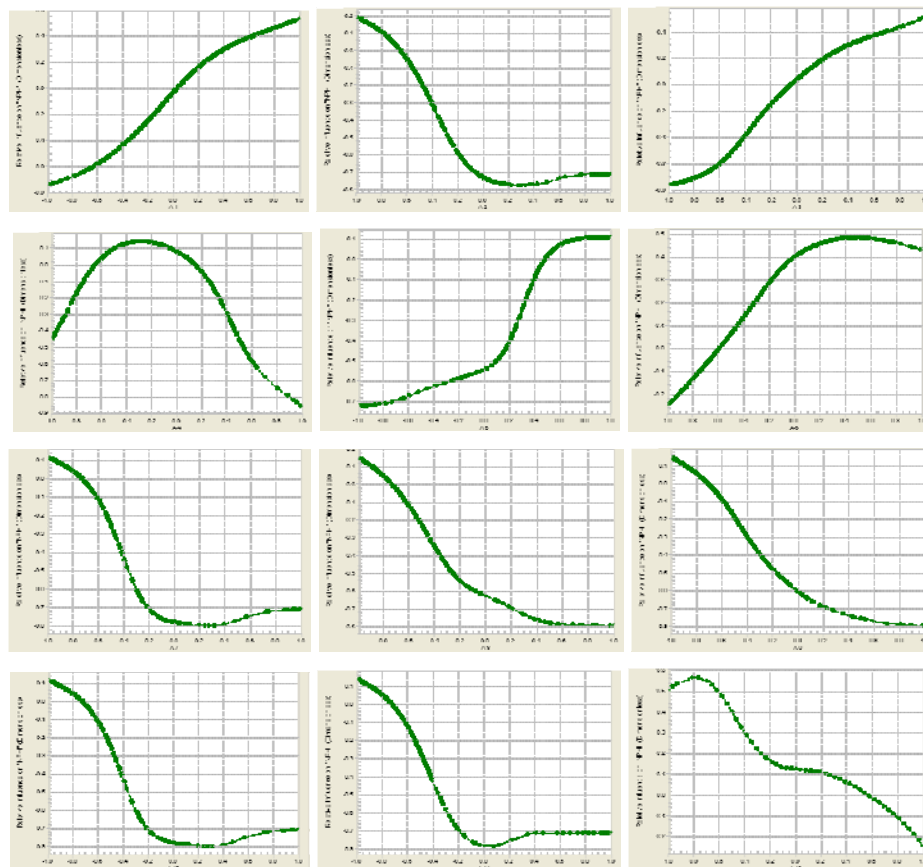
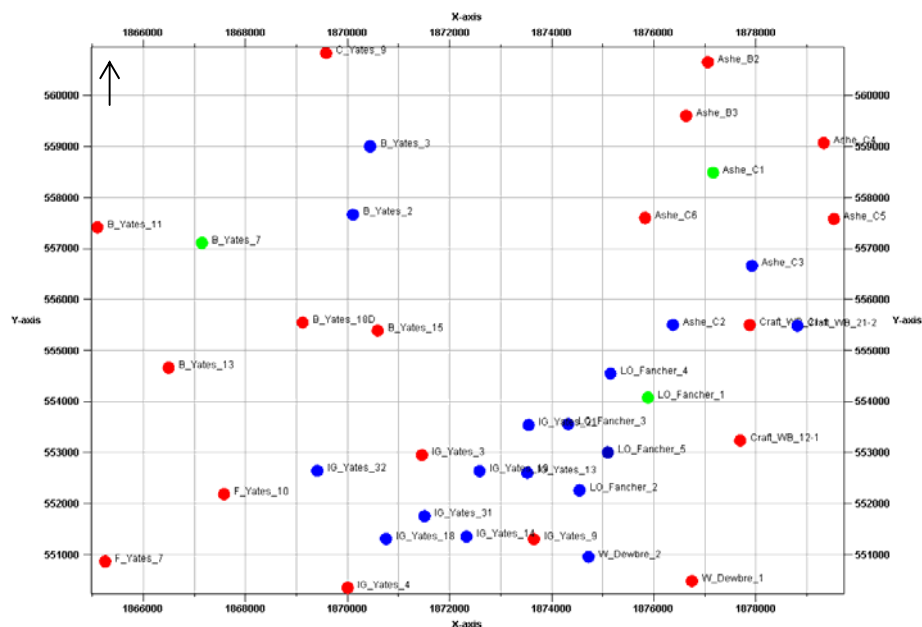


Figure 5.23 Sensitivity analysis for the seismic attributes versus property to be estimated (NPHI). Y-axis is relative influence (dimensionless) and the X-axis is attributes scaled from -1 to 1.

Figure 5.23 represents another technique to analyze the contribution of each attribute to the estimation results to be performed. In these graphs, high values with positive slope represent the strong positive correlation and low values with negative slope show that parameters have dominantly opposite effect (negative correlation) on the output. Steepness of the lines also exhibits the degree of influence of the input over the predicted output. In Figure 5.23, attributes 1, 3 and 6 show positive high influence for the prediction of the NPHI property. Successful application of this analysis requires division of the input data set (attributes) based on the regions indicated by slopes in the sensitivity graphs. In this study, only the degree of influence computed by fuzzy pattern recognition will be used.

After completing the statistical analysis on the data set and eliminating the irrelevant data, we can start to prepare the input data for the neural network analysis. In the study area, there are 38 wells available. Among them, extracted attributes of 18 wells used as input (with red symbols), 3 wells (with green symbols) were chosen to check the validity of the relationship to be established by the network, and 17 wells (with blue symbols) were not included. Figure 5.24 shows the distribution of the wells used for neural network study. The criteria for selecting the wells for training was the representative of the whole are. Wells with blue symbols were not chosen, because the wells chosen for the training were already distributed



in the study area evenly and selecting wells close to each other will increase the computation time and will not bring too much additional information as the seismic signature of the area represent almost horizontal layers parallel to each other (see Chapter 3.4 for more details).

The wells LO Fancher 1, B Yates 7, and Ashe C 1 were selected for testing the results to be able to make a comparison with the results obtained from the geostatistical techniques.

In the data preparation part, three seismic attributes were selected, A-1, -2 and -3. Because the resolution difference between the well logs and seismic data, high frequency content is provided selecting Acoustic Impedance (AI) attribute as a one of the inputs. Please note that, AI curves were estimated for all well locations in Chapter 5. Selecting the input and output data is followed by classification of the data into training, calibration, and verification sets. 20% of the input data is selected as a calibration and another 20% was assigned for verification. The selection of the sets was done randomly. As a result, 15,994 points for training, 5,331 points for calibration and verification were classified. All data is referenced from the sub sea to be able to represent the same depth level.

Prepared data were fed into the Back Propagation Network (BPN) algorithm. The summary of the method was provided in the beginning of this section. Please refer to References section for more detailed information. In Figure 5.25, the designed network can be seen. After several runs, optimized parameters are found between input-hidden layer and hidden-output layer as:

- Learning rate: 0.3
- Weight decay: 0.2

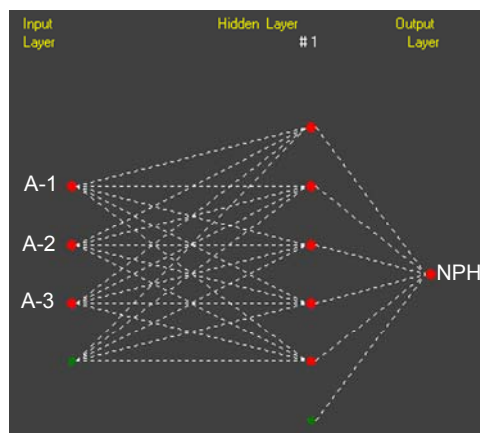


Figure 5.25 Error Back Propagation network built to estimate NPHI property from seismic attributes.

For the activation function, tangent hyperbolic function was used; stopping condition is set to minimum error calibration. Only one hidden layer was used with five neurons. Input layers were represented by three seismic attributes plus well identifier. Hidden layer contains 5 neurons and output layer gets information from a well identifier. Figure 5.26, 5.27 and 5.28 shows the results for this network.

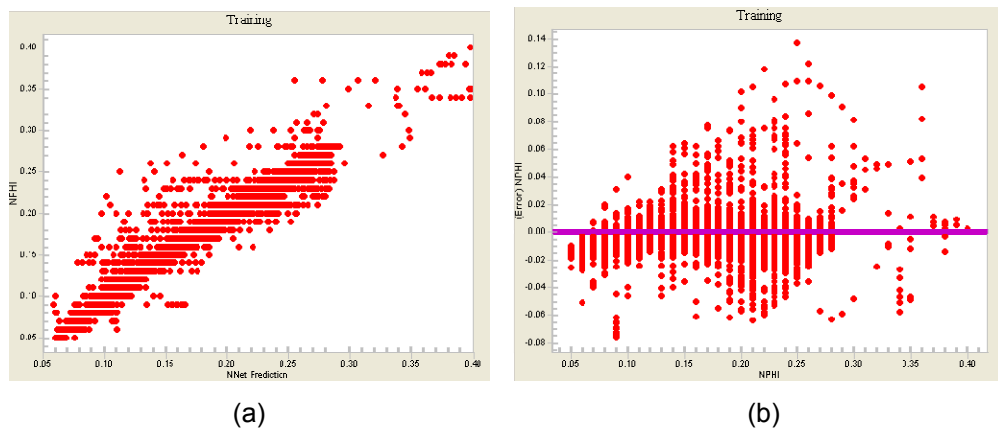


Figure 5.26 BPN algorithm training results for the NPHI estimation. (a) Actual NPHI values versus network prediction and (b) error plot for the estimation results. Magenta line represents zero error line.

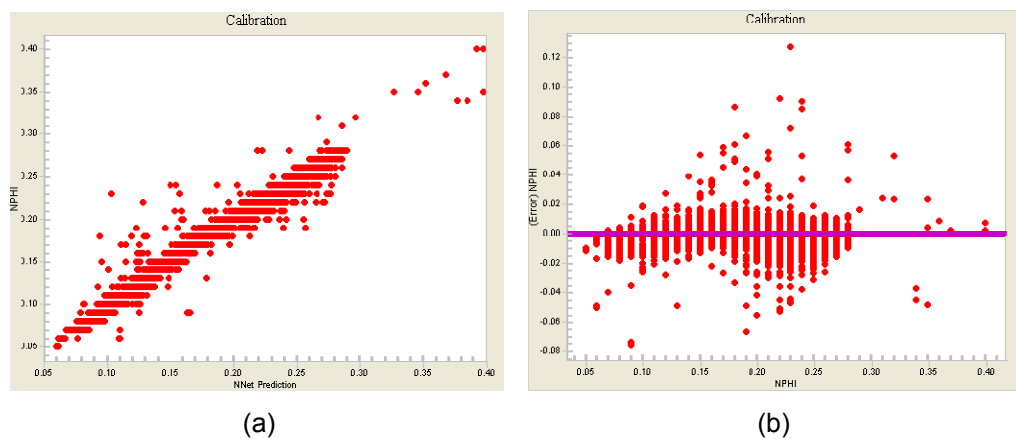


Figure 5.27 BPN algorithm calibration results for the NPHI estimation. (a) Actual NPHI values versus network prediction and (b) error plot for the calibration results. Magenta line represents zero error line.

Training results showed very good fits with 0.865 R^2 value and 0.883 correlation coefficient (CC). Calibration results have 0.873 R^2 value and 0.887 CC, and verification results showed 0.863 R^2 value and 0.882 CC. These results showed

that the high performance of the BPN algorithm for finding out non-linear relationships between data points.

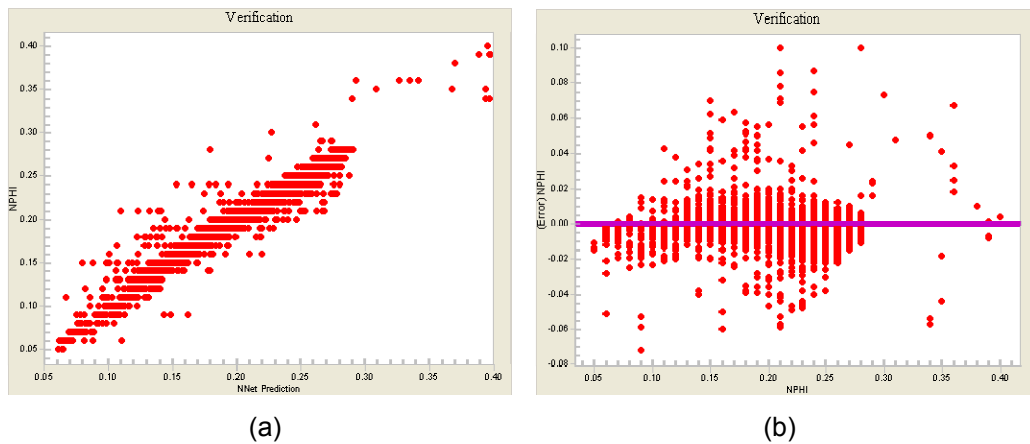


Figure 5.28 BPN algorithm verification results for the NPHI estimation. (a) Actual NPHI values versus network prediction and (b) error plot for the verification results. Magenta line represents zero error line.

Now the performance of the BPN network can be tested applying the relationship extracted to 3 wells left outside the network training. As it can be seen in Figure 5.29, correlation is high between the predicted and actual NPHI logs except some peak regions.

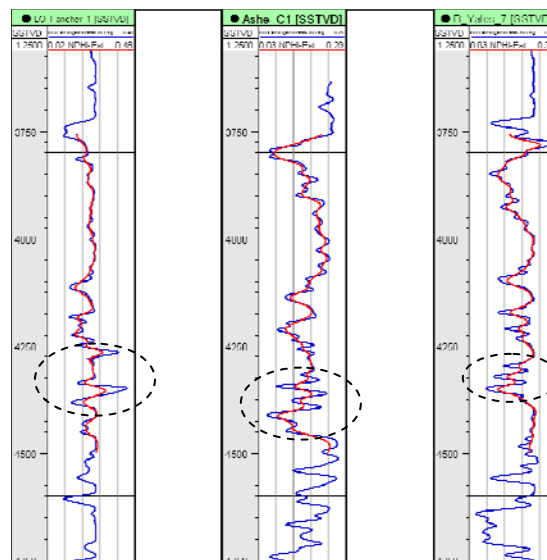


Figure 5.29 BPN validation results on wells LO Fancher 1, Ashe C1, and B Yates 7. Actual NPHI logs are in blue line and predicted logs in red line color. Note that on mismatch on the areas where peak values exist.

There are some important points that should be indicated on this high performance of the network prediction. First of all, not all NPHI logs from top to bottom were considered during training. It was limited to approximately 750 ft interval and as it can be observed from the Figure 5.29, the interval chosen for training and prediction correspond to smooth transition between NPHI values. Especially in the areas where some peaks are observed in the original NPHI logs (dotted circles in the Figure 5.29), the quality of the prediction gets lower. Incorporating previously estimated acoustic impedance attribute also improved the results as it is directly related to estimated log property. Previously smoothed actual NPHI logs should be considered as another factor on predicted results. Another important factor on the results will be the selection of the most correlated seismic attributes as input parameters to the network. Prediction results are, naturally, smoother than the actual logs due to fact that resolution difference between the seismic attributes and well logs. Considering these factors explained, BPN still created better estimation than the geostatistically driven prediction results. Correlation analysis for the actual and predicted NPHI property showed 0.89, 0.93, and 0.94 for wells LO Fancher 1, Ashe C1, and B Yates 7 respectively.

For the BPN network algorithm, “batch” method was used. In this method the network examines all the data in the training set and calculate the average error for the entire data set before it backpropogates the average error to modify the weights. If this method was not used, the modification of the weights was done based on the training data set in a random order.

General Regression Neural Network (GRNN) algorithm was also used to test different network over the estimation results. Basic difference of GRNN methods from the BPN is that the weights between hidden and output layers are the target values. As a result, the output is a weighted average of the target values. It does not use the steepest descent method for error minimization. The main drawback with the GRNN methods is that GRNN cannot ignore the irrelevant inputs due to dimensionality problem. Therefore, it is suggested to employ this network algorithm if the number of inputs is more than 5 or 6 (Intelligent Solutions Inc., 2008). For more detailed information about the theory, please refer to paper written by Specht (1991).

GRRN is performed on the same data set using the “hold out” methodology. During this method, each time one case is left out from the network and process is repeated until all the cases were removed and put back into the network. In our

case, GRNN was applied only to training data set, therefore the network was not used any calibration or verification sets. Calibration was performed only using the training outputs.

Figures 5.30 to 5.32 shows the results of GRNN run on the same training data set. The estimation results obtained show lower correlation when compared to prediction resulted in BPN network due to reasons explained above paragraphs. The R^2 value and CC for the training set was 0.658 and 0.823 respectively. For the calibration, R^2 : 0.667 and CC: 0.830, and verification set represented 0.643 R^2 and 0.818 CC values.

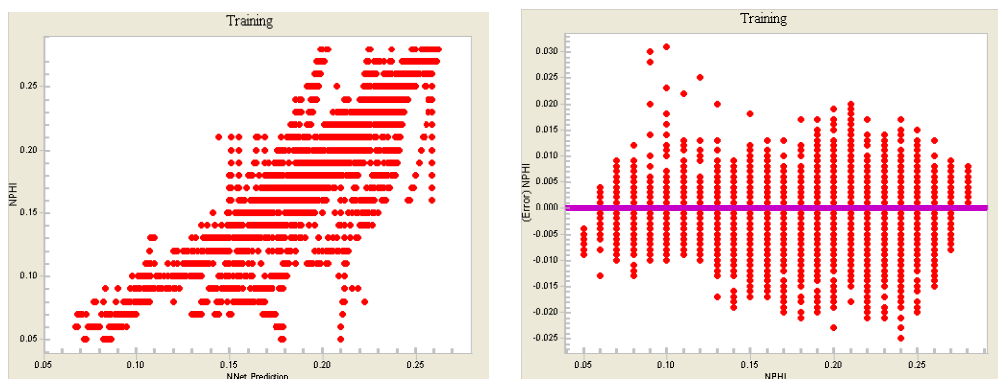


Figure 5.30 GRNN algorithm training results for the NPHI estimation. (a) Actual NPHI values versus network prediction and (b) error plot for the estimation results. Magenta line represents zero error line.

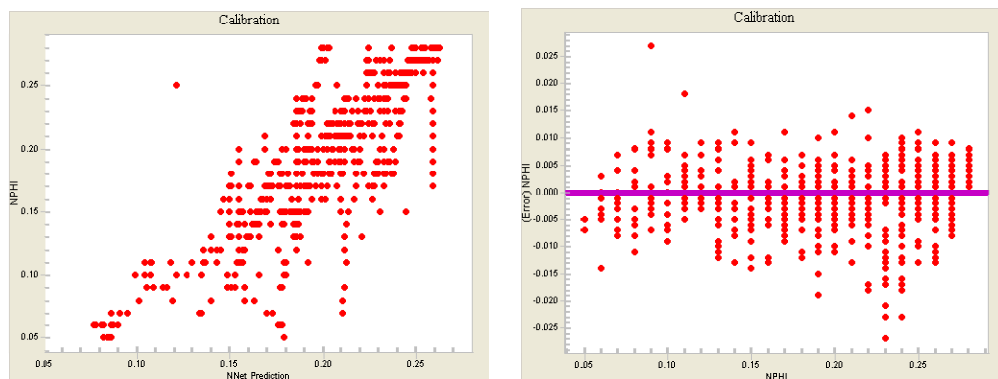


Figure 5.31 GRNN algorithm calibration results for the NPHI estimation. (a) Actual NPHI values versus network prediction and (b) error plot for the calibration results. Magenta line represents zero error line.

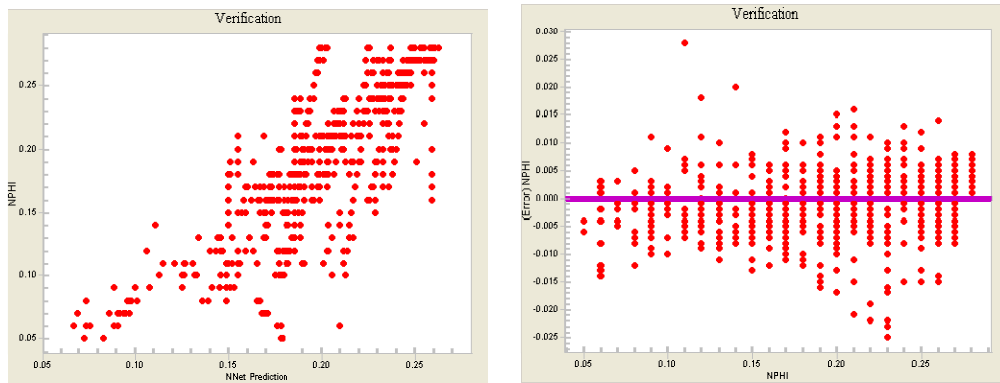


Figure 5.32 GRNN algorithm verification results for the NPHI estimation. (a) Actual NPHI values versus network prediction and (b) error plot for the calibration results. Magenta line represents zero error line.

The performance of the GRNN network can be tested applying the relationship extracted to 3 wells left outside the network training. As it can be seen in Figure 5.33, correlation is lower the predicted and actual NPHI logs except some peak regions.

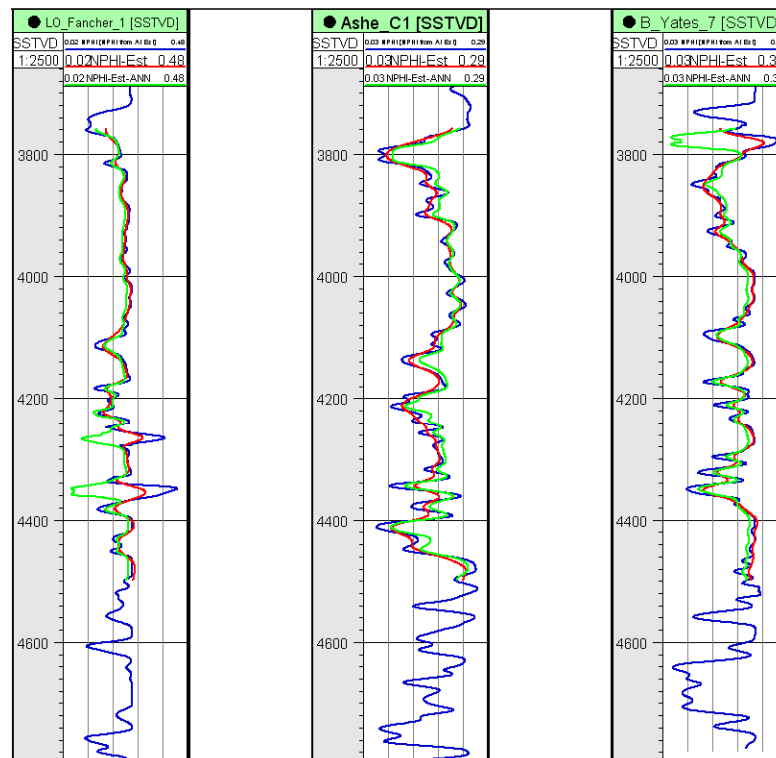


Figure 5.33 GRNN validation results on wells LO Fancher 1, Ashe C1, and B Yates 7. Actual NPHI logs are in blue line and predicted logs in green line color. Red color curve represents the estimation results form the BPN algorithm.

Comparison of the correlation results of both BPN and GRNN algorithms showed that BPN provided slightly better NPHI prediction results than those of the GRNN. The main reason for the low performance is believed to be the fact that GRNN does not use calibration and verification sets.

As it can be seen in Figure 5.33, BPN lower estimated the NPHI values at the high porous zones. GRNN, on the other hand, produced mostly inaccurate results in the same zones. Because during the prediction study seismic attributes and AI logs were used, they may not contain enough physical information where porous zones are located. The results can also be affected by the possible fluid fill inside the pores. Training, calibration and verification error ranges for the BPN are vary between -0.08 and 0.13 in average. GRNN error results fallen between -0.025 and 0.027.

CHAPTER 6

DISCUSSION

In this study, geostatistical and artificial neural network techniques were applied to predict reservoir properties in the study area. The final outcome is pointing out the existing relationship between various well logs and how ANN techniques are capable of predicting them with and without using seismic data.

One of the major problems in reservoir characterization studies is integrating different types of data having various scales, for instance, seismic and well log data. Vertical resolution of the well logs was coarsened using upscaling process. It is obvious that the loss of information during this process which cannot be incorporated to the estimation processes. On the other hand, applying this procedure is inevitable due to fact that all information need to be consistent.

Preparing the existing data to build the structural model of the reservoir is another important step. As most of the information was supplied by 3D seismic data, eventually there is need for converting time dependent data into depth using appropriate velocity function and/or model. In this study, 3 wells were used to extract the velocity information and then time depth relationship at the formation tops were used to populate velocity field to whole area. Depth conversion using this methodology, obviously contain some artefacts. The most important drawback is the error associated with the interpretation of the horizons. Predicting the velocities using information from limited number wells can also lead to some inaccuracy. Geostatistical depth conversion methods may provide more suitable results as they can use the spatial distribution of the given information.

Estimation of the acoustic impedance was performed first based on the existing density sonic relationships. In the study area, there are only 3 wells having this information. Therefore, sonic logs were predicted using ANN techniques, mainly form RILD logs, and then AI property was estimation in the area. As a result, error associated with ANN estimation was added to resulting AI prediction. Seismic inversion techniques can provide better estimation of the AI property as they relate the seismic information directly with in the whole field.

Finally, sonic porosity property was estimated using BPN and GRNN algorithms. During this study, seismic attributes were used as an input for the network algorithms along with the AI property. Attributes were extracted along the

boreholes as a single trace and then scaled. As a result, single traces carry an information for a very limited areal extent. Extracting several traces in the vicinity of the borehole can present more meaningful information as the reflectivity already contains some information from the neighbourhood areas around the borehole.

Neural network prediction was performed first using BPN to estimate NPHI property. Using appropriate parameters was produced very good estimation results. GRNN algorithm prediction was not satisfying. During network runs, a single hidden layer was used. Even though, it is stated that using a single hidden layer can solve most of the non-linear problems, applying more hidden layers can improve the results.

CHAPTER 7

CONCLUSIONS

In this study, reservoir parameters, in particular NPHI, were predicted using existing other logs and seismic attributes. Geostatistical simulation algorithms and artificial neural network techniques were used for property estimation. The major results of this estimation study in the Boonsville Field, Forth Worth Basin can be summarized as follows:

Estimation of missing logs using empirical relationships showed linear dependency of the equations used. Two cases were examined: DT estimation with Fault's relationship and RHOB estimation using Gardner's equation. Both methods resulted in very low correlations: for density the highest CC found in well B Yates 9 as a 0.60 and the lowest CC obtained for well B Yates 11 as a 0.44. Faust's approach produced better sonic estimation. For the same wells, approximately >0.80 CC was obtained. As a result, empirical relationship cannot be generalized to the whole field due to their linear dependency to the proposed equation system. In contrary, subsurface usually characterized by heterogeneities and they cannot be represented with linear equation systems.

Prediction of the missing log sets were performed using ANN methods. For the B Yates 18 D well, the most correlated logs against DT were found as NPHI, RHOB, and RILD. Estimation of DT using RILD log was resulted in 0.79, 0.91, and 0.85 CC for the wells Ashe C 5, B Yates 11, and C Yates 9 respectively. These results showed that in the study area, DT logs can be estimated using existing RILD logs with ANN methods considering the careful selection of the optimum network parameters. Incorporating more than one well log into the training phase slightly lowered the estimation results for the B Yates 18 D well but exhibited better areal distribution.

GR log found to be the most correlated log with NPHI and it was used to predict missing NPHI logs in the study area. The results showed high prediction accuracy (>0.86 CC). NPHI estimation using RILD and GR slightly reduced the estimation correlation but applying PCA removed the irrelevant data and reduced the data dimension resulting in enhancement in the prediction accuracy.

At the end, it was concluded that DT and NPHI logs can be predicted accurately in the study area using other correlated logs with ANN methods.

Acoustic impedance is another important parameters to be estimated in the study area as it can be directly related to the physical rock properties. Because AI is the product of the density and velocity, it was calculated directly only for wells B Yates 11, C Yates 9, and B Yates 18 D. To estimate AI for the rest of the wells in the study area, DT versus AI and RILD correlations were checked and 0.91-0.90, 0.88-0.88, and 0.85-0.89 CC were found. ANN prediction study for the DT estimation using AI and RILD resulted in 0.95, 0.93, and 0.95 CC for the same wells. These outcomes proved that AI logs can be estimated with high accuracy in the study area.

Two simulation algorithms were used to predict the NPHI property; SGS and SGS with collocated cokriging. SGS results were mainly respecting the minimum and maximum NPHI values at the estimated well locations LO Fancher 1, B Yates 7, and Ashe C 1. Because SGS only uses variogram models to populate spatial relationship to areas where no well control is available, the results are mainly dependent on the density of the data available and the quality of the variogram model which is directly dependent on the quality of the relationship if it exists. Seismically driven results for the NPHI estimation using collocated cokriging algorithm showed improved results but within the limitations of the SGS algorithm. As a result, both SGS and collocated cokriging estimations produced meaningful NPHI values at the well locations but prediction away from wells needs to be carefully handled by producing enough number of simulations to be able to point out the best representative realization.

Finally, the NPHI prediction was performed using BPN and GRNN methods. 25 seismic attributes were extracted along the well bores and most correlated attributes were selected using sensitivity analysis. It was observed that, using fuzzy logic to find the degree of influence of the each input against each other fastened the process and lowered the data dimension. After several runs, the best network parameters were selected and 3 attributes were fed into BPN network to estimate NPHI property. Results showed good correlation for the wells LO Fancher 1, Ashe C1, and B Yates 7. Less accurate intervals were observed as immediate peaks exist in the NPHI log. These less accurate estimations of the BPN network suggested that these intervals can correspond to major lithological and/or rock physical changes (e.g. fluid fill in porous zones). GRNN technique was also used to predict the NPHI property in the study area. Results showed slightly lower correlation than those of the BPN runs. As a conclusion, both ANN methods provided a good prediction results as they are able to find out and apply the existing non linear relationship in the given data set.

REFERENCES

- Akin, S., C. M. Ross, and A. R. Kavscek, 2008, Combination of well log and pore-scale data to predict petrophysical properties of diatomite, *Journal of Petroleum Science and Engineering*, v. 60, p. 133-149
- Aminzadeh, F. and P. de Groot, P., 2006, *Neural networks and other soft computing techniques with application in the oil industry*, EAGE Publications, 161 p.
- Aminzadeh, F., 2005, Applications of AI and soft computing for challenging problems in the oil industry, *Journal of Petroleum Science and Engineering*, v.47, p. 5-14
- Armstrong, M., 1998, *Basic linear geostatistics*, Springer-Verlag, 153 p.
- Arzuman, S., 2009, Application of Petrel neural network tools to estimate well logs, Extended abstract, 17th International Petroleum and Natural Gas Congress and Exhibition of Turkey, Proceedings, p. 40-43.
- Bacon, M., R. Simm, and T. Redshaw, 2003, *3-D seismic interpretation*, Cambridge University Press, The United Kingdom, 213 p.
- Barclay, F., A. Bruun, K. B. Rasmussen, J. C. Alfaro, A. Cooke, R. Godfrey, D. Lowden, S. McHugo, H. Ozdemir, S. Pickering, F. G. Pineda, J. Herwanger, S. Volterrani, A. Murineddu, A. Rasmussen, and R. Roberts, 2008, Seismic inversion: Reading between the lines, *Oilfield Review*, v. 20, n. 1, p. 42-63
- Bongarcon, D. F., 2004, Theory of sampling and geostatistics: an intimate link, *Chemometrics and Intelligent Laboratory Systems*, v. 74, p. 143-148
- Boschetti, F., M. C. Dentithz, and R. D. List, 1996, Inversion of seismic refraction data using genetic algorithms, *Geophysics*, v. 61, n. 6, p. 1715-1727
- Boyer, S., and J. L. Mari, *Seismic Surveying and Well Logging*, 1997, French Institute of Petroleum (IFP), Editions Technip, 192 p.
- Brown, A., R., 2001, Understanding seismic attributes, *Geophysics*, v. 66, n. 1, p. 47-48

Caers, J., 2000, Direct sequential indicator simulation, Proceedings of the 6th International Geostatistics Congress, in Kleingeld, W. and Krige, D., eds., Cape Town, South Africa, 12 p.

Carr, D. L., R. Y. Elphick, L. S. Foulk, High-Resolution Reservoir Characterization of Midcontinent Sandstones Using Wireline Resistivity Imaging, Boonsville (Bend Conglomerate) Gas Field, Fort Worth Basin, Texas, AAPG Annual Convention, San Diego, v. 80, n. 13, p. 23

Carr, D. L., R. Y. Elphick, R. A. Johns, and L. S. Foulk, 1997, High-resolution reservoir characterization of Midcontinent sandstones using wireline resistivity imaging, Boonsville (Bend Conglomerate) Gas Field, Fort Worth Basin, Texas: The Log Analyst, v. 38, p. 54–70.

Chambers, R. L., J. M. Yarus, and K. B. Hird, 2000, Petroleum geostatistics for nongeostatisticians Part 1 and 2, The Leading Edge, v. 19, p. 474-479 and p. 592-599

Chambers, R. L., and J. M. Yarus, 2002, Quantitative Use of Seismic Attributes for Reservoir Characterization, <http://www.geovariances.com/>, last visited on August 2009

Cooke, D., V. Ball, T. Muryanto, G. O'Donnell, and A. Sena, 1999, What is the best seismic attribute for quantitative seismic reservoir characterization?: Annual Meeting Abstracts, SEG, p. 1588-1591

Davis, J. C., 2002, Statistics and Data Analysis in Geology, 3rd Edition, John Wiley & Sons, Inc., 638 p.

Delfiner, P., and A. Haas, 2005, Over Thirty Years of Petroleum Geostatistics, in Space, Structure and Randomness, Springer New York, Lecture Notes in Statistics, v. 183, p. 89-104

Deutsch, C. V., and P. W. Cockerham, 1994, Practical considerations in the application of simulated annealing to stochastic simulation, Mathematical Geology, v. 26, p. 67–82

Dix, C. H., 1955, Seismic velocities from surface measurements, Geophysics, v. 20, n. 1, p. 68-86

Dubrulle, O., 1998, Geostatistics in Petroleum Geology, AAPG Continuing Education Course Note Series, n. 38

Doyen, P.M., D. E. Psaila, and S. Strandenes, 1994, Bayesian Sequential Indicator Simulation of Channel Sands From 3-D Seismic Data in The Oseberg Field, Norwegian North Sea, SPE 28382, 69th Annual Technical Conference, New Orleans, Louisiana, USA

Duboz, P., Y. Lafet, and D. Mougenot, 1998, Moving to a layered impedance cube: advantages of 3D stratigraphic inversion, *First Break*, v. 16. n. 9, p. 311-318

Faust, L.Y., 1953, A velocity function including lithologic variation, *Geophysics*, v. 18, n.2, p. 271-288

Gardner, R. A., 1960, The Boonsville (Bend Conglomerate Gas) Field Wise County, Texas' Abilene Geological Society, p. 7-18

Gardner, G. H. F., Gardner, L. W. and Gregory, A. R., 1974, Formation velocity and density, the diagnostic basics for stratigraphic traps, *Geophysics*, v. 39, p. 770-780

Geovariances, 2008, Petroleum Geostatistics course notes, Paris, France

Hamilton, D. S., B. A. Hardage, R. J. Finley, D. Carr, D. E. Lancaster, and R. Y. Elphick, 1997, Abstract: Application of Integrated Geological, Geophysical, and Engineering Analysis in Identifying Compartmented Reservoirs, Boonsville Field, Fort Worth Basin, Texas, AAPG, International Conference and Exhibition, Vienna, Austria

Hardage, B. A., D. L. Carr, D. E. Lancaster, J. L. Simmons, Jr., R. Y. Elphick, V. M. Pendleton, and R. A. Johns, 1996, 3-D seismic evidence of the effects of collapse on overlying clastic stratigraphy and reservoir compartmentalization *Geophysics*, v. 61, n. 5, p. 1336-1350

Hardage, B. A., J. L. Simmons, Jr., D. E. Lancaster, R. Y. Elphick, R. D. Edson, D. L. Carr, and V. Pendleton, 1996, Boonsville 3-D Seismic Data Set: The University of Texas at Austin Bureau of Economic Geology well log and petrophysical data and 3-D data in SEG-Y format on 1 CD-ROM, 1 text booklet (40 p., 9 figs., 5 tables, 1 appendix).

Hentz, T. F., J. A. Kane, W. A. Ambrose, and E. C. Potter, 2006, Depositional Facies, Reservoir Distribution, and Infield Potential of the Lower Atoka Group (Bend Conglomerate) in Boonsville Field, Fort Worth Basin, Texas: New Look at an Old Play, AAPG

Hill, R. J., D. M. Jarvie, J. Zumberge, M. Henry, and R. M. Pollastro, 2007, Geologic framework of the Mississippian Barnett Shale, Barnett-Paleozoic total petroleum system, Bend arch-Fort Worth Basin, Texas, *AAPG Bulletin*, v. 91, n. 4, p. 445-473

Hirsche, K., S. Boerner, C. Kalkomey, and C. Gastaldi, 1998, Avoiding pitfalls in geostatistical reservoir characterization: A survival guide, CSEG Recorder, issue June, p. 35-56

Hohn, M. E., 1998, Geostatistics and petroleum geology, 2nd Edition, Kluwer Academic Publishing, 260 p.

IHRDC, International Human Resources Development Corporation, Basic Geostatistics, <http://oilandgastraining.org>, last visited on October 2009

Intelligent Solutions Inc., 2008, Intelligent data evaluation and analysis (IDEA) software user manual

Isaaks, E. H. and R. M. Srivastava, 1988, Spatial Continuity Measures for Probabilistic and Deterministic Geostatistics, *Mathematical Geology*, v. 20, n. 4, p. 239-252.

Journel, A. G., 1994, Geostatistics and Reservoir Geology, in J. M. Yarus and R. L. Chambers, eds., *Stochastic Modeling and Geostatistics Principles, Methods, and Case Studies*, APPG Computer Applications in Geology n. 3, p. 19-20

Krose, B., and P. van der Smagt, 1996, *An Introduction to Neural Networks*, 8th Edition, The University of Amsterdam, 135 p.

Lancaster, D. E., B. A. Hardage, D. L. Carr, D. S. Hamilton, R. Y. Elphick, and T. H. Fate, 1996, Integrated Applications For Infield Reserve Growth In Midcontinent Gas Reservoirs, Boonsville Field, Fort Worth Basin, TX, SPE, 35629, Gas Technology Symposium, Calgary, Alberta, Canada

Lancaster, D. E., R. Y. Elphick, and C. R. A. Johns, 1996, A deterministic method for calculating facies from wireline logs, *The Log Analyst*, v. 37. n. 2,

Lindseth, R. O., 1979, Synthetic sonic logs - a process for stratigraphic interpretation, *Geophysics*, v. 44, n. 1, p. 3-26

Mavko, G., T. Mukerji, and J. Dvorkin, 1998, *The Rock Physics Handbook, Tools for seismic analysis in porous media*, 1st Edition, Cambridge University Press, 239 p.
McCormack, M. D., R. F. Stoitsits, D. J. Macallister, and K. D. Crawford, 1999, Application of generic algorithms in exploration and production, *The Leading Edge*, issue June, p. 716-718

McCulloch, W. S., and W. Pitts, 1943, A logical calculus of the ideas immanent in nervous activity, *Bulletin of Mathematical Biophysics*, v. 5, p. 115-133

McCormick, D. S., D. L. Carr, and I. D. Bryant, 1999, Integration of Analog Data for Building Testable, Deterministic Geological Models in a Common Interpretation Environment: An Example From the Atokan Boonsville Gas Field, Fort Worth Basin, Texas, SPE 57592, Annual Technical Conference and Exhibition, Houston, Texas

McDonnel, A., R. G. Loucks, and T. Dooley, 2007, Quantifying the origin and geometry of circular sag structures in northern Fort Worth Basin, Texas: Paleocave collapse, pull-apart fault systems, or hydrothermal alteration?, AAPG Bulletin, v. 91, n. 9, p. 1295-1318

Nikraves, M., and F. Aminzadeh, 2001, Past, present and future intelligent reservoir characterization trends, Journal of Petroleum Science and Engineering, v.31, issue 2, p. 67-69

Nikraves, M., and F. Aminzadeh, 2001, Mining and fusion of petroleum data with fuzzy logic and neural network agents, Journal of Petroleum Science and Engineering, v.29, p.221-238

Oldenburg, D. W., T. Scheuer, and S. Levy, 1983, Recovery of the acoustic impedance from reflection seismograms, Geophysics, v. 48, n. 10, p. 1318-1337

Ransom, R. C., 1995, Practical Formation Evaluation, John Wiley & Sons, Inc., 490 p.

Rider, M. H., 1986, The Geological Interpretation of Well Logs, 1st Edition, Blackie and Son Ltd., 175 p.

Russell, B. H., 1988, Introduction to seismic inversion methods, in S. N. Domenico, eds., Course Notes Series, v.2, SEG

Russell, B. H., and D. Hampson, 1991, Comparison of poststack inversion methods, SEG Extended Abstracts, n. 10, p. 876-878

Russell, B. H., 2006, The old and the new seismic inversion, CSEG Distinguished Lecture presentation

Schlumberger, 2009, Petrel software online manual

Schraudolph, N., and F. Cummins, Introduction to Neural Networks, Istituto Dalle Molle di Studi sull'Intelligenza Artificiale, <http://www.idsia.ch/NNcourse/>, last visited on August 2009

Sheriff, R. E., 1992, Basic petrophysics and geophysics, in Reservoir Geophysics, R. E. Sheriff, ed., SEG Investigations in Geophysics, n. 7, p. 37-49

Specht, D., 1991, A general regression neural network, IEEE Transactions on Neural Networks, v. 2, issue 6, p. 568-576

Srivastava, R. M., 1994, An Overview of Stochastic Methods for Reservoir Characterization, in J. M. Yarus and R. L. Chambers, eds., Stochastic Modeling and Geostatistics Principles, Methods, and Case Studies, APPG Computer Applications in Geology, n. 3, p. 3-16

Tanakov, M. Y., 1997, Integrated reservoir description for Boonsville (Texas) Field using 3-D seismic, well and production data, MSc Thesis, The University of Tulsa

Taner, M. T., 2000, Attributed Revisited, http://www.rocksolidimages.com/pdf/attrib_revisited.htm#_Toc494264878, last visited on August 2009

Wackernagel, H., 2003, Multivariate Geostatistics, An Introduction with Applications, 3rd Edition, Springer-Verlag, 387 p.

Xie, D., 2001, Thin-bed reservoir characterization using integrated 3-D seismic and well log data: A case study of the Central Boonsville Field, Fort Worth Basin, North-Central Texas, A PhD Dissertation, Michigan Technological University

Zahir, M., 1998, Application of Attribute Analysis to Three Dimensional Seismic Reflection Data for reservoir Delineation in the Boonsville Gas Field, North Central Texas, USA, BSc Thesis,

Zhao, H., N. B. Givens, and B. Curtis, 2007, Thermal maturity of the Barnett Shale determined from well-log analysis, AAPG Bulletin, v. 91, n. 4, p. 535-549

APPENDIX A

WELL LOG TYPES AND STRATIGRAPHIC NOMENCLATURE

Table A.1 Wells and well log data types available in this study.

WELL NAME	SP	GR	NPHI	RHOB	PEF	DELT	MICRO	CALI	MSFL
Ashe B2	X								
Ashe B3	X								
Ashe C1	X								
Ashe C2	X								
Ashe C3	X								
Ashe C4	X								
Ashe C5	X	X				X			
Ashe C6	X	X	X	X	X				X
B Yates 2	X								
B Yates 3	X								
B Yates 7	X								
B Yates 11	X	X		X	X	X		X	
B Yates 13	X	X	X	X				X	
B Yates 15	X	X	X	X	X			X	
B Yates 18D	X	X	X	X	X	X	X	X	X
Craft WB 12-1	X								
Craft WB 21-1	X								
Craft WB 21-2	X								
C Yates 9	X	X		X	X	X		X	
F Yates 7	X								
F Yates 10	X						X	X	
I.G. Yates 3	X								
I.G. Yates 4	X								
I.G. Yates 9	X	X	X	X				X	
I.G. Yates 13	X	X	X	X				X	
I.G. Yates 14	X	X	X	X				X	
I.G. Yates 18	X	X							
I.G. Yates 19	X	X	X	X				X	
I.G. Yates 21	X	X							
I.G. Yates 31	X	X	X	X	X			X	
I.G. Yates 32	X	X							
L.O. Fancher 1	X								
L.O. Fancher 2	X	X	X	X				X	
L.O. Fancher 3	X	X	X	X				X	
L.O. Fancher 4	X	X							
L.O. Fancher 5	X	X	X	X				X	
W Dewbre 1	X								
W Dewbre 2	X								

Table A.1 (continued)

WELL NAME	RILD	RILM	SFL	LL3	LL 8	S GRD	SN	LN	LAT
Ashe B2	X								
Ashe B3	X								
Ashe C1	X								
Ashe C2	X								
Ashe C3	X								
Ashe C4	X								
Ashe C5	X						X		
Ashe C6	X	X	X						
B Yates 2							X	X	X
B Yates 3							X	X	X
B Yates 7	X						X		
B Yates 11	X	X			X				
B Yates 13	X	X		X					
B Yates 15	X	X	X						
B Yates 18D	X	X	X						
Craft WB 12-1	X						X		
Craft WB 21-1	X						X		
Craft WB 21-2									X
C Yates 9	X	X			X				
F Yates 7	X						X		
F Yates 10	X						X		
I.G. Yates 3	X						X		
I.G. Yates 4	X						X		
I.G. Yates 9	X	X	X						
I.G. Yates 13	X	X	X						
I.G. Yates 14	X	X				X			
I.G. Yates 18	X	X		X					
I.G. Yates 19	X	X	X						
I.G. Yates 21	X	X		X					
I.G. Yates 31	X	X	X						
I.G. Yates 32	X	X	X						
L.O. Fancher 1	X						X		
L.O. Fancher 2	X	X		X					
L.O. Fancher 3	X	X		X					
L.O. Fancher 4	X	X		X					
L.O. Fancher 5	X	X				X			
W Dewbre 1	X						X		
W Dewbre 2							X	X	X

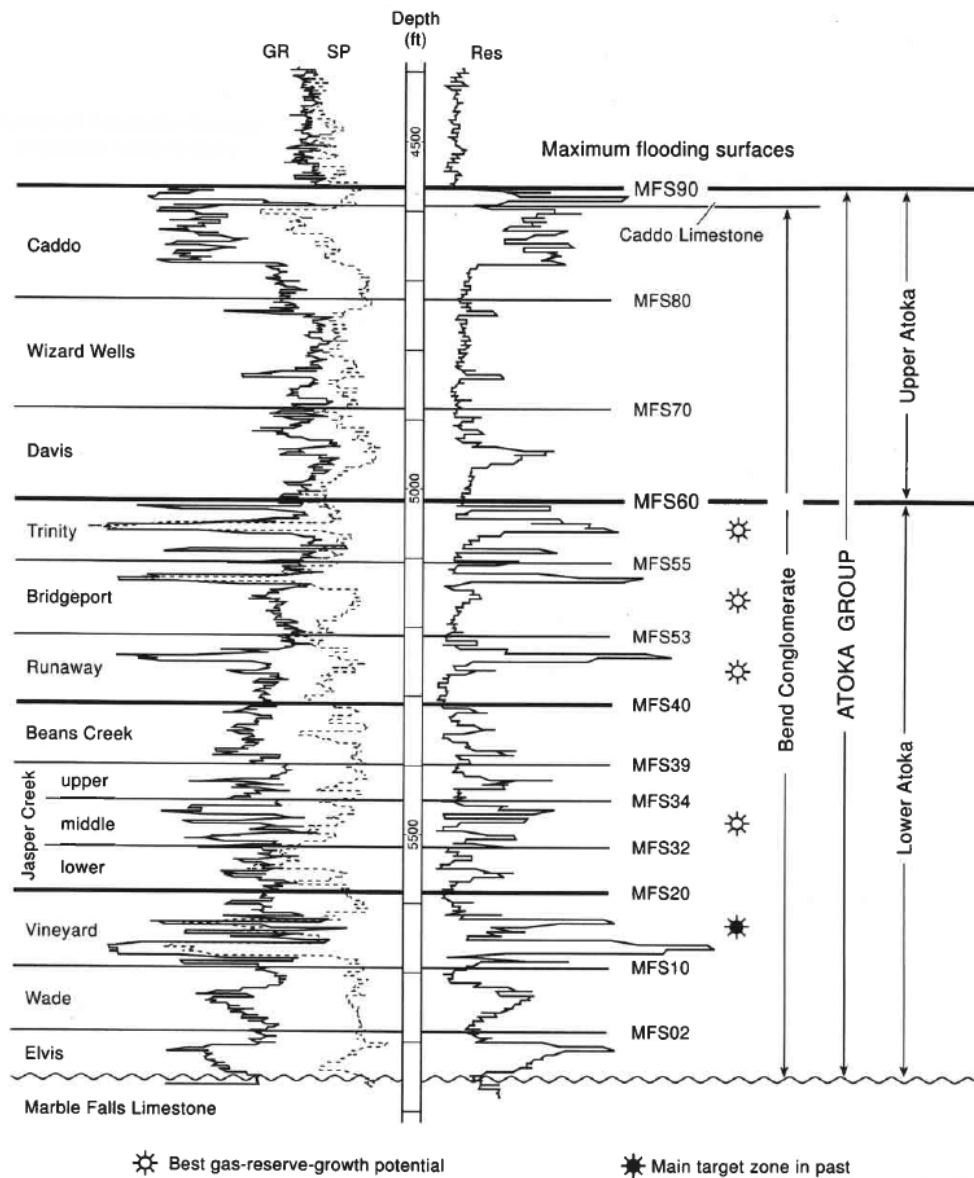


Figure A.1 Stratigraphic nomenclature used to define Bend Conglomerate genetic sequences by Bureau of Economic Geology for Boonsville field (Hardage et. al., 1996).

APPENDIX B

BASIC SEISMIC ATTRIBUTES

Theoretical basis of some of the basic attributes (Taner, 2000):

Envelope:

Analytic trace be given by: $F(t)=f(t)+g(t)$, where $f(t)$ is the real part corresponding to the recorded seismic data and $g(t)$, the imaginary part of the complex trace, is the Hilbert transform of $f(t)$. Then the envelope is the modulus of the complex function:

$$E(t) = \sqrt{|f^2(t) + g^2(t)|}$$

(B.1)

$E(t)$ represents the total instantaneous energy and its magnitude is of the same order as that of the input traces. It varies approximately between 0 and the maximum amplitude of the trace. The envelope is independent of the phase and it relates directly to the acoustic impedance contrasts. It may represent the individual interface contrast or, more likely, the combined response of several interfaces, depending on the seismic bandwidth. Trace envelope is a physical attribute and it can be used as an effective discriminator for the following characteristics:

- Represents mainly the acoustic impedance contrast, hence reflectivity,
- Bright spots,
- Possible gas accumulation,
- Sequence boundaries,
- Thin-bed tuning effects
- Unconformities,
- Major changes of lithology,
- Major changes in depositional environment,
- Lateral changes indicating faulting,
- Spatial correlation to porosity and other lithologic variations,
- Indicates the group, rather than phase component of the seismic wave propagation

Instantaneous Phase:

The argument of the complex function is the instantaneous phase:

$$\text{Ph}(x,t) = \arctan \left[\frac{g(x,t)}{f(x,t)} \right]$$

(B.2)

Instantaneous frequency is displayed in degrees. The phase information is independent of trace amplitudes and it relates to the propagation phase of the seismic wave front. Since, most of the time, wave fronts are defined as lines of constant phase, the phase attribute is also a physical attribute and can be effectively used as a discriminator for geometrical shape classifications:

- Best indicator of lateral continuity,
- Relates to the phase component of the wave-propagation.
- Can be used to compute the phase velocity,
- Has no amplitude information, hence all events are represented,
- Shows discontinuity, but may not be the best. It is better for showing continuity.
- Sequence boundaries,
- Detailed visualization of bedding configurations,
- Used in the computation of instantaneous frequency and acceleration

Instantaneous Frequency:

Time rate of change of phase is the instantaneous frequency:

$$\text{Freq}(x,t) = \frac{\partial[\text{Ph}(x,t)]}{\partial(t)}$$

(B.3)

The computed output is given in units of cycles per second. Instantaneous phase represents the phase of the resultant vector of individual simple harmonic motions. While individual vectors will rotate in clockwise motion, their resultant vector may, in some instances, form a cardioid pattern and appear to turn in the opposite direction. We interpret this as the effect of interference of two closely arriving wavelets. This can also be caused by the noise interference in the low amplitude zones. Instantaneous frequencies are mainly influenced by the bed thickness.

Instantaneous frequencies relate the wave propagation and depositional environment, hence they are physical attributes and they can be used as effective discriminators:

- Corresponds to the average frequency (centroid) of the power spectrum of the seismic wavelet.
- Seismic character correlator in lateral direction,
- Indicates the edges of low impedance thin beds,
- Hydrocarbon indicator by low frequency anomaly. This effect is some times accentuated by unconsolidated sands due to the oil content of the pores.
- Fracture zone indicator, they may appear as lower frequency zones.
- Chaotic reflection zone indicator, due to excessive scatter,
- Bed thickness indicator. Higher frequencies indicate sharp interfaces or thin shale bedding, lower frequencies indicate sand rich bedding.
- Sand/Shale ratio indicator in a clastic environment

Relative Acoustic Impedance:

Seismic trace represents the band limited reflectivity series, which can be expressed as:

$$f(t) = \frac{1}{2} \frac{\Delta\rho v}{\rho v} = \frac{1}{2} \Delta \ln(\rho v)$$

(B.4)

Therefore, by integrating the zero phase trace, the band-limited estimate of the natural log of the acoustic impedance is obtained. Since it is band limited, the impedance will not have absolute magnitudes and the stack section is usually the estimate of zero offset reflectivity; hence it is called relative acoustic impedance.

Relative acoustic impedance shows band limited apparent acoustic impedance contrast,

- It relates to porosity
- High contrast indicates possible sequence boundaries,
- Indicates unconformity surfaces,
- Indicates discontinuities

APPENDIX C

ACOUSTIC IMPEDANCE ESTIMATION RESULTS

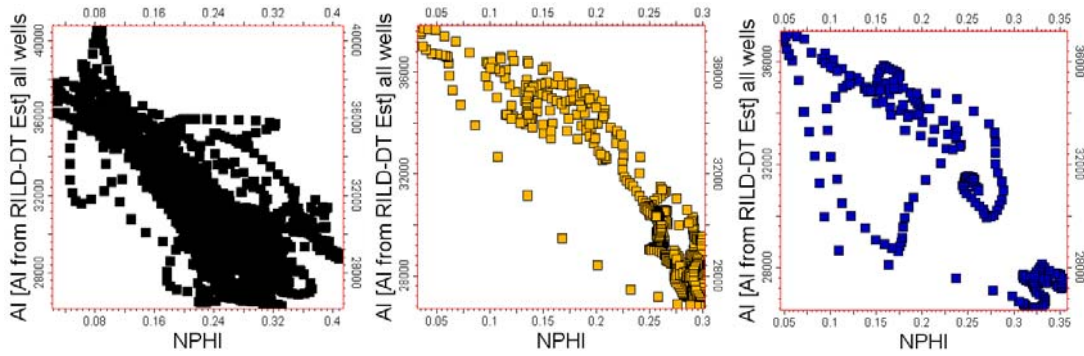


Figure C.1 NPHI versus estimated AI cross plots. Plots represent results for the wells B Yates 18D, IG Yates 19, and LO Fancher 5 with -0.79, -0.93, and -0.83 correlation coefficients respectively.

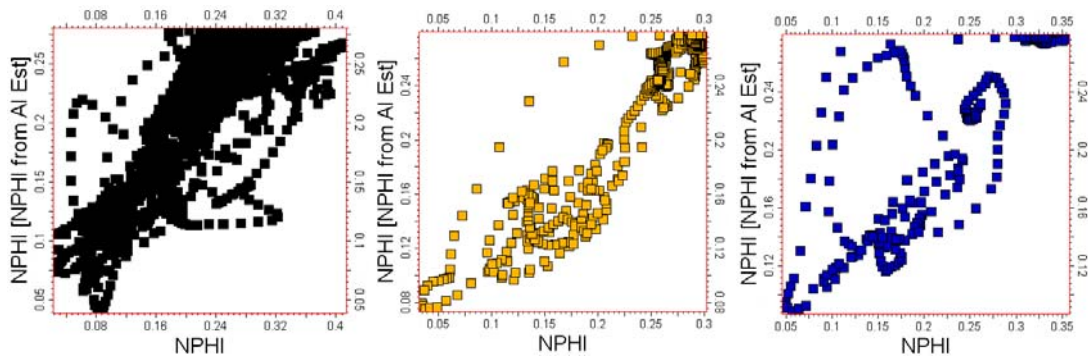


Figure C.2 NPHI versus NPHI estimated cross plots. Plots represent results for the same wells with 0.82, 0.95, and 0.81 correlation coefficients.

APPENDIX D

VARIOGRAM PRINCIPLES

A variogram is a plot of variability in terms of semi-variance against separation distance. It is generated by finding pairs of data with similar separation distances and then calculating the degree of dissimilarity between these pairs. Figure E.1 is a typical variogram.

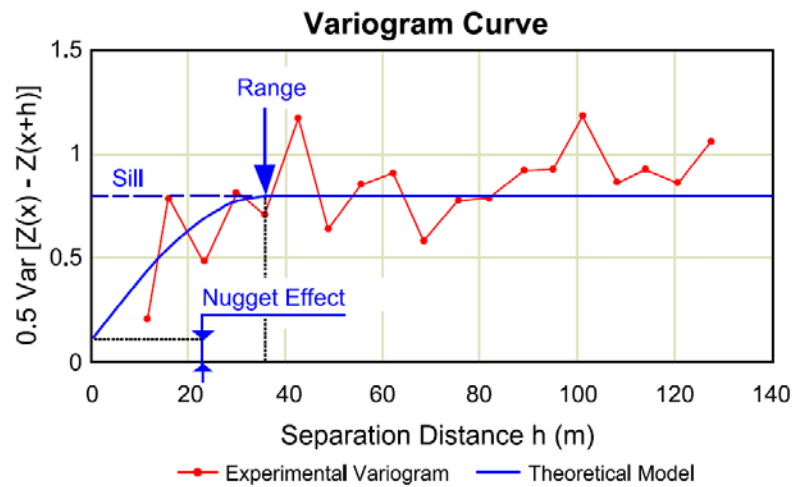


Figure D.1 Sample variogram and variogram model (Bongarcon, 2004).

Sample variogram: Variogram calculated for a sample data set using a direction and separation distance. Variogram model: A continuous mathematical expression used to describe the sample variogram. The variogram model in Petrel also contains information of anisotropy. Range: Describes where the variogram model reaches its plateau (i.e. the separation distance where there is no longer any change in the degree of correlation between pairs of data values). Sill: The semi-variance where the separation distance is greater than the range (on the plateau). It describes the variation between two unrelated samples. Transformed data should have a value of 1 and values much higher or lower than this (e.g. ± 0.3) may indicate a spatial trend. Nugget: The semi-variance where the separation distance is zero. It describes the short scale variation in the data. This is often most accurately identified from vertical data where the sampling interval is usually much lower. Plateau: The part of the variogram model where an increase in separation distance no longer increases the variogram value. Transition: Variogram models that reach a

plateau are referred to as transition models. Different types of variogram models are used to describe the transition.

Variograms should be calculated in several different directions because geological data is usually anisotropic (at least between the vertical and horizontal directions). These are commonly chosen as the Major and Minor directions in the XY plane and the Vertical direction. The Major direction may not necessarily follow the geological layers.

Major direction: The major direction defines the direction where the sample points have the strongest correlation. The angle of this major direction can be changed interactively by editing the direction in the search cone. The angle is specified as the clockwise angle from the north (in degrees) for the main search direction. **Minor direction:** This is the minor search direction and is perpendicular to the major direction.

Variogram dip: The dip is specified as the inclination (upward angle) in degrees between the major direction and the horizontal.

The procedure for data sampling in different directions is approximately the same; except that the vertical sample variograms always are calculated isotropically (i.e. orientation is not used). Nugget, sill and variogram type values will be the same in all three directions while the range will vary.

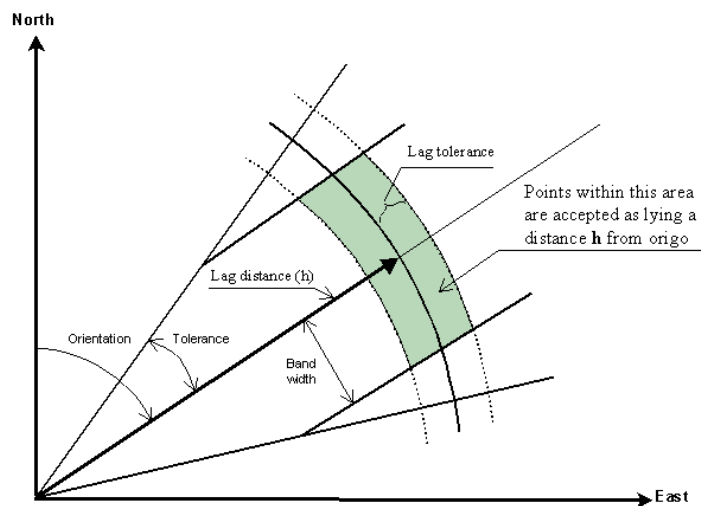


Figure D.2 Sample variogram calculation features (Schlumberger, 2009).

Orientation: The direction used in the search for sample pairs for construction of a directional sample variogram. The orientation is defined positively clockwise from the north direction. **Tolerance:** The tolerance in degrees from the orientation for the search of sample pairs. **Bandwidth:** Cut off to prevent the search area from

becoming too wide at large separation distances. Search distance: The maximum separation distance used in the search for sample pairs. Lag: Subdivisions of the range. Lag Tolerance: Distance from the lag at which data will be considered as belonging to that lag. This is quoted as a percentage of the lag distance. For example, 50% means that all points will belong to one lag, greater than 50% means that some same data may be considered in two lags, less than 50% means that some data may not be considered (Schlumberger, 2009).

VITA

PERSONAL INFORMATION

Surname, Name: Arzuman, Sadun

Nationality: Turkish

Phone: +90 507 3651989

Email: sadunarzuman@yahoo.com

EDUCATION

Degree	Institution	Year of Graduation
MS	Texas A&M University, Geology	2002
BS	İstanbul Technical Uni., Geophysical Eng.	1998

WORK EXPERIENCE

Year	Place	Enrollment
2007-present	Schlumberger	Support Engineer
2002-2007	TPAO	Geophysicist

FOREIGN LANGUAGES

Advanced English

PUBLICATIONS

Sadun Arzuman, Application of Petrel Neural Network Tools to Estimate Well Logs, Extended Abstract, IPETGAS, Ankara, Turkey, 2009

Sadun Arzuman, Seismic stratigraphic and structural interpretation of the Guassare-Misoa Interval, Lake Maracaibo, Abstract and Poster, AAPG Student Expo, 2002, Oklahoma, USA